UNIVERSIDAD DE BUENOS AIRES

Facultad de Ciencias Exactas y Naturales

Departamento de Física

Relajación de espín en semiconductores dopados y nanoestructuras semiconductoras

Trabajo de Tesis para optar por el título de Doctor de la Universidad de Buenos Aires en el área Ciencias Físicas

por **Guido A. Intronati**

Directores de Tesis: Prof. Dr. Pablo I. Tamborenea

Prof. Dr. Rodolfo A. Jalabert

Lugar de trabajo: Departamento de Física, FCEyN, UBA

IPCMS, Université de Strasbourg

Buenos Aires, abril de 2013

A mis hermanas

No hay nada más práctico que
una buena teoría.

(Kurt Lewin, 1952)

There is nothing more practical
than a good theory.

(Kurt Lewin, 1952)

Resumen

Actualmente, los dispositivos basados en materiales semiconductores están presentes en varias aplicaciones de comunicación y procesamiento de información. En estos dispositivos, las distintas operaciones involucradas implican el desplazamiento controlado de cargas. Para el almacenamiento de información, arreglos de múltiples capas formadas por metales magnéticos, así como materiales aislantes, son ampliamente utilizados. En este último caso, la información es registrada y recuperada al reorientar dominios magnéticos.

La posibilidad de construir dispositivos que uliticen otra propiedad de las partículas, el llamado espín, da lugar al campo de la Espintrónica, a diferencia de la electrónica tradicional basada en la carga eléctrica de las partículas. Más aún, la Espintrónica con materiales semiconductores busca el desarrollo de dispositivos híbridos en los cuales las tres operaciones básicas (lógica, comunicación y almacenamiento) puedan estar integradas en un mismo material. A pesar de los grandes progresos y avances en esta dirección, son varias las preguntas y dificultades técnicas que quedan por resolver. El desafío, entre otros, es entonces entender cómo el espín se comporta e interacciona en un material sólido. El espín, al ser una propiedad cuántica de cualquier partícula elemental, está representada por un estado, susceptible de ser afectado por alguna dada interacción. El espín de un electrón, por ejemplo, puede no sólo interaccionar con un campo magnético externo, sino también acoplarse a otro grado de libertad del electrón. La interacción de espín-órbita, precisamente, se refiere al acoplamiento entre el espín y el estado orbital del mismo electrón.

En la primera parte de esta tesis consideramos este último efecto, y en particular, nos ocupamos de un semiconductor *bulk* de GaAs dopado, y estudiamos la relajación

Resumen

de espín debido a la interacción de espín-órbita. Las densidades de dopantes de nuestro interés están en un rango cercano a la densidad crítica correspondiente a la transición metal-aislante. Por debajo de esta densidad, la propiedades electrónicas del sistema son las de un material aislante, mientras que para densidades mayores, aparece un comportamiento de tipo metálico y en consecuencia, la conductividad a temperatura nula adquiere un valor finito. En esta tesis estudiamos la relajación de espín del lado metálico de la transición debido a dos clases diferentes de interacción espín-órbita. La primera de ellas está asociada a la presencia de impurezas, mientras que la otra aparece como consecuencia de la asimetría de inversión causada por la presencia de dos tipos diferentes de átomos en una celda unidad. Es decir, esta última es una propiedad inherente de la estructura cristalina del material y es también conocida como la interacción de *Dresselhaus* o BIA, por sus siglas en inglés (*bulk inversion asymmetry*). Para atacar el problema de la dinámica de espín, desarrollamos una formulación analítica basada en la difusión de espín de un electrón en el régimen metálico de conducción en la banda de impurezas. A través de esta derivación logramos una expresión para el tiempo de relajación de espín, dependiente de la densidad de dopantes y de la intensidad de la interacción de espín-órbita. Notablemente, dicha expresión está exenta de parámetros ajustables. Complementamos este esquema y respaldamos los resultados obtenidos analíticamente con el cálculo numérico del tiempo de vida del espín. Para ello, llevamos a cabo la evolución temporal de un estado inicial con un espín definido. De esta manera, el valor medio del operador de espín evoluciona bajo la influencia del Hamiltoniano completo, que comprende la interacción de espín-órbita y el Hamiltoniano del modelo de Matsubara-Toyozawa. Este último describe la banda de impurezas pero no toma en cuenta el espín. El estado inicialmente polarizado, al no ser un autoestado del operador Hamiltoniano completo, experimenta un decaimiento temporal siguiendo un dado comportamiento, del cual extraemos el tiempo de relajación de espín.

En la segunda parte de esta tesis consideramos un sistema cuántico de dimensión cero (punto cuántico o *quantum dot*) y estudiamos el efecto de la interacción de espín-órbita sobre los autoestados. El *quantum dot* está alojado entre dos heteroestructuras

implantadas en un nanohilo de material InAs. Este material presenta la particularidad que, al ser crecido de manera unidimensional, adquiere una estructura de tipo wurtzita, a diferencia de la estructura zinc blenda que tiene en su fase *bulk*. Aquí desarrollamos una solución analítica para el *quantum dot*, considerando la interacción de espín-órbita propia de este tipo de estructuras. Más precisamente, tomamos la interacción de Dresselhaus de la banda de conducción de un material wurtzita que, además de un término cúbico en k -aunque de diferente forma que el de zinc blenda- presenta uno lineal, propio de la wurtzita. El efecto de un campo magnético débil es introducido a través del acoplamiento de tipo Zeeman. Entre los resultados se incluyen además la estructura de espín en el *quantum-dot* y el cálculo del factor g efectivo en función de las dimensiones del *dot*. Por último, estudiamos y calculamos la relajación de espín debido a fonones acústicos, teniendo en cuenta para ello los potenciales de fonón correspondientes a la estructura wurtzita.

Palabras claves: interacción espín-órbita, relajación de espín, semiconductores dopados, nanoestructuras, puntos cuánticos, fonones

Summary

Spin relaxation in doped semiconductors and semiconductor nanostructures

At present, information-processing and communications are mainly based on semiconductor devices, within which all the operations imply the controlled motion of small pools of charge. For information-storage, multilayers of magnetic metals and insulators are predominantly used. In this last case, the information is stored and retrieved by reorienting magnetic domains. The possibility of building devices that use another property of particles, the spin, gives rise the so-called Spintronics, in contrast to the current charge-based technology. Moreover, semiconductor spintronics pursues the development of hybrid devices where the three basic operations -logic, communications and storage- within the same materials technology would be possible. In spite of the strong progress and numerous advances in the field, many fundamental questions and technical hurdles remain unsolved. A lot of effort is therefore devoted to understand how the spin behaves and interacts with its solid-state environment.

The spin, being a quantum property of any elementary particle, is represented by a state that may change due to some given interaction. The spin of an electron, for example, can not only interact with an external magnetic field, but also with another degree of freedom of the electron. In this sense, the so-called spin-orbit interaction precisely refers to the coupling between the spin and the orbital state of the same electron.

In the first part of this thesis we regard this latter effect, and in particular, we adress

Summary

the problem of the spin-relaxation in a bulk doped GaAs semiconductor resulting from the spin-orbit interaction. Our interest is focused on donor density values close to a critical value, where a metal-insulator transition occurs. Below this density, the electronic properties of the system correspond to that of the insulating regime, while for larger densities, a metallic behaviour appears and accordingly, a non-zero conductivity is measured at $T = 0$. It is on this metallic side of the transition where we study the spin relaxation due to two different types of spin-orbit coupling. The first of them is associated to the presence of extrinsic impurities, while the other one appears as a consequence of the bulk inversion asymmetry (BIA) brought about by the the presence of two different atoms (Ga and As) in a unit cell. This latter SOC is also known as the Dresselhaus coupling. To tackle the spin dynamics problem, we develop an analytical formulation based on the spin diffusion of an electron in the metallic regime of conduction of the impurity band. The full derivation provides us with an expression for the spin-relaxation time, which depends on the doping density and the spin-orbit coupling strength, and remarkably, is free of adjustable parameters. We complement this approach and back our analytical results with the numerical calculation of the spin lifetime. For this, we perform and track the exact time evolution of an initial state with a defined spin state. We look at the spin operator evolving under the influence of the full Hamiltonian, containing both the spin-orbit interactions and the spin-free Hamiltonian (based on the Matsuba-Toyozawa model) describing the impurity band. The initial polarized state, being no longer an eigenstate, decays following a certain damped time evolution, from which we extract the spin-relaxation time.

In the second part of the thesis we consider a zero-dimensional system and study the effect of spin-orbit coupling on the eigenstates. The quantum dot is hosted between two heterojunctions placed in an InAs nanowire. This semiconductor, when grown unidimensionally, presents a wurtzite-type crystal structure, unlike its zincblende phase in bulk. We develop here an exact analytical solution for the quantum dot, taking into account the proper effective spin-orbit coupling for this type of material. We focus on the BIA coupling, which presents a cubic-in-k SOC, yet with a different expression from

that of zincblende, and add also the linear-in-k SOC, characteristic of WZ materials. A Zeeman interaction from an external magnetic field is included as well. We calculate the energy spectra for different values of the spin-orbit coupling strength. We also display the spin texture across the dot, compute the effective g-factor as a function of the dot size, and calculate the spin-relaxation due to acoustic phonons, taking into account the phonon potentials corresponding to the wurtzite structure.

Contents

Chapter 1

Introduction

1.1 General Presentation

The spin is an inherent property of electrons, photons, quarks and in general, any elementary particle. Its nature lies in quantum mechanics. Its existence was proposed nearly 90 years ago by Pauli, while trying to solve some inconsistencies observed in molecular spectra. He then called this new degree of freedom spin and claimed that in the case of electrons, it could only take two possible values, which was later on verified for electrons, as well as for protons and neutrons.

The spin is ubiquitous in many phenomena in condensed matter physics. For example, in magnetic resonance imaging (MRI) the spin of the proton is used to visualize internal structures of the human body. Another celebrated example is that of itinerant ferromagnetism, where the electron spin appears as a crucial ingredient. An understanding of the interactions that affect the spin dynamics is therefore necessary, both to describe observed phenomena in physical systems and to exploit the possibilities it offers for technological applications.

Conventionally, the spin is associated to an intrinsic angular moment, and due to the way it couples to a magnetic field, it is also viewed as an intrinsic magnetic moment of the particle. Its dipole-like magnetic moment interacts with a magnetic field, such that it experiences a torque $\mathbf{S} \times \mathbf{B}$ that tends to align the spin orientation with this field.

Another interaction that is central in this work is the coupling between the motion of an electron -its orbital degree of freedom- to the spin. To illustrate this, it suffices to consider an electron moving in an electric field. In the electrons' frame of reference, this electric field is transformed into a magnetic field, which according to what we have just mentioned, interacts with the electronic spin. This gives rise to the so-called spin-orbit interaction (SOC).

In solid state physics, the electronic spin is necessary to explain many phenomena, like the ferromagnetism as we have just cited. Ferromagnetic metals are constituted of atoms with a partially filled electronic shell. This means that for each spin in the shell with a given state there is not another spin with the opposite state. The spontaneous alignment (being an additional and distinct effect) of these unpaired spins along the same direction creates a net magnetization by effect of the exchange interaction, even though no external magnetic field is necessarily present.

Spin-orbit interactions are not only a key ingredient in the phenomenology of many experimental observations, but can also be used to control the state of a spin. For example, the fact that the spin of an electron may only take on two values, and the possibility to switch between these two states by means of any of the interactions with the environment, makes the spin an ideal candidate for computation. In this context, each of the two possible values is equivalent to a *bit* of information. The spin is bound to the charge, that may displace across the device, transporting this information. It is then important that the spin state remains unperturbed so that the information encoded in its state is not lost. This promising feature fostered a great deal of research in this direction in view of its technological potential. In recent years, new experimental setups have been proposed and designed in the search of physical systems where the spin can be efficiently manipulated. More precisely, its properties have been intensely studied both in bulk and low-dimensional systems, the latter meaning that the motion of the electron is spatially confined. An archetype of these systems is a quantum well made on a heterostructure, where the composition of a semiconductor material is changed on the nanoscale [1]. For example, a $GaAs$ layer between two $Al_xGa_{1-x}As$ layers makes up a

quantum well, where the motion of the electrons parallel to the layers remains free, but is confined in the transverse direction.

Low-dimensional systems have also been widely used to test fundamental physical concepts, such as the quantum-mechanical version of the Hall effect: in a two-dimensional sample, and at low temperatures, the quantization of the conductivity as a function of the applied magnetic field was first observed in 1980 by Klaus von Klitzing, later on awarded with the Nobel Prize.

The purpose of this thesis, expressed in a broad sense, is to study the interaction of the electron spin with its solid-state environment in semiconducting systems. This may be reckoned as the central question of the so-called spintronics discipline, which in contrast to conventional electronics involving the *charge*, makes use of the *spin* instead.

1.2 Spintronics

Even though the success of any spintronic device hinges on the controlled manipulation of the spin degree of freedom, finding an effective way to polarize a spin system, having a long lifetime of the spin orientation, and being able to detect it are the three major challenges.

Many techniques are utilized nowadays for the generation of spin polarization. The optical orientation and the electrical spin injection are among the better developed. While the former is based on the transfer of angular momenta from circularly polarized photons to electrons, the second one uses a magnetic electrode connected to a sample. The injected spin-polarized electrons flow from the electrode to the sample, and a non-equilibrium spin accumulation may so be achieved. The spin population, no matter how it is generated, will eventually evolve towards equilibrium by means of spin relaxation mechanisms, many of which involve the aforementioned spin-orbit interaction.

Before describing some spintronic devices, it is worth pointing out that in what follows we also refer to the term spin as meaning an *ensemble* of individual spins. Historically, spintronic devices used these ensembles to store information, but nowadays, experimen-

talists have been able to address and control one single spin. In addition to this distinction, we mention that spintronic devices are normally made either of semiconductor or metallic (normal or ferromagnetic) materials, or of a combination of both.

In the case of metals, the discovery of Giant Magneto Resistance represented a big boost for spintronics. It generated a great deal of interest in the academic field, but also in industry because of the technological applications it enabled. It was observed in 1988 by Fert [2] and afterwards by Grünberg *et al.* [3]. Soon after, it was successfully applied in data storage technologies [4]. IBM bolstered the role of spintronics in 1997 when it introduced the first hard-disk drive based on the GMR technology. The implementation of such structures by IBM for new read heads into their magnetoresistance hard-disk drives was just the first step of a race towards smaller and smaller hard-disks, found currently in any mobile device. In a typical GMR device, a non-magnetic metallic spacer is placed between two ferromagnetic layers. The relative orientation of the magnetization polarization of these layers determines the overall resistance. The physical principle behind the GMR is the fact that the scattering of electrons travelling through a ferromagnetic conductor depend on the relative orientation of their spin with respect to the magnetization direction of the conductor. This means that electrons bearing a spin aligned with the magnetization axis scatter differently from those having an opposite spin. Actually, those oriented parallel scatter less often than those oriented antiparallel. In the GMR setup we have just described, this effect can be exploited in the following way: the electrons injected from one of the magnetic conductors into the non-magnetic conductor will be preferentially oriented in one direction. If these electrons then arrive to the second ferromagnetic layer, they will pass into it freely from the non-magnetic metal, without undergoing strong scattering, only under the condition that their preferred orientation is parallel to the magnetization of the second layer. Hence, the resistance of the trilayer arrangement depends strongly on the relative magnetization direction of the two ferromagnetic layers. Although the whole process is about the flow (or not) of electrons, the fact that the spin is used to control this flow is the reason to reckon it as a great inspiration for the spintronic field [5].

Another closely related phenomenon is observed if the spacer is replaced with a non-magnetic insulating layer, giving rise to a magnetic tunnel junction, or tunneling magnetoresistance (TMR) device. In this configuration, the electrons tunnel through the layer without flipping its spin. Although being proposed in 1975 by F. Jullière, the observation of magnetoresistance in such junctions was possible only in 1995, when certain experimental difficulties were overcome. After this achievement, the challenge to develop new magnetic random access memory (MRAM) using this technology attracted a lot of attention from the community, and finally the first MRAM product was presented in 2006. Fast read/write times, as of the order of 5 ns, are now pursued [6].

There is still another experimental setup based on the so-called Tunneling Anisotropic Magnetoresistance, where only a single magnetic layer is needed. In this case, the resistance depends on the angle of the magnetization vector of this layer with respect to some crystallographic axis of an adjacent semiconductor layer. The TAMR necessitates a semiconductor material with a strong spin-orbit coupling and some magnetic anisotropy to be efficient. In Ref. [7], this type of magnetoresistance is explained in more detail.

The use of semiconductors in a spintronic device was firstly proposed in 1990, when the Datta-Das transistor, known also as the Spin-Field effective transistor (SFET) [8], was presented. It illustrates the fundamental ideas of a spin-based logic device. In it, a drain and a source made of ferromagnetic materials (with parallel magnetic moments; see Fig 1.1) provide the necessary pieces to inject and detect the spin, respectively. Between them, a non-magnetic semiconductor sample makes up a narrow channel for the electrons to flow ballistically from the source to the drain. The electrons injected by the source are spin-polarized. If the electron polarization arriving at the drain is parallel to the drain magnetic moment, the electron goes through. Otherwise, it is scattered off and a large resistance is measured. The degree of spin rotation so determines whether there is a current or not. In order to control this amount of rotation, a voltage gate is applied on top of the semiconductor channel. This electrostatic potential, in combination with the confinement geometry of the channel and the spin-orbit coupling in the substrate constitute an effective magnetic field that makes the spin precess across the sample. The
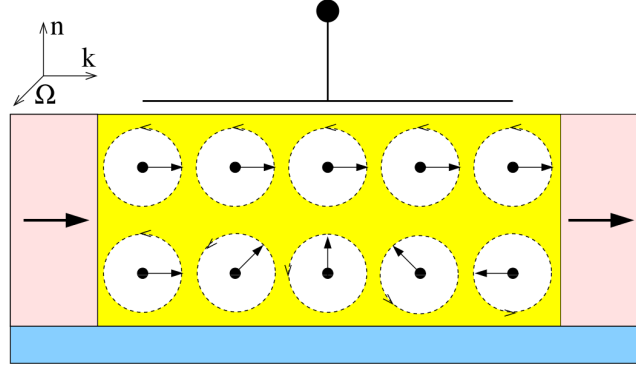
Figure 1.1: In the scheme of the Datta-Das spin field-effect transistor (SFET), a ferromagnetic emitter (spin injector) and a ferromagnetic collector (spin detector) are placed with parallel magnetic moments. In between, an InGaAs/InAlAs heterojunction in a plane normal to n generates a channel for two-dimensional electron transport between the two ferromagnetic electrodes. The spin-polarized electrons injected by the source with wave vector k move ballistically across the channel. Due to the spin-orbit interaction, the spins precess about the precession vector Ω, defined also by the structure and material properties of the channel. The strength of Ω can be tuned by the gate voltage applied on the top of the channel, which indirectly controls the degree of rotation of the spin. In the end, the current is large if the electron spin at the drain points in the initial direction (top row), and small if the direction is reversed (bottom) The current is so modulated by the gate electrode. Taken from Ref. [9]

final effective result is the ability to control the spin rotation, and thereby the current, by means of the gate voltage. Other proposals akin to the Datta-Das transistor have been put forward, for example, by Schliemann *et al.* [10], where the condition of ballistic transport is relaxed by tuning the Rashba and the Dresselhaus (to be explained below) spin-orbit couplings so that the eigenspinors become momentum-independent. Hence, elastic or inelastic scattering processes changing the wave vector do not randomize the

spin state of transmitted electrons.

An important remark here is that the spin-flip process involved in any of the spin transistors described above requires less energy than the energy needed for charge transport, which inevitably entails energy dissipation, as in the conventional field-effect transistor. From this point of view, spintronics is also a key player in power consumption optimization.

All these devices, as we said, require in general long spin lifetimes. And that is why semiconductors are so relevant in spintronics. Their great advantage is that besides the long lifetimes, the spin can be manipulated via the characteristic strong spin-orbit coupling of these materials. An example of this rather long spin relaxation times is encountered in bulk doped GaAs semiconductors. In this case, it was observed that spin relaxation times of the order of 100 ns can be obtained at certain doping densities, the spin relaxation times being strongly affected by the impurity density, as we will see in the next section. We concentrate on this problem in the first part of the thesis.

When a semiconductor is doped, the impurities are not arranged in a regular way as the crystal structure hosting them does. They form a random distribution inside the perfectly ordered crystal structure. This feature leads then naturally to the theory of transport in disordered systems. The first research works on such systems go back to the late fifties when P. W. Anderson published his pioneering paper *Absence of Diffusion in Certain Random Lattices*. Although many works that followed dealt with the electrical conduction (or equivalently electronic eigenstates) in disordered systems, Anderson's paper context was the diffusion of an initial spin excitation which, according to the experimental observation [11], seemed to remain localized for low-concentration of spins. Interestingly, the opening sentence in Anderson's abstract [12] was

> ***This paper presents a simple model for such processes as spin diffusion or conduction in the impurity band.***

In the first part of this thesis we also consider the impurity band of a GaAs semiconductor, where spin related processes are examined and the spin relaxation time is calculated. Many aspects of the physics in the impurity band will be carefully unfolded

in the following sections.

Anderson's cutting-edge ideas about localization could have been regarded, as he points out in Ref. [13], as the germ of modern quantum computation: localization would provide the necessary isolation to have independent sites with a quantum entity (spin) inside, thereby forming a two-level system, and sufficiently protected from loss of coherence. Needless to say that the very word "qubit" did not exist at the time. In spintronics, a qubit means a bit of quantum information, or equivalently, a controllable quantum two-level system. A superposition of these states represents a possible configuration that can be changed via a unitary evolution, performing many classical computations in parallel. The common condition of the various spin-based quantum computers that have been proposed is the manipulation of the dynamics of the spin. Many of them employ GaAs quantum dots [14] or Si systems [15], to be introduced later. As a zero-dimensional example, a quantum dot is built upon spatially confining one or many conduction band electrons in its three directions. Nowadays, the so-called qubits are commonly realized in quantum dot nanostructures, as originally proposed in 1998 [14], but they can also be found in trapped atoms or ions, in quantum states of Josephson junctions, and other examples.

One of the challenges in these confined systems is to manipulate the electron spin in a short time, shorter than the time for it to lose the coherence of information. It is precisely the long coherence times (of the order of hundred of nanoseconds) of spin that make them suitable for quantum computation. However, the electrical read-out of the state of an individual electron spin (the spin orientation) was possible only in 2004 [16], reported by the group of Kouwenhoven. In their experiment, an electron is trapped in a quantum dot, in the presence of a magnetic field that separates the energy of the two possible spin states (Zeeman splitting). An electrostatic potential is tuned such that if the spin is down (antiparallel to the magnetic field), the electron leaves the dot; otherwise it stays. In this way, the charge of the state in the dot is correlated to the spin state of the electron. Using a nearby quantum point contact, they were able to detect whether the dot was occupied or not. In 2010, the same group described in Ref. [17] an ingenious

experiment, where they claimed to be able to control the individual spin in a quantum dot via the spin-orbit interaction. The more sophisticated arrangement consisted of two quantum dots hosted in a InAs nanowire, a quasi-one-dimensional structure where the electrons can flow in one direction. The quantum dots are defined within the nanowire by making use of gate voltages applied over it. In the experimental setup, the electrons in both dots are individually addressable. In this scheme, fast qubit rotations and universal single-qubit control were accomplished using only electric fields, coupled to the spin via the SOC.

In the second part of the thesis we focus on InAs nanowires. This specific choice is related to the fact that, when grown unidimensionally, this semiconductor material acquires a wurtzite-type (WZ) crystal structure, unlike the zincblende case that we considered for the spin relaxation in a bulk GaAs sample. We specifically study a quantum dot in such a wire, with cylindrical shape and in particular, we consider the case where the radius is larger than the length ("pillbox"-like). Taking this into account, we analyse different electronic properties by including the appropriate effective spin-orbit coupling terms derived for a WZ structure.

As a general remark, it is worth emphasizing that spintronics, far from being only a topic in the realm of fundamental science, promises new technological applications to keep up with the demand on the increasing number of transistors in computer processors, and the continuing miniaturization of electronic devices. This is largely a motivation to foster the scientific research in this field.

In the following, we go through the two main subjects already mentioned, starting with the spin relaxation in a doped semiconductor as well as the physics related with the metal-insulator transition, and secondly, we describe quantum nanostructures in more detail.

1.3 Spin relaxation in n-GaAs

As it was already indicated, the first part of this thesis deals with the spin relaxation in a doped bulk GaAs semiconductor. The role of impurities is of paramount importance, and in particular, the spin relaxation depends strongly on the doping density. We start by recalling the different density ranges of interest, in which distinct electronic transport properties are observed. Afterwards, we resume the study of the spin-orbit coupling and spin relaxation.

1.3.1 Different doping density regimes in a bulk semiconductor

Let us first consider the extreme situation of a single impurity placed in the semiconductor host lattice. If the impurity is a donor, as it is in our case, a new electronic state is created close to the conduction band, within the energy gap of the semiconductor. As other impurities are added, so that the electron may *jump* from one to the other, an impurity band will arise out of the donor states of different impurities. If we further increase the donor density, this band gets broader and the electronic states span over a larger energy interval. Beyond a certain density -**the hybridization density**- the impurity and conduction bands merge. Below this value, the system is in the impurity band regime, where two different phases can still be distinguished. It is important to remark that due to the fact that the impurities are randomly distributed, the wave number k associated to the *crystal momentum* of the electron is not a good quantum number anymore since the translational invariance is broken.

One common property of three dimensional disordered systems is the coexistence of localized and extended states, as it is illustrated in Fig. 1.2. In a density of states picture, the localized states appear towards the band edges, while the extended states are located in between. The separating limit is called the **mobility edge** (E_c). Here the Fermi Level comes into play. If it is situated in the localized region $(|E_F| > E_C)$, the system does not conduct at $T = 0$ and it behaves as an insulator. For $T > 0$, the electrons can be thermally excited, either to an extended state or to another localized
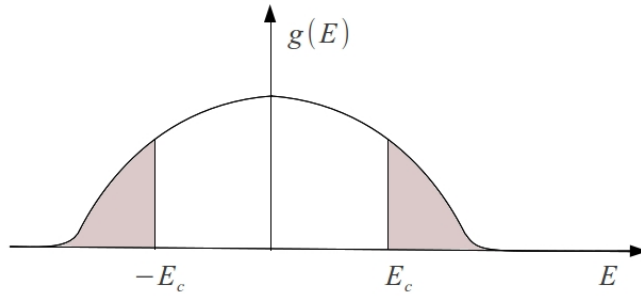
Figure 1.2: Schematic representation of the density of states of a disordered system as a function of energy within the Anderson model. The coloured zone represents localized states, while the extended states are in between. The energy separating them is called the *mobility edge.*

state, thereby giving rise to conduction. Conversely, once the Fermi Level enters the extended region, the metallic regime is reached.

In the Anderson model, the **metal-insulator transition** takes place when the two mobility edges come together, and the energy spectrum contains only localized states [18]. At the precise density of n_c, disorder systems show interesting properties like fractality [19].

In conclusion, for three dimensions, depending on the doping density, there may be a coexistence of both localized and extended eigenstates in the energy spectrum, separated by the mobility edge cited before. For one dimensional systems, instead, the Anderson model predicts that all the eigenstates are localized no matter how weak the disorder is [12]. For two dimensions the scaling theory of localization yields an insulating phase for any degree of randomness, but the localization length may be extremely large. Experiments exhibiting the signature of metallic behaviour, have often been interpreted by going beyond single-particle modes and invoking the interaction between electrons [20]. It has also been found in two dimensions that spin-orbit coupling favors the delocalization of the electrons.
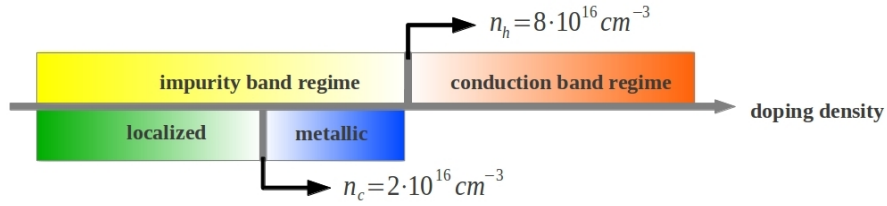
Figure 1.3: Different conducting regimes according to the dopant density are shown. At the hybridization critical density n_h separates, the impurity band merges the conduction band. Below n_h, two situations may arise: between n_h and the MIT density n_c, we observe the metallic regime with delocalized states, while for densities smaller than n_c, the insulating regime is reached, and the conductivity at zero temperature vanishes.

Our study deals with three dimensional systems, and focuses on the spatial extension of one-particle electronic states in the impurity band, of which we present a detailed study in Chap. 3. We start there with a preliminary analysis that does not contain the spin, and then we look at the spin-orbit coupling effects on the density of states, as well as the distribution of the so-called Inverse participation ratio, that measures the degree of extension of a wave function. The original results presented in this Chapter have been published in Ref. [21].

1.3.2 Spin dephasing and spin relaxation

We now come back to the description of the spin and discuss the key concepts concerning the spin decay time. The first step is to address the precise meaning of the word spin relaxation, in contrast to the spin dephasing concept. Microscopically, relaxation and dephasing are driven by different spin processes, although both lead to spin-lifetime decays [22]. In general, the relaxation time T_1 (also called longitudinal time) and the dephasing time T_2 (transverse) are two characteristic times that appear in the context of the magnetization produced by a spin ensemble. The Bloch-Torrey equation describes the precession, decay and diffusion of the magnetization $\mathbf{M}$ (associated to the spin) in

the case of mobile electrons. These equations include the two times in question [9],

$$
\begin{aligned}
\frac{\partial M_x}{\partial t} &= \gamma(\mathbf{M} \times \mathbf{B})_x - \frac{M_x}{T_2} + D\nabla^2 M_x \\
\frac{\partial M_y}{\partial t} &= \gamma(\mathbf{M} \times \mathbf{B})_y - \frac{M_y}{T_2} + D\nabla^2 M_y \\
\frac{\partial M_z}{\partial t} &= \gamma(\mathbf{M} \times \mathbf{B})_z - \frac{M_z - M_z^0}{T_1} + D\nabla^2 M_z
\end{aligned}
$$

where a magnetic field $\mathbf{B}(t) = B_0\hat{z} + \mathbf{B}_1(t)$ with a static part B_0 and a transverse oscillating $\mathbf{B}_1$ are assumed to be applied. D is the diffusion coefficient, $\gamma = \mu_B g/\hbar$ is the electron gyromagnetic ratio including the Bohr magneton μ_B and the electron g-factor; $M_z^0 = \chi B_0$ is the thermal equilibrium magnetization with χ being the static susceptibility. These phenomenological equations show that T_1 is related to the time it takes for the longitudinal magnetization to reach equilibrium. Equivalently, it accounts for the non-equilibrium population decay, in which a certain amount of energy has to be transferred from the spin system to the lattice, for example, via phonons. The time T_2, on the other hand, measures how long the transverse component of the spin ensemble is well-defined and can precess around the longitudinal direction.

Regarding this spin dephasing time, there are two processes that contribute. The first contribution to T_2 comes from the so-called inhomogeneous broadening, that appears for example as a consequence of the inhomogeneities in the g-factor [22], that leads ultimately to different precession frequencies of the individual spins. This broadening might also be brought about by a momentum-dependent spin-orbit coupling or an energy-(or momentum-) dependent g-factor. Conventionally, when the spin dephasing time includes this type of broadening related to reversible processes, it is refered as T_2^*. By contrast, if the phase is lost due to spatial or temporal fluctuations of the precessing frequencies (or magnetic fields equivalently) leading to *irreversible* dephasing, the term *homogeneous* broadening is used, and the time T_2 does not bear a star symbol. In the case of mobile electrons, the different momentum states have slightly different g-factor and thus different precession frequencies. This inhomogeneous broadening is however surpassed by the so-called motional narrowing, that we next explain.

For mobile electrons, the times T_1 and T_2 are calculated by averaging the spin over the thermal distribution of the electron momenta. The different momentum states have different spin flip characteristics, and therefore momentum scattering entails spin-flip scattering. This means that when an electron undergoes a momentum scattering, its spin orientation might change, which is equivalent to having a fluctuating effective magnetic field. The physics of the spin dephasing in this inhomogeneous magnetic field is governed by the so-called *motional narrowing*, that also introduces another relevant timescale, as we now see.

Let us consider a spin precessing about a given axis with a Larmor frequency Ω. This frequency may change randomly between $-\Omega$ and Ω, which means that the spin rotates clock- or counterclockwise. Let us assume that a correlation time τ_c determines the probability that the spin continues its precession in the same direction, or changes it. During this time τ_c, a phase is accumulated $\delta\varphi = \Omega \ \tau_c$. If we now consider the spin precession as a random walk with this precise step $\delta\varphi$, after N steps, we simply have that the spread of the total accumulated phase is $\gamma = \delta\varphi \ \sqrt{N}$. On the other hand, the number N depends on time and is indeed equal to t/τ_c. Identifying the phase relaxation time t_φ with the time at which the phase spread reaches unity, we have that $1 = \delta\varphi^2 t_\varphi/\tau_c$. Finally we get the important result

$$\frac{1}{t_\varphi} = \Omega^2 \tau_c$$

The inverse relation between the two times is characteristic of the motional narrowing, and implies that the longer the correlation time, the smaller the phase relaxation time, and vice versa. In our language, the motional narrowing is related to T_2 and is the main source of spin dephasing. For conduction electrons, to a very good approximation, the relation $T_2^* = T_2$ holds.

In the case of electrons bound to impurities or quantum dots, the inhomogeneities are static and the g-factor-induced broadening due to spatial inhomogeneities plays an important role. Nevertheless, thanks to a technique known as spin-echo, it is possible to suppress these reversible phase losses, and the sole contribution to T_2 comes from the

homogeneous dephasing. For example, the time T_2^* has been measured in lightly n-doped GaAs samples, yielding values ~ 5 ns [23]. In general, T_2 is the quantity of most interest in quantum computing and spintronic, whereas T_1 is usually easier to measure.

However, in electronic systems at relatively weak magnetic fields, the useful relation $T_1 = T_2$ holds for isotropic and cubic solids (if this last condition is not fulfilled, an anisotropy factor of order unity is introduced) [24]. To determine the validity of this equality, we must resort again to the correlation time τ_c introduced for the motional narrowing. The phase losses occur during time intervals of τ_c, and in consequence $1/\tau_c$ gives the rate of change of the effective magnetic field. If this rate is such that $1/\tau_c \gg \gamma B_0$, then $T_1 = T_2$. For electrons, τ_c can be identified either with the momentum scattering time or with the time of interaction of the electrons with phonons or holes. As they can be as small as a picosecond, the equality between T_1 and T_2 is satisfied up to several Tesla. In many cases, therefore, a single term τ_s is used to refer to spin relaxation or spin dephasing, indistinctly. In the experiments of our interest, since the magnetic field is weak, we will use τ_s, and call it the spin-relaxation time, making it clear that the spin decay will be driven by the spin-orbit coupling.

We finally mention that in our discussion about spin relaxation, we deal with many-spin systems. In the context of quantum computation, another term is utilized for the spin dephasing of a single -or few- spin, namely the spin decoherence. But we do not discuss it in what follows.

The experimental results that motivated the first part of our work are presented in the next part, while the techniques are succinctly described afterwards.

1.3.3 The experiment

As we have mentioned, the first part of this thesis deals with GaAs samples, doped with Silicon, and is inspired in the work of Kikkawa and Awschalom [25]. These authors measured in 1998 the spin relaxation time and observed the influence of the doping on the spin relaxation. Interestingly, relaxation times longer than 100 nanoseconds for a doping densitiy of the order of 10^{16}cm^{-3} were reported. Four years later, Dzhioev

and collaborators [26] carried out similar experiments, but they swept a larger range of donor densities, establishing a more accurate value for the longest relaxation time and the corresponding density. These valuable experiments raised the interest of the spintronics community and many attempts were performed to explain the results. The experiment of Dzhioev *et al.* showed very clearly (Fig. 1.4) that the longest spin relaxation time was in the proximity of the Metal-Insulator transition density, that occurs within the impurity band of a n-doped semiconductor. The physics around this critical point is still not understood due to the competition of disorder and electron-electron interaction.
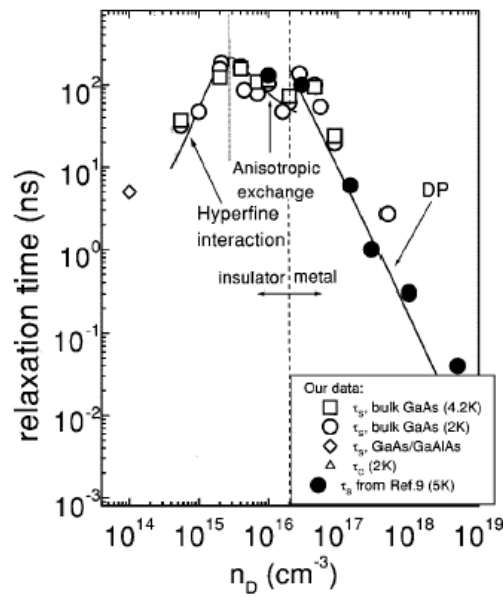
Figure 1.4: The spin-relaxation time at low temperatures as a function of the doping density (labeled as n_D) obtained in different experiments is shown. Open symbols correspond to the optical orientation data from Ref. [26], while the solid circles are the results from a Faraday Rotation experiment from [25,27]. Solid lines correspond to parameter-free theoretical estimates, considering the relevant spin-relaxation mechanism indicated by the labels: DP for Dyakonov-Perel, anisotropic interaction, and hyperfine interaction. Taken from Ref. [26]

16

Our aim is to tackle the problem of the spin relaxation on the metallic side of the MIT, and close to it. The identification of the dominant spin-interaction giving such long relaxation times is one of our major goals.

As we will later see in this chapter, the spin relaxation times for different density values far away from the critical one have been understood in terms of various existing theories. Nevertheless, none of these can be applied to the precise density range near the metal-insulator transition that is the center of our attention. Before describing these theories, we quickly review the experimental techniques involved in the measurements.

1.3.4 Experimental techniques

We briefly describe here the different experimental techniques encountered in the literature reporting spin relaxation measurements.

In Ref. [25], Kikkawa *et al* used the so-called Time-resolved Faraday rotation (TRFR) technique, with a temporal resolution going from femto to nanoseconds. This *pump-probe* technique uses the Faraday rotation as the fundamental principle. The initial circularly polarized light (pump) creates a net magnetization in the sample, and subsequently, with a time delay Δt, a second linearly polarized light crosses the sample (probe). The angle of polarization changes according to the degree of magnetization present in the system, and by changing the time delay Δt, a time-resolved observation is obtained. The TRFR was also used in lightly ($< 2 \times 10 cm^{-3}$) doped n-GaAs to measure spin-flip times as a function of magnetic field and temperature [23, 28].

The experiment of Dzhioev *et al.* used the combination of the optical orientation and the Hanle effect, which is the depolarization of the photoluminescence with a transverse magnetic field. The polarization created by the initial circularly polarized light is suppressed by the presence of a transverse magnetic field, and therefore, by measuring the corresponding photoluminescence polarization, the spin-relaxation can be inferred. In this case, the degree of spin polarization is detected by observing circularly polarized luminescence coming from the recombination of the spin-polarized electrons and holes.

In both cases, the initial step is to create an electron-hole pair by circularly polar-

ized light (optical spin orientation). The hole loses very rapidly its initial spin state and it recombines with an unpolarized equilibrium electron (the probability of recombination with a photoexcited electron is negligible under low pump intensity). Thus, spin-polarized photoexcited electrons eventually create a spin polarization accumulation in the crystal.

A totally different technique was also applied for measuring the spin-relaxation in n-doped bulk semiconductors. It is based on the spin noise spectroscopy [29], and it maps the ever present stochastic spin-polarization fluctuations of free and localized carriers at thermal equilibrium and the Faraday effect onto the light polarization of an off-resonant probe laser. The advantage of this tool over other methods is that it measures the disturbance-free spin dynamics in the semiconductors with high accuracy, and undesired effects such as carrier heating or injection of interfering holes are not present. Employing this technique, the spin-relaxation rate in samples with doping densities close to the metal-insulator transition was measured, for temperatures between 4 K and 80 K. A clear difference in the spin-relaxation times was observed when varying the doping densities and moving from the regime of localized electrons to that of free electrons. We discuss about this in more detail in Chap. 4, and only mention here that the longest spin relaxation time at the critical density was verified for the lowest temperature range, up to 70 K [30].

1.3.5 The existing theories

Having already identified the different doping density regimes, we can now move to the existing theories in terms of which the different spin relaxation times measured in the experiment can be explained. However, we insist that none of them can be applied to the metallic regime of the impurity band, which will be covered by our theory afterwards.

Hyperfine interaction

For the smallest doping densities, the different impurities are far from each other and one expects electrons to be deeply localized. In this case, the measured spin-relaxation

times can be understood by appealing to the hyperfine interaction. On the extreme side of very low donor concentration, the electrons are isolated and precess independently in the random static nuclear fields of the impurity domains. The origin of the hyperfine interaction is the coupling between the electrons and the magnetic field produced by the atomic nuclei. This magnetic coupling affects the localized spins, such as those confined in quantum dots or bound to donors, and it may produce spin dephasing as well as single spin decoherence. The interaction, although it is suitable for localized electrons, was shown to be too weak for itinerant electrons (free electrons in metals or bulk semiconductor) in Ref. [31].

The hyperfine Hamiltonian reads

$$H = \frac{2}{3}\mu_0 g_0 \mu_B \sum_i \hbar \gamma_{n,i} \mathbf{S} \cdot \mathbf{I} \, \delta(r - \mathbf{R_i}) \tag{1.1}$$

where μ_0 denotes the vacuum permeability, μ_B the Bohr magneton, $g_0 = 2.0023$ is the free-electron g-factor, i labels the nucleus at position $\mathbf{R_i}$, while $\mathbf{S}$ and $\mathbf{I}$ corresponds to the electron spin operator and the nucleus spin operator, respectively, both expressed in units of $\hbar$. $\gamma_{n,i}$ stands for the nuclear gyromagnetic ratio. It can be shown that this interaction can be expressed as $A(\mathbf{IS})$ (Fermi contact interaction), with A being proportional to the square of the electron wave function at the location of the nucleus [32]. Both the properties of nuclei involved and the degree of localization of the electron, which may be spread over many lattice sites (typically $10^4 - 10^6$) are decisive to determine the strength of the interaction. In Si, for instance, most of the nuclei carry no spin: only the isotope ^{29}Si with spin 1/2 produces hyperfine interaction, but its natural abundance is too low (4.6%) [9]. In GaAs, on the other hand, all the nuclei have spin 3/2, whence the stronger hyperfine interaction of a localized electron in it.

There are in general three mechanisms where the hyperfine interaction plays a major role in the electron spin relaxation. The first of them deals with independent evolution of the nuclei and electron spins, i.e, small orbital and spin correlations. The spatial variations of B_n -the magnetic field experienced by the electron- lead to inhomogeneous

dephasing of the spin ensemble. This dephasing has been measured in Si in Ref. [11], the same experiment that inspired Anderson. If this effect is removed by a spin-echo technique, then the temporal fluctuation of B_n due to nuclear dipole-dipole interaction leads to irreversible dephasing and decoherence of the electron spin, which makes the second case of the list. The third regime corresponds to the hopping regime of the electron between adjacent states and thus important at finite temperatures. Here the spin precession due to B_n is motionally narrowed, as explained before, and limited by the direct exchange interaction, which causes individual spin decoherence.

In the experiment by Dzhioev *et al.*, the authors attribute the increase in the relaxation time with dopant density for the lowest density range to the dynamical averaging of the hyperfine interaction, where the electron passes less time in each localization domain as the density increases, interacting for shorter time with more nuclei, thus diminishing the effect of the nuclei-spin fluctuations.

Anisotropic exchange

As we further increase the doping density, electrons centered around neighboring impurity centers start having some degree of overlap, and therefore the exchange interaction becomes relevant. It is worth mentioning here that since we discuss the case of two localized electrons in what follows, the same physics does indeed apply to double quantum dots, with an electron in each of them.

The origin of the exchange term is in the Coulomb interaction between electrons, that gives a spin-dependent energy contribution as we require the total wave function - including spin- of the two-electron system be anti-symmetric with respect to the exchange of their coordinates. What this means is that if the spins of the electrons are parallel, the spatial coordinate part of the wave function must be antisymmetric, meaning that it must change sign upon exchanging the spatial coordinates of the electrons:

$$\Psi_{\uparrow\uparrow}(\vec{r}_1, \vec{r}_2) = -\Psi_{\uparrow\uparrow}(\vec{r}_2, \vec{r}_1)$$

This ultimately implies that electrons with parallel spin tend to be far apart, reducing

their mutual repulsion, and consequently diminishing the electrostatic energy.

Let us now consider the effect of the spatial anisotropy arising from the crystal environment and introduce the *isotropic* exchange interaction. The spins of two localized electrons are actually coupled by two kinds of interaction, the magnetodipole and the exchange interactions. In an isotropic system, the latter is described by the Heisenberg Hamiltonian

$$H_{ex} = 2J\mathbf{S}_A \cdot \mathbf{S}_B$$

where J is the exchange coupling constant, and $\mathbf{S}$ denote the spin operator of the corresponding electron. Interestingly, this isotropic (or scalar) interaction conserves the total spin of the two electrons, and consequently, it does not cause any spin relaxation. However, in the presence of a crystal environment, the previous expression should be generalized [33] to

$$H_{ex} = A_{\alpha\beta}S_{A\alpha}S_{B\beta}$$

where A turns out to be a second-rank tensor defined by the structure symmetry. Anisotropic interactions of this kind appear in crystal structures lacking inversion symmetry, as in bulk semiconductors with zincblende and wurtzite structures. The spin-orbit coupling gives rise to this anisotropic part of the exchange term, whose form is also known as the Dzyaloshinskii-Moriya interaction, and it may even dominate over the isotropic part. Although the spin-orbit interaction disappears on averaging over the localized wave function of a single-electron state, it is no longer the case for two electrons at a pair of donors close to each other, or quantum dots alternatively.

Qualitatively, the process can be described in the following way, as Kavokin explained in Ref. [33]. If we take two sites A and B, and consider an electron tunneling from one site to the other one, it will experience the influence of the spin-orbit field. This field makes the spin rotate a small angle. Reversely, the tunneling of the other electron in the opposite direction is accompanied by a spin rotation through the same angle, but in the opposite direction, because the internal field arising from the SOC, changes its polarity for the backward motion. This makes that an interchange of the electrons also implies a relative rotation of their spins. As a result, we expect to have an effective coupling

between these rotated spins, whose relative angle is determined by the SOC. In other words, we end up with an interaction between tipped spin operators of the form

$$H_{ex} = 2J\mathbf{S}'_A \cdot \mathbf{S}'_B$$

If one wishes to express this interaction in terms of the original spin operators $\mathbf{S}_A$ and $\mathbf{S}_B$, the appropriate transformation yields

$$H_{ex} = 2J\mathbf{S}_A\mathbf{S}_B\cos(\gamma) + \frac{2J}{b^2}\left(\mathbf{b}\mathbf{S}_A\right)\left(\mathbf{b}\mathbf{S}_B\right)\left(1 - \cos(\gamma)\right) + \frac{2J}{b}\mathbf{b}\left(\mathbf{S}_A \times \mathbf{S}_B\right)\sin(\gamma) \quad (1.2)$$

where γ is the relative angle of rotation and b stands for the internal magnetic field produced by the spin-orbit coupling. The last two terms correspond to the anisotropic contribution [33]. Although we will not work out the full derivation of the anisotropic Hamiltonian, we just emphasize some important aspects of it. The first of them is related to the general structure of the electron wave function. As mentioned before, we consider semiconductors lacking inversion symmetry, where an effective spin-orbit coupling in the conduction band (this is further explained in Chap. 2) presents the general form

$$H_{SOC} = \mu_B g\mathbf{B}_{SOC}(\vec{k}) \cdot \mathbf{S}$$

where $\mathbf{B}_{SOC}$ represents an effective spin-orbit field that depends on the wave vector, only via odd powers of $\vec{k}$.

As it is usually very weak, it has no incidence on the binding energy and the wave function shape near the localization center. However, away from it, it strongly modifies the wave function, even though the potential energy at large distances can be neglected. As shown by Kavokin [34], the wave function at a (large) distance r from the center is

$$\Psi \sim e^{-r/r_0}\exp\left(i\frac{m\mu_B g\mathbf{B}_{SOC}(\vec{k} = \vec{r}/(rr_0)) \cdot \mathbf{S}}{\hbar^2}\frac{r}{r_0}\right)$$

where the length scale $r_0 = (\sqrt{\frac{2mE_B}{\hbar^2}})^{-1}$ has been introduced. E_B denotes the binding energy, and m the effective mass of a conduction electron. The second part of this formula resembles a spin rotation operation, meaning that if near the center the spin is pointing along a certain axis, then at a given distance r the spin have the same projection but on an turned axis, whose angle is equal to

$$\gamma(r) = \frac{m\mu_B g\mathbf{B}_{SOC}(\vec{k} = \vec{r}/(rr_0))r}{r_0}$$

around the spin-orbit field B_{SOC}. This asymptotic behaviour has an influence on the spin dynamics. To show this, the next step is to consider the two centers A and B, and notice that the two wave functions of the electrons localized at each site are no longer orthogonal, even though they have opposite spin projection (along a common axis). This implies at the same time that an electron tunneling from, say, site A to site B will turn its spin through an angle given by $\gamma(\mathbf{R}_{AB})$. If the site B is occupied by another electron (described also by an asymptotic wave function), the exchange interaction will couple both electrons which are defined in different primed coordinate frames, as shown before. Upon transforming this primed Hamiltonian back to a common frame, the resulting exchange interaction (1.2) accounts for the full process.

From this description, yet not totally formal, it is reasonable to expect that a stronger overlap between the wave functions, due to a increasing doping density for example, will produce a stronger exchange and yield lower values for the spin-relaxation times. This situation is consistent with the dip observed in Fig. 1.4 for a doping density just below the critical one. Indeed, Kavokin showed that the motional narrowing of the anisotropic term for two conduction-band electrons localized at shallow centers (donors or quantum dots) accounts for the decrease of τ_s in the intermediate density region $3 \times 10^{15} cm^{-3} < n < n_c$ of the experiment of Dzhioev *et al.*.

If we now leap over the critical density and consider the extreme case of highly doped samples, beyond the hybridization density, where the conduction band is mainly pop-

ulated, we expect the usual spin-relaxation mechanisms for conduction electrons to be applicable. We address two of them in the following section.

The Elliot-Yafet mechanism

We briefly describe here the spin-relaxation mechanism that despite not being suitable in our specific context, it certainly helps to understand the theory developed later for the impurity band. In a regular array of ions, the periodic potential V_{cry} induces a spin-orbit coupling term

$$H_{SOC} = \frac{\hbar}{4m_0^2}(\nabla V_{cry} \times \mathbf{p}) \cdot \sigma$$

where m_0 is the free electron mass, $\mathbf{p} = -i\hbar\overline{\nabla}$ is the linear-momentum operator, and σ is the spin operator. This term couples different single-electron Bloch states, and therefore, they are no longer σ_z eigenstates, but a mixture of spin-up and spin-down. Elliot first considered the case of a metal with a center of symmetry, for which these modified eigenstates read

$$\Psi_{\mathbf{k}n\uparrow}(r) = \left[a_{\mathbf{k}n}(\vec{r})|\uparrow\rangle + b_{\mathbf{k}n}(\vec{r})|\downarrow\rangle]e^{i\overline{\mathbf{k}}\cdot\vec{r}}\right] \tag{1.3}$$

$$\Psi_{\mathbf{k}n\downarrow}(\vec{r}) = \left[a^*_{-\mathbf{k}n}(\vec{r})|\downarrow\rangle - b^*_{-\mathbf{k}n}(\vec{r})|\uparrow\rangle\right]e^{i\overline{\mathbf{k}}\cdot\vec{r}}\right] \tag{1.4}$$

where the different coefficients $a_{\mathbf{k}n}$ and $b_{\mathbf{k}n}$ measure the degree of spin mixture of the state in the band n, for each wave vector $\mathbf{k}$. The spatial-inversion operator and the time-reversal operator (both of them commute with the Hamiltonian) connect these two degenerate states. The labels $\uparrow$ and $\downarrow$ are justified by the fact that the spin-orbit coupling is weak and consequently, the typical value of $|b_{\mathbf{k}n}| << 1$. This estimation can be done in the following way: since H_{SOC} has the periodicity of the lattice, it only connects states with opposite spin but the same $\mathbf{k}$ at different bands n. If a typical coupling matrix element is given by $|H_{SOC}|$, and we denote the distance between these states by a gap

$\triangle E$, then

$$b \simeq |H_{soc}|/\triangle E,$$

which is usually much smaller than 1, because the spin-orbit coupling is much smaller than a typical energy gap. Given this, we observe that some mechanism of momentum scattering will produce spin relaxation, because states with different **k**'s have different spin orientations. Or to put this differently, every time the electron suffers a scattering event that changes its momentum, its spin state may change as well. In Fig. 1.5, the process is sketched. At each scattering on a center (phonon, impurity, *etc*), the electron has a small chance to flip its spin. Elliot's formula [9] states that the spin-relaxation rate is proportional to the momentum relaxation rate

$$\Gamma_s \equiv \tau_s^{-1} \sim \langle b^2 \rangle \Gamma_p$$

where $\Gamma_p = \tau_p^{-1}$ is the momentum relaxation rate determined by "up" to "up" scattering [35]. The spin-flip length turns out to be proportional to the mean-free path (or to the diffusion constant):

$$\lambda_s = \sqrt{D\tau_s}$$

The Elliot-Yafet mechanism is known to be very effective in metals, but it also enters the physics of semiconductors. It is applicable for conduction electrons in the presence of an inversion symmetric crystal structure. When this last condition is not fulfilled, another mechanism appears and competes with it, namely the Dyakonov-Perel mechanism that we discuss in the sequel.

D'yakonov-Perel

The inversion symmetry in semiconductors can be broken by the presence of two distinct atoms in the Bravais lattice. This happens to be the case in groups III-V (such as GaAs) and II-VI (ZnSe) semiconductors. In heterostructures, instead, the source of this breaking is the asymmetric confining potential. In general, in asymmetric systems the spin-orbit interaction leads to the Dyakonov-Perel mechanism for conduction electrons. Due to the lack of translational invariance, the eigenenergies do no longer

satisfy $E_{\mathbf{k}\downarrow} = E_{\mathbf{k}\uparrow}$, but since the time-reversal symmetry is still present (as long as no external magnetic field is applied), the following relation holds $E_{\mathbf{k}\downarrow} = E_{-\mathbf{k}\uparrow}$. The spin splitting so produced is equivalent to consider an intrinsic $\mathbf{k}$-dependent magnetic field $B_i(\mathbf{k})$, perpendicular to $\mathbf{k}$, that induces a Larmor precession around it with a frequency of $\Omega(\mathbf{k}) = (e/m)B_i(\mathbf{k})$. This intrinsic magnetic field derives (and depends on) from the spin-orbit coupling in the band structure, whose effective interaction term reads

$$H(\mathbf{k}) = \frac{1}{2}\hbar\sigma \cdot \Omega(\mathbf{k})$$

where σ are the Pauli matrices and $\mathbf{k}$ is the momentum state label of the electron in the conduction band. Therefore, the combination of the momentum relaxation described by a characteristic time τ_p and the momentum-dependent spin interaction gives rise to spin dephasing. If we further define Ω_{av} as the average of the intrinsic Larmor frequency over the electronic momentum distribution, two different cases can be distinguished.

If $\Omega_{av}\tau_p \geq 1$, the momentum relaxation time is long enough as to permit the spin to precess a full cycle before being scattered to another momentum state. In general, the
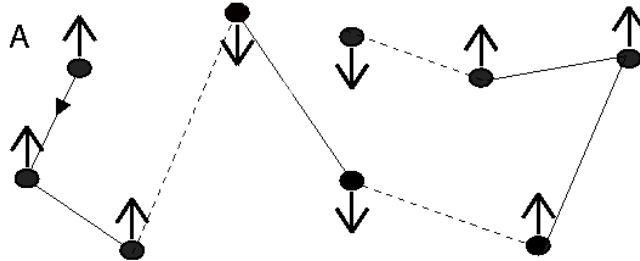
Figure 1.5: The Elliot Yafet mechanism, relevant for conduction electron in centrosymmetric crystals, is sketched. The spin-orbit interaction makes a spin-up (down) Bloch state bear a small contribution of spin-down (up) amplitude. Impurities, boundaries or phonons, even being spin independent potentials, may induce transition between quasi-up and quasi-down states [35].

spin dephasing time is given by $1/\tau_s \approx \triangle\Omega$, where $\triangle\Omega$ is the width of the distribution sampled by the ensemble of spins. For $t < \tau_p$, all the spins dephase reversibly, but afterwards, this coherence is irreversibly lost due to randomizing scattering.

In the other case, $\Omega_{av}\tau_p < 1$, the electrons changes its momentum rapidly and so does the magnitude and direction of the intrinsic magnetic field. The time step τ_p determines the "small" rotation angle of the spin $\delta\Phi = \Omega_{av}\tau_p$ *between* two successive scattering events. The spin phase then accumulates diffusively and after a certain number of steps given by t/τ_p, the total phase is calculated as

$$\Phi(t) \approx \delta\phi\sqrt{t/\tau_p}$$

The presence of the square root coming from the random walk picture must be noticed. If we now define τ_s as the time at which $\Phi(\tau_s) = 1$, then we come across the usual "motional narrowing" equation

$$1/\tau_s = \Omega_{av}^2\tau_p$$

In this case, the total phase accumulated by a single electron consist of a *sum* of different Larmor frequencies (randomly taken) multiplied by τ_p, such that $\Omega(\mathbf{k})$ is sampled by the distribution of these *sums*. Its variance is, according to the central-limit theorem, very small. Randomizing is very effective in this case because there are other spins bearing different momentums, and thus precessing with different Larmor frequencies.

The simple picture of the Dyakonov-Perel mechanism is presented in Fig. 1.6. As the spins in the bands are no longer degenerate, the spin-up state carries a different energy from a spin-down state with the same momentum. The electrons moving throughout the sample experience an internal magnetic field, dependent on momentum, that makes the spin precess along such field, until the electron momentum changes by scattering due to a impurity, boundaries, or phonons. The precession then continues, but along a different axis, because the $\vec{k}$ has changed. In this case, unlike the Elliot mechanism, the smaller the momentum scattering time the longer the spin relaxation time. A large momentum scattering rate prevents the spin to perform a full cycle of spin rotation, whereby spin
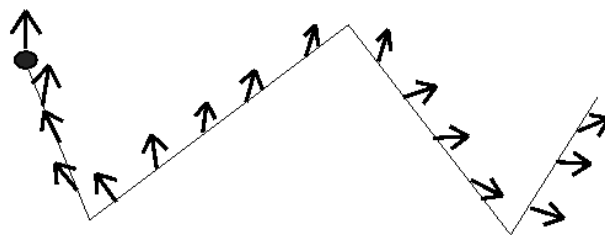
Figure 1.6: The Dyakonov-Perel mechanism applies in non-centrosymmetric structures, where the spin bands are no longer degenerate, and a spin up state with a given momentum has a different energy from the spin down state with the same momentum. Therefore, the effective picture is an internal k-dependent magnetic field, along which the spin precesses. When the electron is scattered by a phonon, a boundary or an impurity, the precession continues along a different axis [35].

relaxation would be enhanced.

As it has been pointed out, the Dyakonov Perel mechanism is suitable for conduction electrons with a well-defined crystal momentum $\vec{k}$. In the case of doped semiconductor, for large densities (Fig. 1.4) where the conduction band is well populated, the spin-relaxation times can be understood in terms of this mechanism. For a smaller density, just above the critical point, we enter the metallic regime of the impurity band, and therefore the aforementioned theory is not applicable. We have developed in this work a suitable theory for treating the spin relaxation in this case, whose results can be found in Ref. [36]. However, we anticipate that the notion of spin diffusion will be used upon constructing our description for the spin-relaxation in the impurity band.

1.4 Spin in nanostructures

So far we have dealt with electrons and spins in bulk systems, where the electron moves in the three directions. In low-dimensional systems, by contrast, the electron motion is

restricted to two, one, or even zero dimensions. Nevertheless, bulk and low-dimensional physics are not completely dissociated. For example, lightly doped GaAs has been studied in view of the similar spin properties observed for electrons localized on isolated donors and for electrons localized in quantum dots [23], since in both cases the electron is effectively confined in a zero dimensional enclosure. As it is mentioned by Kavokin in Ref. [34], an understanding of the spin behaviour in the impurity band of bulk semiconductors would be a proper basis for the study of localized electronic spins in wells or dot arrays. However, the confinement potential in nanostructures is in general less isotropic than the localizing potentials of donors in bulk systems.

The importance of low-dimensional semiconductor systems is related to their great flexibility in manipulating charge and also spin properties of the electronic states. Here, spin relaxation is also caused by random magnetic fields originating either from the base material or from the heterostructure itself, and the Dyakonov-Perel and the Hyperfine interaction are believed to be the most relevant mechanisms [9]. As the spin relaxation and spin dephasing in these systems should be reduced for technological applications, a great deal of research has been devoted to understand them.

From the point of view of applications, an additional motivation for studying low-dimensional spin-based electronics is its close connection to the current trend in technology of requiring smaller and smaller devices. In this sense, spintronics also belongs to the field of nanotechnology.

In the second part of this thesis we concentrate on a semiconductor quantum dot, explained in Chap. 5. Before that, we briefly describe the various low-dimensional systems, starting with the two-dimensional case.

1.4.1 Quantum wells

An example of low-dimensional system is the quantum well. In this case, the carriers are confined on a planar region, whose thickness is comparable to the de Broglie wavelength of the carriers. The setup consists of an ultra-thin layer of a small band gap semiconductor between larger gap semiconductor materials, that effectively forms an

attractive potential in which electrons are trapped. In heterostructures made of GaAs and AlGaAs, the two-dimensional electron gas (2DEG) is formed between the spacer (AlGaAs) and the buffer layer (GaAs) [37]. In these systems, electrons spins have been successfully manipulated by means of electric fields, which allows to set and control the g-factor value -so varying the coupling between the magnetic field and the spin- throughout the well, and thereby tuning the electron spin resonance [37, 38]. An equivalent g-tensor modulation resonance technique that used a gigahertz electric field was proposed in Ref. [39]. After it, a different approach that also made use of time-dependent electric fields, was put forth by Rashba and Efros [40, 41]. These electric fields change the orbital state of the electrons, and couple to the spin via the spin-orbit coupling. Their alternative gate-voltage induced spin resonance mechanism, known as the Electric Dipole Spin Resonance (EDSR), was later on extended for quantum dots.

1.4.2 Nanowires

Another example of a lower dimensional system is a wire, in which the electrons are confined to one single dimension, as in a rod or a whisker. They are typically grown by the so-called metalorganic vapor phase epitaxy (MOVPE), a chemical -in contrast to physical- method used to grow thin films of a given material. The desired atoms diffusing through the gas phase deposit onto the wafer (substrate surface) atomic layer by atomic layer. The chemicals are vaporized and injected into a reactor together with other gases, where a critical chemical reaction takes place, turning the chemicals into the desired crystal. A compound semiconductor can also be grown using this technique [42]. This procedure needs a seeding nanoparticle, deposited on the substrate, in order to induce the process. The nanoparticle size determines the diameter of the nanowire, which can typically reach 100nm [43]. The structural properties of the nanowires are usually studied using a high-resolution transmission electron microscopy (TEM).

Nanowires have been proposed for several practical applications. In Ref. [44], the possibility to use a ferromagnetic gate as a spin-polarization filter for one-dimensional electron systems was put forward. Nowadays, an additional interest on these wires is
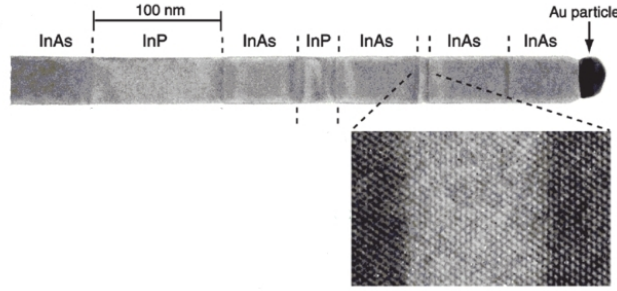
Figure 1.7: A transmission electron microscopy of InP barriers of various sizes inside InAs nanowhiskers. In the lower figure the crystalline perfection is showed, along with the interface abruptness. The InAs whisker diameter is 40 nm [46].

rising, because in contact with normal (gold) and superconducting electrodes, they can be used for the seek of the novel Majorana fermions [45]. In this thesis we do not deal with this interesting subject.

An appealing feature about the nanowires is the possibility to host a quantum dot, by confining the electron in the axis of the wire. The electron dwelling in the dot is a conduction band electron of the underlying structure that is affected by the confinement effects. A necessary step for achieving such a setup is the formation of one dimensional heterostructures, in which a single whisker contains various segments, with abrupt interfaces and heterostructure barriers of varying thickness. The picture in Fig. 1.7 shows the transmission electron microscopy (TEM) image of a nanowhisker made of InP and InAs pieces, with a remarkably sharp interface between them, also displayed.

By using these InAs nanowires, the group in Sweden headed by L. Samuelson [47] came across a novel device. They designed a few-electron quantum dot in these semiconductor nanowires, by introducing a double barrier made of InP heterostructures. The quantum dot is hosted between the barriers, and by increasing the gate voltage, they added electrons one by one into the dot, up to 50. This is the type of quantum dot that we study, and we next describe it in more detail.
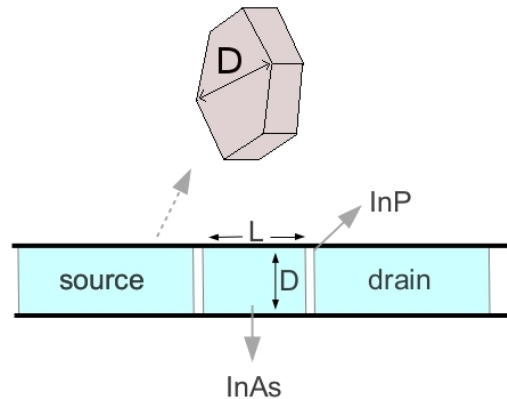
Figure 1.8: An outline of the nanowhisker quantum dot. Tho InP tunnel barriers define the quantum dot in the InAs nanowire. The lateral side facets form a hexagonal cross section with presumably hard wall conditions [48].

1.4.3 Quantum Dots

A quantum dot is a zero-dimensional system in which the motion of the electron is confined in its three dimensions. As such, the energy spectra presents discretized levels. The electron spin in a semiconductor quantum dot is a promising candidate for quantum information applications, and therefore much effort has been devoted to understand and identify the effects producing the loss of information either via decoherence or relaxation. The original proposal of implementing a two-level system -associated to the electron spin- as a quantum bit (or qubit) in a quantum dot was published in 1998 by D. Loss and D. DiVincenzo [14]. Many theoretical and experimental works followed thereafter, and many technical pitfalls have been overcome, eventually leading to great advances. Only in recent years systems where the properties of individual electrons can be measured have been achieved. Among those, the quantum dot is particularly appealing since it constitutes the building block for scalable solid-state quantum computers. The central and major challenge notwithstanding remains in the present: how to manipulate the spin in a short time before it loses its (quantum) initial state. The simplest idea would be to think about resonant magnetic fields. In Ref. [49], the group of L. P. Kouwenhoven

claimed to control coherently a single spin in a dot by applying short bursts of oscillating magnetic fields. The problem is that the field involved cannot be spatially localized, the strength of it renders the time to reverse the spin too slow, and the experiment has to be performed at very low temperatures and at high frequencies [50]. All these shortcomings make the experiment as well as the technological application a very hard task. A more desirable approach was conceived in 2007 by Nowack and collaborators [51], where the coherent control of the spin by means of oscillating electric fields generated in a local gate was performed. They reported induced coherent transitions (Rabi oscillations) as fast as 55 nanoseconds, and their analysis indicated that the spin-orbit interaction was the driving mechanism. The manipulation times obtained in these GaAs quantum dots, about 110 ns for a spin flip, were not fast enough, hindering a quick and precise control. This deficiency was partially improved again by Kouwenhoven's group [17]. Here the one dimensional wire was made of indium arsenide, whose spin-orbit coupling is known to be stronger. In this spin-orbit qubit, spin-flip times of about 8 ns were obtained. The quantum dot in this latter example is defined by using an array of 5 contiguous gates (no structuraly defined tunnel barriers are present), where two quantum dots are hosted. One of them serves only for reading purposes. Operating in the Coulomb blockade regime, that prevents the electron from escaping from the dot, a microwave-frequency electric field applied to one of the gates forces the spin inside the wire to oscillate, so inducing resonant transitions between spin-orbit states when the a.c frequency is equal to the Larmor frequency. The Electric Dipole Spin Resonance mechanism, already mentioned for 2D systems and extended for quantum dots in Ref. [52], is at the basis of the comprehension of the experimental results.

Another property of interest in quantum dots is the effective g-factor. It has been measured in InAs nanowire quantum dots for various dot sizes in Ref. [48], where a strong dependence on the dot sizes is exhibited in the case in which few electrons occupy the lowest discretized energy states. This sensitivity leads to a possible setup for individually addressable spin qubits, if the nanowire has multiple dots with different g-factors along it.

Our reference to the specific material InAs is not casual. We consider an quantum dot like the one sketched in Fig. 1.8. The dot is hosted between the two InP tunnel barriers. Our point of interest is the intrinsic spin-orbit coupling related to a particular property of these systems: the crystal structure of InAs presents a zincblende form in the bulk phase, but it acquires a wurtzite-type structure when grown unidimensionally [53]. Moreover, a crossover to the zincblende crystal structure has been observed as a function of the wire diameter [54], and theoretically explained by classical nucleation modeling. Logically, the commonly cited form of the effective Dresselhaus spin-orbit coupling for zincblende (cubic-in-k) is not expected to be applicable to the wurtzite case. Indeed, the effective spin-orbit coupling for the conduction band of WZ contains a linear-in-k term, firstly proposed in Ref. [55]. In addition, and only recently, a cubic-in-k term has been shown to be present [56] as well, and the corresponding coupling parameters have been calculated [57].

In our study about spin-orbit effects in InAs-based quantum dots, we treat both terms on equal footing (see Ref. [58]).

1.5 Outline of this thesis

The outline of the thesis is as follows. In Chap. 2 we review the theoretical formalism related to our work. We begin by exploring the origin of the spin-orbit interaction starting from the Dirac equation. After this and by way of a digression, we introduce basic concepts of group theory, that provide us with a convenient language to treat the symmetries encountered in crystal structures. The zincblende and the wurtzite structures are there described. The chapter finishes with the effective theories whereby we can deal with the behaviour of an electron without taking into account all the microscopic details concerning the crystalline structure.

In Chap. 3 we present our characterization of the impurity band, and more precisely, our study about the effect of the spin-orbit interaction on the localization of the wave function. We consider a suitable parameter to measure the degree of spatial extension of

the calculated eigenfunctions, and how it changes upon increasing the spin-orbit coupling strength, in this case, given by an extrinsic-type SOC associated to the impurities.

In Chap. 4 we tackle our main subject related to spin-relaxation on the metallic side of the metal-insulator transition of a doped semiconductor. In addition to the extrinsic term, we add the Dresselhaus (cubic-in-k) SOC derived for zincblende structures. Our approach to the spin diffusion in the impurity band is carefully explained, along with the complete analytical treatment of the density dependence of the spin relaxation for dopant densities slightly larger than the one corresponding to the metal-insulator transition. We also performed some numerical calculations for the estimation of the spin relaxation by considering the time evolution of an initial state. After presenting the numerical results, we compare and discuss the agreement of our theory with the experiment of Fig. 1.4.

In Chap. 5 we concentrate on the behaviour of a conduction electron confined in a cylindrical quantum dot. The effective spin-orbit coupling terms related to the wurtzite structure, here containing both a linear-in-k and a cubic-in-k contribution, are exactly treated. A two-dimensional system is firstly considered, and the energy dispersion as a function of k is derived analytically. A further confinement is imposed with cylindrical hard-wall boundary conditions to make up a pillbox-like quantum dot. Here, an equation for the discretization of the energies is found, and a numerical solution is thus implemented. The resulting g-factors are evaluated.

The conclusions brought about by our theoretical work, as well as the perspectives are in terms of further theoretical and experimental research discussed in Chap. 6.

Chapter 2

Spin-orbit interaction in semiconductors

2.1 Dirac-Spinor

The spin-degree of freedom associated with an intrinsi angular momentum **S** couples to a magnetic field exactly in the same way as a dipole magnetic moment does. This magnetic moment is related to **S** via the definition $\mu = g\mu_B \mathbf{S}$, where g is the g-factor and μ_B is the Bohr magneton. But in spite of this interaction, which has a classical form, the spin degree of freedom itself does not have any classical analog. Even though the spin emerges naturally in relativistic quantum mechanics, its existence is revealed *solely* by a linearization of the Schrödinger equation, without appealing to any relativistic theory, as it is elegantly exposed in [59]. Such *linearized* equation is equivalent to the usual Schödinger equation, but in contrast to the latter, this one is linear both in $(\partial/\partial t)$ and in $(\partial/\partial x)$. The Pauli equation can be thus derived and the correct value for the g-factor results. Here, however, we will follow the more conventional way of using a Quantum Electrodynamics framework, in order to treat the interaction of an electron with an electromagnetic field. The basic goal is to see how the **spin-orbit coupling** (SOC) comes out, or equivalently, to trace back its origin. For this, the Dirac equation will be unfolded, and the spin g-factor will appear as well. In the beginning we succinctly

sketch the derivation of the Dirac Equation, following [60]. The road map starts from the Schrödinger equation, followed by its relativistic counterpart, and we finish by deriving a new Schrödinger equation as a non-relativistic limit.

The Schrödinger Equation can be obtained by using the quantum prescription $\bar{p} \rightarrow (-i\hbar)\nabla$ and $E \rightarrow i\hbar\frac{\partial}{\partial t}$ for a conservative mechanical system

$$-\frac{\hbar^2}{2m}\nabla^2\psi + V\psi = i\hbar\frac{\partial\psi}{\partial t} \tag{2.1}$$

with m the free-electron mass, V a potential energy and $\hbar$ the Planck's constant.

On the other hand, leaving out the potential energy, the relativistic energy-momentum relation is

$$E^2 - p^2c^2 = m^2c^4$$

In the so-called covariant notation, this is expressed as :

$$p^\mu p_\mu - m^2c^2 = 0 \tag{2.2}$$

where $\mu = 0, 1, 2, 3$. The 0 component is associated to the energy (x_0 is the time coordinate), while the other three correspond to the momentum components. We note that the space and time coordinates appear on equal footing in this last equation. The Einstein notation has been used for the sum. For our purposes, it is enough to know that the super and subscript notation simply mean

$$a^\mu b_\mu = a^0 b_0 + a^1 b_1 + a^2 b_2 + a^3 b_3 = a^0 b^0 - a^1 b^1 - a^2 b^2 - a^3 b^3$$

where a and b are operators. Every time we want to rise the index of an operator, we have to multiply it by -1 only if $\mu = 1, 2, 3$. The 0-component remains the same. In relativistic language, $p_0 = E/c$ and $\bar{p} = (p_1, p_2, p_3)$ is the linear momentum operator. If we followed the aforementioned quantum prescription, we would arrive to the Klein Gordon equation :

$$\frac{-1}{c^2}\frac{\partial^2\psi}{\partial^2 t} + \nabla^2\psi = \left(\frac{mc}{\hbar}\right)^2\psi$$

The fact of being second order in t poses a problem based on the statistical interpretation of $|\psi|^2$. To circumvent this difficulty, Dirac sought an equation *linear* in $\partial/\partial t$, and

compatible with the relativistic energy-momentum relation (2.2). Dirac's proposition was to split the energy-momentum relation (2.2) in two parts :

$$p^\mu p_\mu - m^2 c^2 = (\beta^k p_k + m\,c)(\gamma^\lambda p_\lambda - m\,c) = 0 \tag{2.3}$$

thereby imposing the energy-momentum relation. If this equation is to be satisfied, then any of the two terms of the decomposition is a solution to the total problem. It also implies that the linear equation is attained. Remarkably, the simple requirement in eq. (2.3) leads to the conditions to be met by the $\beta's$ and $\gamma's$:

- $\beta^k = \gamma^k$

- the $\gamma's$ must be matrices

- the smallest dimension of these matrices can be 4×4

- $(\gamma^0)^2 = \mathbb{I}$

- $(\gamma^i)^2 = -\mathbb{I}$ for $i = 1, 2, 3$

- $\gamma^\mu \gamma^\nu + \gamma^\nu \gamma^\mu = 0$ if $(\mu \neq \nu)$ (the anti-commutation relation)

The last item defines an *algebra*, and there are several equivalent ways of representing the $\gamma's$. One of them is

$$\gamma^0 = \begin{pmatrix} \mathbb{I} & 0 \\ 0 & -\mathbb{I} \end{pmatrix}$$

and

$$\gamma^i = \begin{pmatrix} 0 & \sigma^i \\ -\sigma^i & 0 \end{pmatrix}$$

Each block in these matrices is a 2×2 matrix; $\mathbb{I}$ is the identity and σ_i are the Pauli matrices.

Another choice is the so-called *Majorana* basis. It takes up different expressions for the γ matrices, which of course satisfy the same algebra, and imply ultimately the existence of a particle that is its own antiparticle, i.e. a Majorana Fermion.

Back to our derivation, the usual substitution $p_\mu = i\hbar\partial_\mu$ is inserted into the eq. (2.3), and any of the two terms can be named the **Dirac Equation** :

$$i\hbar\gamma^\mu\partial_\mu\psi - m\,c\psi = 0. \tag{2.4}$$

Nevertheless, it must be noted that ψ is a four-component spinor; it is NOT a four-component vector, since it does not transform under the ordinary Lorentz rules. We mentioned that the spin-orbit coupling is our final objective, and therefore the effect of an electromagnetic field needs to be included. The requirement of preserving the gauge invariance dictates that the spatial and time derivatives must be replaced by

- $\frac{\hbar}{i}\nabla \to \frac{\hbar}{i}\nabla - \frac{e}{c}\vec{A}$

- $i\hbar\frac{\partial}{\partial t} \to i\hbar\frac{\partial}{\partial t} - e\phi$

where $\vec{A}$ is the magnetic vector potential and ϕ the electric scalar potential. In covariant notation, the Dirac equation including this quadripotential is

$$[\gamma^\mu(i\hbar\partial_\mu - \frac{e}{c}A_\mu) - m\,c]\psi(x) = 0. \tag{2.5}$$

In order to recover the Schrödinger equation, the linear time derivative can be separated from all the other terms by multiplying $(\gamma^0\,c)$ from the left

$$[\gamma^0\,c]\,[\gamma^0(i\hbar\partial_0 - \frac{e}{c}A_0) + \gamma^i(i\hbar\partial_i - \frac{e}{c}A_i) - m\,c]\psi(x) = 0. \tag{2.6}$$

Using the property $(\gamma^0)^2 = 1$, the time derivative is written on the left side, while the

rest of the equation passes to the right

$$i\hbar\frac{\partial\psi}{\partial t} = eA_0\psi - \gamma^0\gamma^i(i\hbar c)\partial_i\psi + e\gamma^0\gamma^i A_i\psi + \gamma^0 m\,c^2\psi = \kappa\,\psi \tag{2.7}$$

If the potential A_μ is restored to its original form and the product of matrices is renamed as

$$\gamma^0\gamma^i = \alpha^i = \begin{pmatrix} 0 & \sigma_i \\ \sigma_i & 0 \end{pmatrix}$$

$$\gamma^0 = \beta$$

then κ in eq. (2.7) can be re-expressed as

$$\kappa = c\alpha\cdot(\vec{p} - \frac{e}{c}\vec{A}) + mc^2\beta + e\phi\mathbb{I} \tag{2.8}$$

which is in the original form put forth by Dirac.

We now analyze the **non-relativistic limit** limit of this equation, setting our sight on the Schrödinger equation. For this purpose, the equation (2.7) will be considered, along with a decomposition of the four-component spinor ψ into two components

$$\psi = \begin{pmatrix} \varphi' \\ \chi' \end{pmatrix}$$

We then have

$$i\hbar\frac{\partial}{\partial t}\begin{pmatrix} \varphi' \\ \chi' \end{pmatrix} = \begin{pmatrix} c\vec{\sigma}\cdot\widehat{\Pi}\chi' \\ c\vec{\sigma}\cdot\widehat{\Pi}\varphi' \end{pmatrix} + e\phi\begin{pmatrix} \varphi \\ \chi \end{pmatrix} + m\,c^2\begin{pmatrix} \varphi \\ -\chi \end{pmatrix}$$

where $\vec{\sigma} = (\sigma_x, \sigma_y, \sigma_z)$ and the generalized momentum operator has been introduced $\widehat{\Pi} = \vec{p} - (e/c)\vec{A}$. If we further separate the largest energy scale, namely the rest energy, in the following way

$$\psi = \begin{pmatrix} \varphi' \\ \chi' \end{pmatrix} = e^{-i(mc^2/\hbar)t} \begin{pmatrix} \varphi \\ \chi \end{pmatrix}$$

a new expression for the eq. (2.7) is obtained

$$i\hbar\frac{\partial}{\partial t}\begin{pmatrix} \varphi \\ \chi \end{pmatrix} = \begin{pmatrix} c\vec{\sigma}\cdot\widehat{\Pi}\chi \\ c\vec{\sigma}\cdot\widehat{\Pi}\varphi \end{pmatrix} + e\phi\begin{pmatrix} \varphi \\ \chi \end{pmatrix} - 2mc^2\begin{pmatrix} 0 \\ -\chi \end{pmatrix} \tag{2.9}$$

A "formal" solution for the lower part of the spinor can be written as

$$\chi = \frac{\vec{\sigma}\cdot\widehat{\Pi}}{2mc}\varphi - \frac{i\hbar\frac{\partial}{\partial t} - e\phi}{2mc^2}\chi \tag{2.10}$$

If only the first term were retained, the Pauli equation would result in the magnetic dipole interaction, with the correct value of 2 for the spin g-factor. The second term must be kept for the spin-orbit coupling to appear. In our formulation, we can consistently argue that the first term in eq. (2.10) is the dominating one, as the second one is divided by the rest mass (largest energy scale)

This way, the equation can be solved iteratively in order to get χ as a function of φ

$$\chi = \frac{\vec{\sigma}\cdot\widehat{\Pi}}{2mc}\varphi - \frac{i\hbar\frac{\partial}{\partial t} - e\phi}{2mc^2}\left(\frac{\vec{\sigma}\cdot\widehat{\Pi}}{2mc}\right)\varphi \tag{2.11}$$

This relation is then substituted in the eq. (2.9) for φ and what is left can be identified with the Hamiltonian of the problem. Nevertheless, the wave function must be normalized before this; otherwise the Hamiltonian is not Hermitian. This technical step is excluded here, and we only take care of the two products of operators containing $\vec{\sigma}$ and $\widehat{\Pi}$.

The first of them is

$$\frac{1}{2m}(\vec{\sigma}\cdot\widehat{\Pi})(\vec{\sigma}\cdot\widehat{\Pi}) = \frac{1}{2m}\widehat{\Pi}^2 - \frac{e\hbar}{2mc}\vec{\sigma}\cdot\vec{B}$$

where the kinetic energy is represented by $\widehat{\Pi}^2$ and the correct electron g-factor equal to 2 is immediately recognized, once the following identifications are done

$$\frac{\hbar}{2}\vec{\sigma} = \widehat{S}$$

and for the Bohr magneton

$$\mu_B = \frac{e\hbar}{2mc}$$

The second one, stemming from the corrections included in eq. (2.11), turns out to be

$$\frac{2}{4m^2c}(\vec{\sigma} \cdot \widehat{\Pi})\phi(\vec{\sigma} \cdot \widehat{\Pi}) = \frac{2}{4m^2c}\vec{p}\phi\vec{p} + \frac{2}{4m^2c}\vec{\sigma} \cdot (\nabla\phi \times \vec{p})$$

The $\vec{p}\phi\vec{p}$ term has no classical analogue, and is of order $(v/c)^2$. The second term accounts for the sought spin-orbit coupling. The total result for the Hamiltonian, with the correct normalization of the wave function, gives

$$
\begin{aligned}
H &= \left[\frac{\Pi^2}{2m} - \frac{p^4}{8m^3c}\right] + e\phi - \frac{e\hbar}{mc}\vec{\sigma} \cdot \vec{B} - \frac{ie}{8m^2c^2}\vec{p} \cdot \vec{E} - \\
&\quad \left[\frac{ie}{8m^2c^2}\vec{\sigma} \cdot (\nabla \times \vec{E}) + \frac{e}{4m^2c^2}\vec{\sigma} \cdot (\vec{E} \times \vec{p})\right].
\end{aligned}
\tag{2.12}
$$

The last bracket in the expression contains the total spin-orbit coupling, and leads, for example, to the fine structure of atoms. In this case, the presence of a symmetric spherical potential leads to

$$\vec{\sigma} \cdot (\nabla \times E) = 0$$

and

$$\frac{e}{4m^2c^2}\vec{\sigma} \cdot (\vec{E} \times \vec{p}) = \frac{e}{4m^2c^2}\vec{\sigma} \cdot \frac{\partial V}{\partial r}\left(\frac{\vec{r}}{r} \times \vec{p}\right) = \frac{e}{4m^2c^2}\frac{1}{r}\frac{\partial V}{\partial r}\vec{\sigma} \cdot \vec{L}.$$

This formula shows that the correct Thomas Precession -one half the result obtained for an electron at rest in the magnetic field of a proton circling around it- is obtained as well. Finally, the term $\vec{p} \cdot \vec{E}$, associated to the *Darwin force* is not discussed here as it is beyond the scope of our subject.

In this preliminary section we have introduced the spin degree of freedom and the resulting spin-orbit coupling. The results we have got are valid for a free electron in the presence of a general potential $V(\vec{r})$. Exactly the same spin-orbit coupling exists in solids, where the electron sees a crystalline landscape. However, the effective theories we will work with, allow to stow the information about the hosting crystalline structure and its parameters in the coupling constants, and derive effective spin-orbit Hamiltonians.

The derivation of these effective terms and the associated parameters makes use of the crystalline properties of the underlying structure. For this reason, we continue in the next section by briefly introducing Group theory, an appropriate frame to study symmetries.

2.2 A brief summary on Group Theory

Semiconductors, and metals alike, are generally made of regular arrays of ions. This ordered feature offers the possibility of identifying symmetry operations that leave the crystal unchanged. Indeed, this property is exploited to facilitate the study of solids, and in particular, the electron band structure. For example, if two different states labeled with $\vec{k}$ and $\vec{k}'$ are related to each other via a symmetry operation of the crystal, then the electronic energies of these two different states must be identical. This implies that we need to calculate the energy of one state, and infer the other one by symmetry considerations. The second consequence is related to the wave function: they can be expressed in a symmetrized fashion, meaning that they have certain transformation properties defined by the symmetries of the crystal. Therefore, given a symmetry operation, we can classify and group the wave functions according to it. In doing so, we can

deduce if a matrix element -or equivalently, an operator coupling two states- vanishes or not, depending on the symmetry properties of the operator. These gives the so-called *selection rules*. As we will see below, the symmetry operations must also cope with the spin degree of freedom as well, and so a convenient extension of the symmetry operations reserved for crystal structure without spin will be necessary. Once the importance of regarding and identifying the symmetry operations has been highlighted, a systematic way of sorting them is of great utility. The suitable conceptual framework to handle this is **Group Theory**. Though we do not make a thorough description of this theory here, we discuss some relevant concepts and the widely used terminology in solid state physics.

A group is a set of elements (operations in our case), where the successive application or multiplication between any two elements belongs to the set. If a and b belong to **G**, the multiplication must satisfy five conditions:

- Closure $\Rightarrow$ The result of the operation ab is another element of the group.

- Associativity $\Rightarrow$ It is equivalent $(ab)c = a(bc)$

- Identity $\Rightarrow$ An element e is the identity if $\forall a \in \mathbf{G} \rightarrow ea = a$

- Inverse $\Rightarrow$ Every element of $\mathbf{G}$ has its inverse element a^{-1} such that $a^{-1}a = e$

In principle, the successive application of two operations in the group does not commute. In the case of crystal lattices, although there are many symmetry operations, we can list some basic operations in terms of which any other may be written. The defintion for them is

- C_i is an $i-fold$ rotation about a given axis

- σ is the reflection about a plane

- i is the inversion
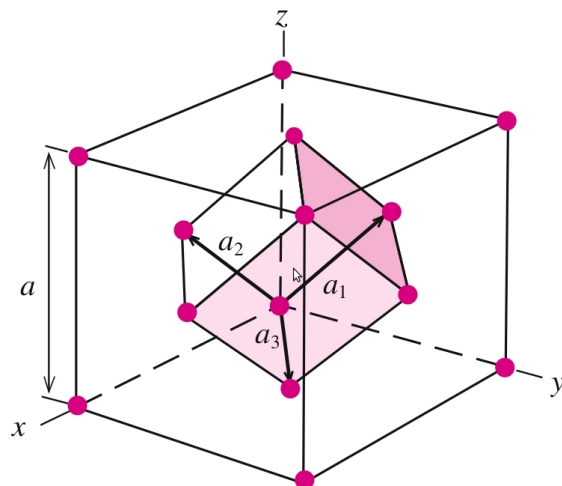
Figure 2.1:   The set of three primitive lattice vectors is shown for the face-centered cubic lattice.

- S_i means the rotation C_i followed by a reflection about the plane perpendicular to the rotation axis

- the identity operation E.

If we now compute all the possible symmetry operations of this kind, but with the additional restriction that at least one point *fixed* and unchanged in space, we obtain the so-called *point* group, related to rotation, inversion and reflection symmetries. Crystals, on the other hand, also have translational symmetries, which also form a group. Groups that contain both rotation and translations are **space** groups. The point group of the zincblende structure is denoted by T_d^2. The translational symmetry operations are defined in terms of the three primitive lattice vectors (see Fig. 2.1.), which are at the same time used to define the point group operations, with the origin at one of two atoms in the primitive cell.

With this choice of coordinates, the 24 operations for T_d^2 are enumerated below (usually introduced equivalently for the methane molecule):

- E : the identity

- C_3: clockwise and counterclockwise rotations of 120° about the $[111], [\bar{1}11], [1\bar{1}1]$, and $[11\bar{1}]$ axes, respectively (8 operations);

- C_2 : rotations of 180° about the $[100], [010]$, and $[001]$ axes, respectively (x3)

- S_4 : clockwise and counterclockwise rotations of 90° about the $[100], [010]$, and $[001]$ axes, respectively, followed by a reflection(x6);

- σ : reflections with respect to the $(110), (1\bar{1}0), (101), (10\bar{1}), (011),$ and $(01\bar{1})$ planes, respectively (x6).

So far we have taken care of the pure description of the crystal in terms of its symmetries. A question might arise: How does an operator generating any of the symmetry transformations cited above act on the wave function? For this, we need a representation of the operator. One way is the matrix representation of an operator in a given basis set $\phi_i(\vec{r})$, spanning the Hilbert space,

$$\mathbf{H}(\vec{r})\phi_i(\vec{r}) = \sum_k H_{ik}\phi_k(\vec{r}), \tag{2.13}$$

where H_{ki} is the matrix element between the states i and k. If we are to consider the effect of any operation $\mathbf{S}$ upon the basis set, we must also operate on the spatial variable $\vec{r}$ [61], such that

$$\phi_i(\mathbf{S}\vec{r}) = \sum_k S_{ik}\phi_k(\vec{r}) \tag{2.14}$$

This leads to an expression for the matrix elements of a Hamiltonian which is transformed under the same $\mathbf{S}$, i.e $H(\mathbf{S}\vec{r})$

$$H_{ij} \rightarrow \sum_{kl} S_{il}^{-1} H_{lk} S_{kj} \tag{2.15}$$

Assuming that $\mathbf{S}$ is any operation of the symmetry group of the Hamiltonian (H remains unchanged under S), we obtain the following condition for the commutator of both operators

$$[\mathbf{H}, \mathbf{S}] = 0$$

This means that a given symmetry of the Hamiltonian, and thus of the crystal, can be expressed via a vanishing commutator of it with the corresponding symmetry operator. Once we fix a basis for each element S of the group, there is a corresponding matrix S_{ik}. The correspondence between the elements of a group and the matrices representing them is such that for $a, b, c \in G$, the multiplication $ab = c$ corresponds to $M_a\, M_b = M_c$, where M_α, the matrix associated with the group element $\alpha = a, b, c$ is termed the *representation* of a group. Such a correspondence is not unique, since the basis can be arbitrary chosen. There is actually -for a given group- an infinite number of such groups of matrices, each of them being connected to its counterpart in another representation via a unitary transformation (they are said to be *equivalent*). Among all of them, there is one special basis set, namely the eigenbasis $\Psi_i(\vec{r})$ which satisfies

$$\mathbf{H}(\vec{r})\Psi_i(\vec{r}) = \epsilon_i \Psi_i(\vec{r}) \tag{2.16}$$

The transformed equation can be consistently expressed as

$$\mathbf{H}(\mathbf{S}\vec{r})\Psi_i(\mathbf{S}\vec{r}) = \epsilon_i \Psi_i(\mathbf{S}\vec{r}) \tag{2.17}$$

and as $\mathbf{S}$ stands for a symmetry operation

$$\mathbf{H}(\mathbf{S}\vec{r}) = \mathbf{H}(\vec{r})$$

$$\mathbf{H}(\vec{r})\Psi_i(\mathbf{S}\vec{r}) = \epsilon_i \Psi_i(\mathbf{S}\vec{r}) \tag{2.18}$$

This result evinces that $\Psi_i(\mathbf{S}\vec{r})$ is itself an eigenfunction with the same energy. In case of having a n-fold degenerate level ϵ_α, with eigenfunctions denoted by Ψ_p^α(r =1,2,3..,n), the implication of the symmetry operation is

$$\Psi_q^\alpha(\mathbf{S}\vec{r}) = \sum_{p=1}^{n} \Psi_p^\alpha(\vec{r}) \tag{2.19}$$

which means that the transformed wave function can be written as a linear combination involving only *partner* wave functions with the same energy

The matrix representation of **S** has block-diagonal form

$$S_{ik} = \begin{pmatrix} S^{(1)} & 0 \\ & \\ 0 & S^{(\alpha)} \end{pmatrix}$$

Every square diagonal submatrix has a dimension $n_\alpha \times n_\alpha$, determined by the degeneracy of the level α. All the other operations in the group can be similarly *reduced* to this shape. A representation is said to be *reducible* if the *same* similarity transformation brings all the matrices of a representation into the same block diagonal form. i.e all of the new matrices have diagonal submatrices with the same dimension at the same position. On the other hand, when each of the blocks cannot be further reduced, the representation is called *irreducible*. A similarity transformation can convert a reducible representation into a block-diagonal form, where each block is a irreducible representation. The possibility of having the irreducible representation of a group -matrices such as $\mathbf{S}^\alpha$ of minimum order n_α- simplifies the multiplication of two matrices of the representation, because it only involves one subspace

$$R^{(\alpha)} = S^{(\alpha)}T^{(\alpha)}$$

The powerful implication that follows is the connection between degeneracy and dimension of irreducible representation. Let us suppose that we have a given representation of a group. If the matrix of any observable, the Hamiltonian for example, is invariant under the group, then it commutes with the irreducible representation of any element

of the group. Shur's lemma then ensures that the eigenvalues of the observable can be put into sets with the same degeneracy n_α. Of course, this does not give the magnitude of the eigenvalues, but since the irreducible representation can be calculated from the basic operations of the group, it provides very useful information about the solution. In other words, the problem of classifying the eigenvalues of the Hamiltonian is solved if the small number of inequivalent irreducible representations of the symmetry group is found. Of course, the eigenfunctions of an operator form a basis for an irreducible representation of the operator, but to find them is the difficult task. In conclusion, we have that for each eigenvalue of a Hamiltonian, there is a unique irreducible representation of the group of that Hamiltonian. Besides this, the degeneracy of an eigenvalue coincides with the dimensionality of this irreducible representation, and thus, the dimensionalities of the irreducible representations of a group are equal to the degeneracies of Hamiltonians (with that symmetry group). Group theory thus provides labels corresponding to irreducible representations and to which eigenfunctions belong. This is a very useful result that group theory gives to quantum mechanics. To illustrate the idea behind the irreducible representations, let us take the example of the reflection of coordinates about the yz-plane, which is represented by the matrix

$$M = \begin{pmatrix} -1 & 0 & 0 \\ 0 & 1 & 0 \\ 0 & 0 & 1 \end{pmatrix} \begin{pmatrix} x \\ y \\ z \end{pmatrix}$$

This is a reducible representation, since the same transformation can be done by applying three one-dimensional matrices in the following way

$$[(-1)x; (1)y; (1)z]$$

and in this last case, the representation cannot be further reduced (it is the irreducible representation). The irreducible representation of a rotation through $180°$ (a 2-fold rotation axis) is also one-dimensional (a sign reversal), provided a suitable choice of coordinates is made. However, the 3-, 4- and 6-fold rotation axes (except the $360°$ rotation) always involve two coordinates changes and the irreducible representation is

therefore two-dimensional. A more physical example concerning the rotation operator is given in [62]. Suppose we have a simultaneous eigenket of $\mathbf{J}$ and $\mathbf{J}_z$, called $|j, m\rangle$. The rotation operator describing a rotation of ϕ around the $\vec{\mathbf{n}}$-axis reads

$$e^{-i\frac{\mathbf{J}\cdot\vec{\mathbf{n}}}{\hbar}\phi}$$

and the matrix elements for this operator in the basis of eigenkets of J^2 and J_z is accordingly

$$\mathfrak{D}^{(j)}_{m,m'} = \langle j, m' | e^{-i\frac{\mathbf{J}\cdot\vec{\mathbf{n}}}{\hbar}\phi} | j, m \rangle \tag{2.20}$$

where the same j is considered on both sides because the rotation operator does not mix states with different j-values, as a direct consequence of the relation

$$[\mathbf{J}^2, J_k] = 0 \quad \forall k.$$

The $(2j+1) \times (2j+1)$ $\mathfrak{D}^{(j)}_{m,m'}$ matrix is said to be a $(2j+1)$-dimensional irreducible representation of the rotation operation $\mathfrak{D}$.

To finish with the classification of the elements of a group, we now fetch the **class** notion. This concept allows us to assemble all the elements of a group into smaller subsets. If two elements s and t in a group satisfy that $xs = tx$ for *some* element x in the group, then s and t are said to be conjugate (they are related by a similarity transformation). A class contains all the elements of a group that are conjugate to each other. To find the class where an element is, one considers the products of the form

$$EsE^{-1}, \; vsv^{-1}$$

for every element v in the group. E is the identity. Several of these products coincide with other elements of the group. By combining and grouping them, we form a class [63]. This transformation also implies that $s = x^{-1}tx$, showing that we can get the same result of the transformation s by means of an application in a certain manner involving two other operations t and x. In the case the group is represented by matrices, the similarity transformation that connects all the elements within a class implies that their traces are all the same. The traces of the matrices in a representation are called its *characters*.

A physical interpretation for this might be as follows: if the symmetry operations that the elements of the group represent satisfy the above relation $B = X^{-1}AX$, it means that the net operation B can be equally obtained by first rotating the object by X, then carrying out the operation A and finally undoing the initial rotation by X^{-1}. Taking for example A as a rotation, then B is also a rotation through a different rotation axis.

For zincblende, for example, we had that the point group has 24 symmetry operations. All these can be further divided in five classes:

$$\{E\}, \{8C_3\}, \{3C_2\}, \{6S_4\}, \{6\sigma\}$$

We have introduced classes because group theory provide us here with a valuable theorem: the number of classes is equal to the number of inequivalent irreducible representations. We thus learn now that T_d (the point group of zincblende) has five irreducible representations.

Let us finally regard the notation used in band structure. At the center of the Brillouin zone, the so-called Γ-point, the wave functions always transform according to the irreducible representation of the point group of the crystal. Therefore, for ZB we label the irreducible representation by Γ_i, where the subscript $i = 1, 2, 3, 4, 5$ simply refers to the irreducible representation in Koster notation. With the introduction of the spin degree of freedom, this notation changes, as the point group itself does (see section 2.6.1).

As we have seen, group theory provides a suitable mathematical tool and terminology to study symmetric structures. We next describe specifically the two crystal structures that concern this thesis, namely zincblende and wurtzite.

2.3 Crystal Structures: Zincblende and Wurtzite

While most of the III-V semiconductors crystallize in the zincblende (ZB) structure, the family of the II-VI and IV-VI compounds exhibit a greater variety [64]; they can be found in the ZB form, others are wurtzite (WZ) and some of them can be found in both forms. InAs, for example, presents a ZB structure in the bulk, but it is of the WZ

type when grown in quasi one-dimensional quantum wires. A further key feature of a band structure in semiconductors is its band gap: it can be either a direct-gap, as in some zincblende and wurtzite-type semiconductors, or an indirect-gap, as in silicon. In a direct-gap semiconductor the maximum of the valence band coincides with the minimum of the conduction band. Since electrons in semiconductors mostly populate the lowest states in the conduction band, it is possible to concentrate on the electronic states near the single conduction band minima. In this thesis, we rely on this condition as we only consider direct-gap cases.

As we have seen, the crystal structure is very important because it determines the symmetry properties of the system, and hence the correct irreducible representation in the band center, which is a key step in the construction of the $k \cdot p$ Hamiltonians, explained in the ensuing section. We also present there the corresponding SOC both in ZB and WZ materials, whose crystalline properties are now described.

Zincblende

The underlying structure of ZB is the diamond lattice, which consist of two interpenetrating face-cented cubic Bravais Lattices, displaced along the diagonal of the cubic cell (see Fig. 2.2) by $\frac{a}{4} = (\hat{x} + \hat{y} + \hat{z})$ [65]. It must be noted that the diamond structure is not a Bravais Lattice. In the diamond structure each lattice point and its 4 nearest neighbors form a regular tetrahedron. The zincblende case is obtained when the two fcc lattices are made of different atoms, for example GaAs, which is a III-V compound. Concerning its symmetry properties, we have already mentioned that its space group is T_d^2 while its point group is T_d, containing 24 basic operations listed before. For ZB materials, the characteristic representations for the band center is sketched in Fig. 2.3 where the effect of the spin-orbit coupling manifest in the split off of the valence band, which are p-like with orbital angular momentum $l = 1$ at the band center. Without spin-orbit, the valence would be three-fold degenerate at the band center. In the presence of SOC, the valence band degeneracy is lifted in two ways. The band with total angular momentum $J = 1/2$, the so-called *split-off band*, separates from the *heavy hole* and *light*
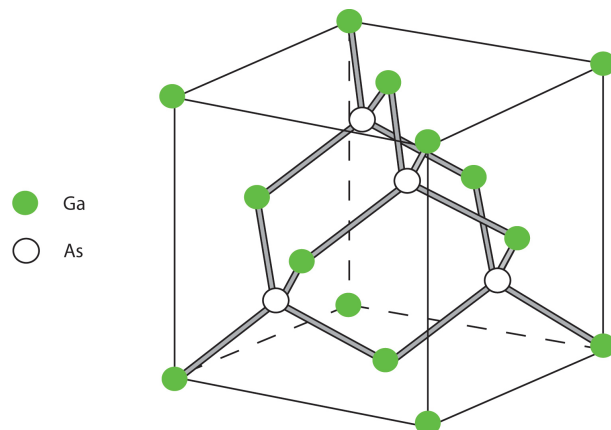
Figure 2.2: The conventional cubic cell for the diamond structure consists of two inter-penetrating face-centered cubic. Each of the sublattices contains a different kind of atoms (Ga and As), making up the zincblende structure.

hole bands (both of them with total angular momentum $J = 3/2$). The combination of the SOC and the lack of inversion symmetry leads to an energy splitting for conduction and valence states with $k \neq 0$, even if the magnetic field is zero. As a consequence, the heavy-hole and light-hole bands have different energies for the same k. The influence of the SOC in the electron energy levels for bulk semiconductors was pointed out by Elliot [66] and Dresselhaus [67] and will be further studied in the coming sections.

Wurtzite

The building block for the wurtzite material is the hexagonal close-packed structure (hcp), obtained as two simple hexagonal Bravais Lattices displaced in the horizontal direction, such that the points of one lattice coincides with the center of the triangles formed by the other one. In the vertical direction, the displacement is along the c-axis and the distance is given by $c/2$ (see Fig. 2.4). The space group of WZ is C_{6v}^4, and the symmetries comprising rotations are the identity, clockwise and counterclockwise rotations of $\pi/3$ about the c-axis, and reflections in vertical planes defined by the c-axis and the reciprocal lattices $(\vec{b}_1, -\vec{b}_2, -\vec{b}_1 + \vec{b}_2)$.
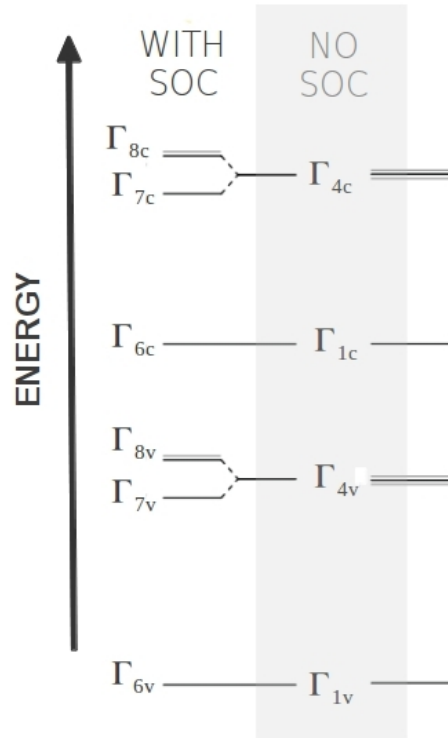
Figure 2.3: The effect of the spin-orbit coupling is shown for the zincblende material. The labels correspond to the group symmetry of the corresponding band, and in the case of SOC, the double group notation is used.

The rotations by π and by $\pm\pi/6$ around the c-axis, and the three reflections in the planes containing the c-axis and $\vec{a}_1, \vec{a}_2$, and $\vec{a}_3$ must be followed by a displacement along $[0, 0, c/2]$ in order to leave the crystal unchanged. The inversion is not a symmetry since different type of atoms occupy the horizontal planes in the z-direction.

In WZ, the spin-orbit coupling has also an effect in the band structure, as it is seen in Fig. 2.5.

The topic of our next section is precisely to introduce the spin-orbit coupling, and describe how they modify the band structure of solids.
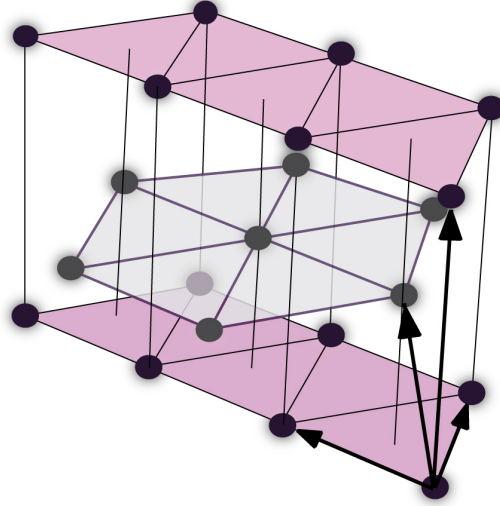
Figure 2.4: The hexagonal close-packed crystal structure is shown. Two interpenetrating simple hexagonal Bravais lattices, displaced along the vertical axis (c-axis), and displaced horizontally so that the center of the triangle of one lies exactly above the point of the other. The three primitive vectors are $\mathbf{a}_1 = a\vec{x}$ $\mathbf{a}_2 = a/2\vec{x} + \sqrt{3}a/2\vec{y}$ (horizontal arrows) and $\mathbf{a}_3 = c\vec{z}$ (vertical arrow).

2.4 Spin-orbit in solids

In this section, we consider the spin-orbit coupling in crystalline solids. In addition to the Zeeman term, already present in the Pauli Equation, we found

$$H_{SOC,vac} = \lambda_{vac}\sigma \cdot (\vec{k} \times \nabla V) \tag{2.21}$$

where $\lambda_{vac} = -\frac{\hbar^2}{4m^2c^2} \approx -3.7 \times 10^{-6} \mathring{A}^2$ and $\hbar\vec{k} = \vec{p}$. The subscript *vac* underlines the fact that we are dealing with an electron in vacuum. This remark will become significant as the effective theory for the SOC is discussed.

In a crystal, the electrostatic potential V can be split off as the sum of a *crystal* contribution V_{crys} that should be separated from V_{other} including any other kind of
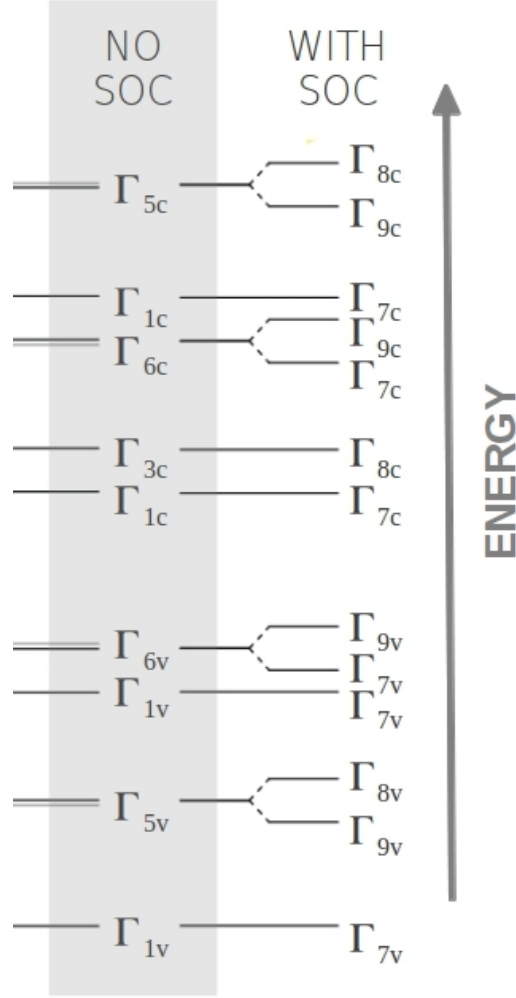
Figure 2.5: The same picture as in Fig. 2.3 is depicted for the wurtzite case.

electric potential due to impurities, boundaries, etc.

$$V = V_{crys} + V_{other} \tag{2.22}$$

The distinction drawn for the possible types of electrostatic potential leads to a classification of the different kinds of SOC. In this sense, we will use the terms *intrinsic* and *extrinsic* spin-orbit coupling, even though it is not unique across the literature. We will refer to the term extrinsic as the spin-orbit contribution that depends on the *impurities*, in accordance with the definition given in Ref. [68]. The **intrinsic** SOC, on the

other hand, means that the spin-orbit field in the solid system is solely related to the structural properties of the system and arises even in the absence of impurities. The *inversion* symmetry needs to be broken to get such a term. Such a definition is based on the idea of intrinsic semiconductors, which are so pure that, at a sufficiently high temperature, the impurity contribution to the carrier density is negligible, and result in intrinsic conductivity. At lower temperatures, the extrinsic properties emerge as the contribution to the carrier density from impurities dominates.

The well-known "Rashba" coupling, for two dimensional systems, arises as consequence of the asymmetry in the confinement potential.

In three dimensional systems, the expression for the intrinsic SOC depends on the crystal structure and band parameters, and as we will see below when we study the Dresselhaus coupling, the zincblende and the wurtzite examples exhibit different H_{int}.

In contrast to this, an **extrinsic** SOC accounts for the coupling of the moving spin in the presence of the electric field due to impurities. Hence, the extrinsic coupling is also present even if the inversion symmetry is preserved. An extrinsic term looks like [68]

$$H_{ext} = \lambda \sigma \cdot (\vec{k} \times \nabla V) \tag{2.23}$$

where λ is an effective constant that contains information about the band structure. The role of V is played, for example, by the impurities potential.

The effective constants and effective SOC terms are obtained by appealing to the so-called $k \cdot p$ method. In combination with the envelope function approximation, it allows to include the effect of the SOC close to the band minima. We start with the envelope function approximation, and then introduce the $k \cdot p$ method. This latter contains the Kane Model in which the effective SOC terms can be calculated. Since the full derivation exceeds the scope of this thesis, it is not carried out in detail. The main ideas and hints will be exposed nevertheless.

2.5 The envelope function approximation

The envelope function approximation (EFA) copes with the behaviour of electrons and holes in the presence of electric or magnetic fields that vary smoothly in the length scale of the crystal. It describes the electron wave function in terms of band-edge Bloch Functions, which renders the method very useful for the subsequent systematic perturbation treatment [69]. To observe how these conditions are introduced, it is instructive to see the derivation of the EFA Hamiltonian, which starts with the Schrödinger Equation

$$\left(\frac{(-i\hbar\nabla + (e/c)\vec{A})^2}{2m_0} + V_0 \quad + \quad \frac{\hbar}{4m_0^2 c^2}\vec{\sigma}\cdot\left((-i\hbar\nabla + (e/c)\vec{A})\times\nabla V_0\right) \right. \tag{2.24}$$
$$\left. + \quad V(r) + \frac{g_0}{2}\mu_B\vec{\sigma}\cdot\vec{B}\right)\Psi(\vec{r}) = E\Psi(\vec{r}).$$

The potential V_0 represents the periodic potential, the vector $\vec{A}$ generates the magnetic field $\vec{B}$, and $V(\vec{r})$ accounts for the slowly varying potential. The next step is to expand the eigenfunctions in terms of band-center Bloch functions, in the same spirit as the $\vec{k}\cdot\vec{p}$ method in next section.

$$\Psi(\vec{r}) = \sum_{\nu'\sigma'} \psi_{\nu'\sigma'}(\vec{r}) u_{\nu'0}(\vec{r})|\sigma'\rangle \tag{2.25}$$

where $u_{\nu'0}$ are the quickly oscillating Bloch Functions of the ν-band at $k = 0$ and $|\sigma'\rangle$ are the spin eigenstates in the S_z basis. The $\psi_{\nu'\sigma'}(r)$ play the role of the expansion coefficients or *envelope functions*, now position-dependent, that modulate the function. We then insert this Ansatz in the eq. (2.25) and integrate over one unit cell. At this stage, we appeal to the smoothly varying character of the field and ψ; we consider that within one unit cell these quantities do not change considerably and therefore, we take them out of the integral. We then come across a set of coupled equations called multiband (many bands are in principle involved) or EFA Hamiltonian:

$$\sum_{\nu',\sigma'} \left\{ \left[E_{\nu'}(0) + \frac{(-i\hbar\nabla + (e/c)\vec{A})^2}{2m_0} + V(\vec{r}) \right] \delta_{\nu,\nu'}\delta_{\sigma,\sigma'} \right. \tag{2.26}$$

$$+ \frac{1}{m_0}(-i\hbar\nabla + (e/c)\vec{A}) \cdot \vec{P}_{\nu,\nu'}^{\sigma\sigma'} + \triangle_{\nu,\nu'}^{\sigma\sigma'}$$

$$\left. \left[+ \frac{g_0}{2}\sigma \cdot \vec{B}\delta_{\nu,\nu'} \right] \right\} \Psi_{\nu',\sigma'}(\vec{r}) = E\Psi_{\nu,\sigma}(\vec{r})$$

where

$$\vec{P}_{\nu,\nu'}^{\sigma\sigma'} = \langle\nu\sigma|\vec{\Pi}|\nu'\sigma'\rangle$$

with

$$\vec{\Pi} = \mathbf{p} + \frac{\hbar}{4m_0c^2}\vec{\sigma} \times \nabla V_0$$

and

$$\triangle_{\nu,\nu'}^{\sigma\sigma'} = \frac{\hbar}{2m_0^2c^2}\langle\nu\sigma|\left[\vec{p}\cdot\vec{\sigma}\times(\nabla V_0)\right]|\nu'\sigma'\rangle.$$

We notice that the characteristic feature in the EFA set of equations is the presence the envelope functions instead of Bloch-Functions. Using quasi-degenerate perturbation theory we can convert this infinite-dimensional eigenvalue equation into a solvable problem.

We have done here a simple exercise of deriving a Hamiltonian that contains a slowly varying potential whereby we expected to get envelope functions. We now step back to consider a situation without this smooth potential. We wish instead to describe the energy dispersion $E(\vec{k})$ close to some point $\vec{k} = \vec{k}_0$ in the band structure. For this, we will resort to a method, called the $k \cdot p$ method, that in analogy to the EFA, considers a linear combination of many bands to build up a solution.

In the end, we will see that the EFA Hamiltonian can be derived from the $k \cdot p$ method by some proper substitutions.

2.6 $k \cdot p$ method

A simple tight-binding (TB) model would be enough to understand how the discrete levels of the atoms merge and form a band when they come closer. Such a quasi-continuous energy levels arise as a consequence of the atomic wave-function overlapping of different atoms. Depending on the type of orbital, the bands may have positive or negative curvatures. The cosine-like energy dispersion given by the TB method resembles the real band structure for k values close to the band extrema. In this region, one can often make a parabolic approximation for the energy dispersion and attribute an effective mass to the electron. The effective mass then allows to pack information about the physical system in a parameter, and to have a simpler Hamiltonian (as simple as the free-electron Hamiltonian, for example), yet restricted to a given energy region.

In this section we will explain how the concept of effective mass arises in more sophisticate descriptions of band structures. The $k \cdot p$ method used to introduce it has proved to be successful for the calculation of energy dispersion near a given $\vec{k}_0$, which for us will be the Γ point or zone center [70].

First of all, we cite the Bloch Theorem, which states that the solutions to the Hamiltonian containing a periodic potential V_0

$$\left(\frac{p^2}{2m_0} + V_0 \right) \Psi_{n\vec{k}} = E_{n\vec{k}} \Psi_{n\vec{k}} \tag{2.27}$$

can be written

$$\Psi_{n\vec{k}}(\vec{r}) = e^{i\vec{k}\cdot\vec{r}} \cdot u_{n\vec{k}}(\vec{r}) \tag{2.28}$$

where $u_{n\vec{k}}(\vec{r})$ is a periodic function with the periodicity of the lattice and m is the free-electron mass, and $\vec{k}$ -the wave vector- is associated to the crystal momentum of the electron. If we now replace this function into eq. (2.27), an equation for the periodic part of the Bloch Function (BF), known as the $\vec{k} \cdot \vec{p}$ equation, is obtained

$$\left(\frac{p^2}{2m_0} + V_0 + \hbar \frac{\vec{k} \cdot \vec{p}}{m_0} + \frac{\hbar^2 k^2}{2m_0} \right) u_{n\vec{k}} = E_{n\vec{k}} u_{n\vec{k}} \tag{2.29}$$

At $\vec{k} = 0$, this equation reduces to

$$\left(\frac{p^2}{2m_0} + V_0 \right) u_{n\mathbf{0}} = E_{n\mathbf{0}} u_{n\mathbf{0}} \quad (\text{ with n=0,1,2,3...}) \tag{2.30}$$

Now we assume we know the solution to this equation. It can be shown that the periodic functions $u_{n\mathbf{0}}$ with different n's form a complete set of basis, and so we can exploit this property to expand the $u_{n\mathbf{k}}$ in terms of these band-edges states and treat the $\hbar\mathbf{k} \cdot \mathbf{p}/m$ as a perturbation. The general expression for the proposed solution is

$$u_{n\vec{k}} = \sum_{n'} c_{n'}^{n}(\vec{k}) u_{n'\mathbf{0}}. \tag{2.31}$$

For simplicity we consider the band structure to have a minimum at $E_{n\mathbf{0}} = 0$ and no degeneracy exist at this point.

At this point, we can proceed by using standard perturbation theory, and take the $k \cdot p$ operator as the "weak" term. In this case, we obtain the correction terms to $u_{n\mathbf{0}}$ (the "unperturbed state")

$$\tilde{u}_{n\vec{k}} = u_{n\mathbf{0}} + \frac{\hbar}{m_0} \sum_{n' \neq n} \frac{\langle u_{n\mathbf{0}} | \vec{k} \cdot \vec{p} | u_{n'\mathbf{0}} \rangle}{E_{n\mathbf{0}} - E_{n'\mathbf{0}}} u_{n'\mathbf{0}} \tag{2.32}$$

and for $E_{n\mathbf{0}}$

$$\tilde{E}_{n\vec{k}} = E_{n\mathbf{0}} + \frac{\hbar^2 k^2}{2m_0} + \frac{\hbar^2}{m_0^2} \sum_{n' \neq n} \frac{|\langle u_{n\mathbf{0}} | \vec{k} \cdot \vec{p} | u_{n'\mathbf{0}} \rangle|^2}{E_{n\mathbf{0}} - E_{n'\mathbf{0}}}. \tag{2.33}$$

We note that there is no linear dependence on k, because the energy has been chosen to be an extreme. The following parabolic energy dispersion for small values of k

$$\tilde{E}_{n\vec{k}} = E_{n\mathbf{0}} + \frac{\hbar^2 k^2}{2m^*} \tag{2.34}$$

defines the **effective mass** of the band as

$$\frac{1}{m^*} = \frac{1}{m_0} + \frac{2}{k^2 m_0^2} \sum_{n' \neq n} \frac{|\langle u_{n\mathbf{0}} | \vec{k} \cdot \vec{p} | u_{n'\mathbf{0}} \rangle|^2}{E_{n\mathbf{0}} - E_{n'\mathbf{0}}} \tag{2.35}$$

by likening the corresponding terms. This formula shows explicitly the correction to the free-electron mass due to the $\vec{k} \cdot \vec{p}$ coupling between this band and the neighboring ones, and it is valid as long as the energy region of interest is close to $E_{n\mathbf{0}}$. We note that the wave function $u_{n\mathbf{0}}$ couples to another $u_{n'\mathbf{0}}$ via the $\mathbf{p}$ operator. The importance of group theory becomes evident here. The operator $\vec{p}$, responsible for the coupling between the two states, has a Γ_4 symmetry in the ZB case (it transforms like a vector). Therefore, applying the **matrix element theorem** and **group theory**, we can anticipate that a conduction band state with symmetry Γ_{1c} will be coupled only to valence band state $\sim \Gamma_{4v}$ (and in principle, also to a Γ_{4c}). The Γ_{4v} state, besides being coupled to Γ_1, also interacts with Γ_3, Γ_4, and Γ_5 states. This is just an example exhibiting how group theory provides a way to discard certain matrix elements based on symmetry properties. Secondly, it must be also noticed that the energy separation between the two states weights the relative contribution of n' to the effective mass of the band n, and could eventually give rise to a negative or a positive contribution to m^*. These two general features can be applied to several direct band gaps of the group-III-V and II-VI. To illustrate the idea we take zincblende GaAs and calculate the effective mass of a **conduction electron**. In Fig. 2.3, the zone-centers states for this material [71] are shown using the group notation for the identification of the symmetry properties of the states involved. We also know that

$$\Gamma_1 \sim S$$

and

$$\Gamma_4 \sim X, Y, Z.$$

The names S and (X, Y, Z) are used because of the similarity between the Γ_4 and Γ_1 states and the atomic p states (three fold degenerate with $l = 1$) and s states, respectively. The other important point is that

$$\langle S|p_x|X\rangle = \langle S|p_y|Y\rangle = \langle S|p_z|Z\rangle$$

and that there is no term like $\langle S|p_x|Y\rangle$. This implies that the effective mass (which should be defined ultimately as a tensor) is isotropic in this case and so

$$\frac{1}{m^*} = \frac{1}{m_0} + \frac{2}{m_0^2}\frac{|\langle S|p_x|X_v\rangle|^2}{E_{\Gamma_{1c}} - E_{\Gamma_{4v}}} - \frac{2}{m_0^2}\frac{|\langle S|p_x|X_c\rangle|^2}{E_{\Gamma_{4c}} - E_{\Gamma_{1c}}} \qquad (2.36)$$

where we include the interaction between the lowest conduction band Γ_{1c} and both the upper conduction band Γ_{4c} and the valence bands Γ_{4v}. In ZB, the last term happens to be smaller that the preceding correction term, and so $m^* < m_0$. Using the same method, we can correct only one of the three p-like valence bands; only the *light hole* band couples to the conduction band Γ_{1c} along a given direction (the $\triangle$ direction). The result here is that $m_{lh} < 0$, which means that the correction "bends" this valence band downwards. The $k \cdot p$ interaction is then capable of changing the curvature of the conduction and valence in certain cases. Within this simple one-band model, the heavy-hole band can also be derived, but in this case, unlike the light-hole band, the interaction of the valence band and the more remote Γ_{4c} state must be necessarily considered.

The general $k \cdot p$ method framework -beyond perturbation theory- allows to describe the coupling between heavy holes and light holes, and other interactions such as non-parabolicity or spin splitting in the band structure. Let us now derive the $k \cdot p$ Hamiltonian with SOC. We must thus include

$$H_{SOC} = -\frac{\hbar}{4m_0c^2}\sigma \cdot \mathbf{p} \times \nabla V_0$$

in eq. (2.29). The resulting equation for the periodic Bloch equation $|n\vec{k}\rangle$ is

$$\left(\frac{p^2}{2m_0} + V_0 + \frac{\hbar^2 k^2}{2m_0} + \frac{\hbar}{m_0}\vec{k} \cdot \vec{\Pi} - \frac{\hbar}{4m_0c^2}\sigma \cdot \mathbf{p} \times \nabla V_0\right)|n\vec{k}\rangle = E_{n\vec{k}}|n\vec{k}\rangle \qquad (2.37)$$

with

$$\vec{\Pi} = \mathbf{p} + \frac{\hbar}{4mc^2}\sigma \times \nabla V_0.$$

It must be noted that owing to the SOC, the newly defined functions $|n\vec{k}\rangle$ are two-component spinor, and the label "n" is a common label both for the orbital motion and for the spin degree of freedom. The indices arise from the irreducible representations of the double group of the band.

However, we will expand the Bloch Functions as before in terms of band-center states, which also are spin eigenstates:

$$|n\vec{k}\rangle = \sum_{\nu',\sigma'=\uparrow,\downarrow} c_{n\nu',\sigma'}(\vec{k})|\nu'\sigma'\rangle \tag{2.38}$$

with $|\nu'\sigma'\rangle = |\nu', \vec{k} = 0\rangle \otimes |\sigma'\rangle$. The next step is to replace this expansion in (2.37) and multiply from the left by $\langle \nu\sigma|$, and in virtue of the orthogonality of the band-center functions, the resulting equation is

$$\sum_{\nu',\sigma'} \left\{ \left[E_{\nu'}(0) + \frac{\hbar^2 k^2}{2m_0} \right] \delta_{\nu\nu'} \delta_{\sigma\sigma'} + \frac{\hbar}{m_0} \vec{k} \cdot \vec{P}_{\nu\nu'}^{\sigma\sigma'} + \triangle_{\nu\nu'}^{\sigma\sigma'} \right\} c_{n\nu',\sigma'}(\vec{k}) = E_n(\vec{k}) c_{n\nu',\sigma'}(\vec{k}) \tag{2.39}$$

where the eigenvalue $E_\nu(0)$ of $|\nu'\sigma'\rangle$ has been introduced.

As the matrix elements appearing in this case $\vec{P}_{\nu\nu'}^{\sigma\sigma'}$ and $\triangle_{\nu\nu'}^{\sigma\sigma'}$ are the same as those in the EFA Hamiltonian (2.27), it seems natural that the EFA Hamiltonian can be obtained from the $k \cdot p$ Hamiltonian by replacing the *vector* $\hbar\vec{k} = \vec{p} \to -i\hbar\nabla + \frac{e}{c}\vec{A}$, adding the slowly varying potential $V(\vec{r})$ and the Zeeman term $(g_0/2)\mu_B \sigma \cdot \vec{B}$. It is worth pointing out that in the EFA case, $\vec{k}$ (or $\mathbf{p}$) is the *operator* of kinetic momentum and must be distinguished from the canonical momentum "$-i\hbar\nabla$". In particular, if no magnetic field is present, then they coincide. If also $V(\vec{r})$ is zero, then the wave vector k is equivalent to the operator k from EFA.

If a non-zero magnetic field is considered instead, then no matter what Gauge is chosen, the components of the operator k do not commute and

$$\vec{k} \times \vec{k} \sim \vec{B}$$

Likewise, we find that

$$[\vec{k}, V(\vec{r})] = -i\nabla V(\vec{r}).$$

Let us see in what follows how the $k \cdot p$ method works for the energy dispersion calculation close to the band center.

2.6.1 The Kane Model : First-order

In the previous section we have found the energy dispersion by means of perturbation theory. Nevertheless, the expansion of the periodic Bloch Function (2.31) can be applied to replace the differential equation (2.29) by the corresponding matrix, in which case an infinite representation naturally appears. As we can only handle finite matrices, an approximation must be done. This consists of the diagonalization within an appropriate subspace, where the interaction between some bands is exactly treated, whereas the coupling to the more distant bands is incorporated through a perturbation scheme. These various models, referred as Kane models, build a hierarchy depending on how and which bands are taken into account. For example, the simplest 4×4 Kane model contains the interaction between the conduction band $\Gamma_{1c} \sim S$ and the three-fold degenerate valence band $\Gamma_{4v} \sim X, Y, Z$. The resulting Hamiltonian [72], in the basis $\{S, -iX, -iY, -iZ\}$, is

$$
H(\vec{k}) = \begin{pmatrix} \epsilon(\vec{k}) + E_g & k_x P & k_y P & k_z P \\ & \epsilon(\vec{k}) & 0 & 0 \\ \dagger & & \epsilon(\vec{k}) & 0 \\ & & & \epsilon(\vec{k}) \end{pmatrix} \tag{2.40}
$$

where $\epsilon(\vec{k}) = \frac{\hbar^2 k^2}{2m_0}$ is the free-electron energy dispersion and $P = -i\hbar m_0 \langle S | P_x | X \rangle$ is related to the coupling between different bands. The energy dispersion is

$$
E(\vec{k}) = \begin{cases} \frac{\hbar^2 k^2}{2m_0} & \text{twice heavy-hole} \\ \epsilon(\vec{k}) + \frac{E_g}{2} + \sqrt{\frac{E_g}{2} + k_x^2 P^2} & \text{electrons} \\ \epsilon(\vec{k}) + \frac{E_g}{2} - \sqrt{\frac{E_g}{2} + k_x^2 P^2} & \text{light-hole} \end{cases}
$$

We see that 2 valence bands are not modified respect to the free-electron one, while the conduction band and the light-hole band lh change and acquire a certain curvature.

The effective masses within this model are isotropic, but the heavy-hole band hh is the free-electron one. The lh band then presents non-parabolicity.

The effective-masses for electrons and holes are

$$\frac{1}{m^*} = \frac{1}{m_0}\left(1 \pm \frac{E_p}{E_g}\right)$$

respectively. The Kane parameter $E_p = \frac{2m_0 P^2}{\hbar^2}$ has been defined.

So far we have neglected the spin-orbit coupling. In the $k \cdot p$ equation (the equation for the periodic Bloch function), the interaction enters as

$$H_{SOC} = \frac{\hbar}{4m_0^2 c^2}\left(\sigma \times \nabla V\right)\cdot \vec{p} + \frac{1}{4m_0^2 c^2}\left(\sigma \times \nabla V\right)\cdot \vec{k} \tag{2.41}$$

if the spin-orbit coupling is applied to the total function $u_{n,\vec{k}}e^{i\vec{k}\cdot\vec{r}}$. The second term in eq. (2.41), being smaller than the first one, is often neglected. The inclusion of spin transforms the 4×4 case into the 8-band Kane model. The spin-orbit coupling lifts the three-fold degeneration present so far in the valence band at the Γ point, leaving only a two-fold degeneration and shifting the energy of the third valence bands to lower energies. This spin split-off band is then considered, and therefore an extra parameter $\triangle_0$ appears. It denotes the energy difference between these two valence bands.

As we have anticipated, the introduction of the spin also entails a modification in the symmetry group of the crystal. The necessity for such a modification can be easily justified if one considers that a orbital part of a wave function remains the same under a rotation of 2π, whereas the spin wave function changes sign under the same operation. Following the notation of Ref. [70], we call $\widehat{E}$ the 2π rotation about a given axis. For a spinless particle $\widehat{E}$ is the identity operation; for a spin-1/2 particle it represents an additional symmetry operation. This implies that if **G** is the point group without spin of a crystal, the new group including spin must be $\widehat{E}$**G**, and it is twice as large as the original one. The name for this kind of groups is accordingly *double* group.

Since the H_{SOC} operates on spin states, we also have to analyze the symmetry proper-ties of the spin matrices, and then review the representations of the symmetry operators. We expect the number of irreducible representations of the double group to increase as

well, as the group is "bigger". The number of elements of the point group in ZB is, as we know, 24 and it is 48 for the double group. However, while the number of **classes** of the single point group is 5, for the double group it is 8, *not* 10. Therefore, Γ_i will run over 1, ..., 8.

In our ZB example, elements in $\{3C_i\}$ and elements in $\{3\widehat{E}C_i\}$ belong to the same class, like $\{6\sigma\}$ and $\{6\widehat{E}\sigma\}$. This explains why the number of irreducible representations is larger but not doubled. The spin-orbit coupling also forces us to adopt other basis functions. The eigenstates of H_{SOC} are also eigenstates of the total angular momentum $\mathbf{J} = \mathbf{L} + \mathbf{S}$ and its z-component. The appropriate basis is now

$$|J, j_z\rangle = \{|\frac{3}{2}, \pm\frac{1}{2}\rangle, |\frac{3}{2}, \pm\frac{3}{2}\rangle, |\frac{1}{2}, \pm\frac{1}{2}\rangle\}$$

We have just seen how the SOC splits the $j = 3/2$ states from the $j = 1/2$ states. Concerning the notation, the four-fold degenerate $j = 3/2$ states belong to a Γ_8 representation, since this is the only four-dimensional representation in the point group. In the case of $j = 1/2$, the irreducible representation may be in principle either Γ_6 or Γ_7, both of them being two-dimensional, but it can be shown that it actually belongs to Γ_7. This observation completes the understanding of Fig. 2.3.

Back in the 8-band Kane model, the bands considered are the Γ_{6c}, Γ_{8v} and Γ_{7v}, these two last bands separated by $\triangle_0$. The basis is the following

$$\{|iS \uparrow\rangle, |\frac{3}{2}, \pm\frac{1}{2}\rangle, |\frac{3}{2}, \pm\frac{3}{2}\rangle, |\frac{1}{2}, \pm\frac{1}{2}\rangle, |iS \downarrow\rangle, \}$$

and matrix elements such as

$$\langle i|S \uparrow |H|\frac{3}{2}\frac{3}{2}\rangle = \langle i|S \uparrow |H|\frac{1}{\sqrt{2}}(X + iY) \uparrow\rangle = \frac{1}{\sqrt{2}}P(k_x + ik_y)$$

must be calculated. Solving for the energy dispersion, the effective masses are derived. The result shows that for the electron

$$\frac{1}{m_e} = \frac{1}{m_0}\left(1 + \frac{2}{3}\frac{E_p}{E_g} + \frac{1}{3}\frac{E_p}{E_g + \triangle_0}\right) \tag{2.42}$$

Likewise, for the light hole,

$$\frac{1}{m_{lh}} = \frac{1}{m_0}\left(1 - \frac{2}{3}\frac{E_p}{E_g}\right),$$

(2.43)

the heavy hole,

$$\frac{1}{m_{hh}} = \frac{1}{m_0}$$

(2.44)

and the spin hole or split-off band,

$$\frac{1}{m_{sh}} = \frac{1}{m_0}\left(1 - \frac{E_p}{3(E_g + \triangle_0)}\right)$$

(2.45)

While the heavy-hole band still has the free-electron mass (because the remote conduction band is not included), we see that the introduction of the spin modifies the effective mass of the split-off band.

2.6.2 The Kane Model : Second-order

As we previously mentioned, the first-order Kane model deals with states within the desired subspace, and contains k-linear coupling terms between the s and the p states. The inclusion of remote bands (Γ_{4c} for example) leads to quadratic terms (second order) both in the diagonal and the off-diagonal matrix elements. An example of extended Kane model takes up the Γ_{4v} valence bands (6-fold degenerate with spin), the Γ_{1c} (2-fold), and the Γ_{4c} (6-fold). In double group notation, the bands considered are listed in Fig. 2.6 in increasing order of energy, and with the dimension of the irreducible representation besides.

This extended Kane model forms a $14{\times}14$ model that takes *exactly* into account all the $\vec{k}{\cdot}\vec{p}$ and spin-orbit interaction between the above-mentioned bands. The interaction with other bands is considered using second order perturbation theory [69], or alternatively, by means of a block-diagonalization, known as the Lödwin Partitioning, which is actually a unitary transformation that converts the original Hamiltonian into a block-diagonal matrix (keeping terms up to the desired order).

We now describe the Dresselhaus SOC term, for which a 14×14 Kane Model must be considered. An 8 model is not enough.

Figure 2.6: The energy separation at the Γ point is shown with the coupling parameters of the 14×14 Kane model.

2.6.3 Dresselhaus SOC

The time-reversal symmetry, preserved in the presence of the SOC, changes the sign of the vector $\vec{k}$ and "flips" the spin such that its effect is

$$\text{Time-reversal} \rightarrow E_+(\vec{k}) = E_-(-\vec{k}) \tag{2.46}$$

The symmetry provided by an inversion symmetric systems ensures that the energy is unchanged if $\vec{k} \rightarrow -\vec{k}$, whereas the spin remains the same

$$\text{Inversion symmetry} \rightarrow E_\pm(\vec{k}) = E_\pm(-\vec{k}) \tag{2.47}$$

The combination of both properties result in a spin-degeneracy $E_+(\vec{k}) = E_-(\vec{k})$, which is lifted upon the inclusion of an inversion symmetry breaking mechanism. This is indeed the case that we will next consider: systems without a center of inversion or equivalently, with bulk inversion asymmetry (BIA). In zincblende or wurtzite material, the inversion

symmetry is broken due to the different type of atoms in the cell, and we expect therefore an energy splitting for a given k. Nevertheless, we still have Kramers degeneracy as we firstly mentioned. The wave vector $\vec{k}$ defines a spin orientation axis $\mathbf{n}(\vec{k})$ that depends on $\vec{k}$, and we have an eigenstate of the spin operator pointing along this direction. The time-reversed partner carrying the same energy, points in the direction defined by $-\vec{k}$. All these symmetries imply that in these materials without bulk inversion symmetry, only odd powers of k are generally allowed in the energy expansion around the symmetry point Γ. This effect is know as the Dresselhaus or Bulk Inversion Asymmetry (BIA) effect. In ZB, the lowest term is cubic, unlike the WZ case having a linear-in-k term. One way of approaching the problem is the **Theory of invariants**.

Although this theory has not been detailed here, it basically states that since the Hamiltonian of a system must be invariant under the same symmetry operations of the crystal involved (the T_d for the zincblende), the only possible effective Hamiltonian terms containing k and σ must be compatible with this symmetry. In this way, one can rule out other terms that must necessarily vanish.

Zincblende structures

For example, if we focus on the higher order term in the conduction band Γ_{6c} of a zincblende material, we know that there is no linear-in-k spin splitting, because the term $\sigma \cdot (\vec{k} \times \nabla V)$ in first order perturbation and the term $\sigma \cdot (\vec{p} \times \nabla V)$ coupled via $\vec{k} \cdot \vec{p}$ in second-order perturbation theory gives zero matrix elements [72]. This means that the spin splitting is cubic in k, and so the theory of invariants gives a general expression of this term in zincblende structures, that is known as the "Dresselhaus" term.

$$H^{6c,6c} = \gamma_c \left(k_x(k_y^2 - k_z^2)\sigma_x + c.p. \right) \tag{2.48}$$

where c.p. means cyclic permutations. This is the lowest-order term producing a spin-splitting in the conduction band. The method gives equivalently invariant terms for the valence band that will be omitted here. In the language of Kane models, we get the Dresselhaus term from an extended Kane model, considering the $\Gamma_{7v}, \Gamma_{8v}, \Gamma_{6c}, \Gamma_{7c}$, and

Γ_{8c}, i.e. a 14×14 model.

The figure 2.6 shows these bands and the parameters for the BIA splitting. The prefactor involves the product $PP'Q$, which means that the origin of the *spin-splitting* resides in the $\vec{k} \cdot \vec{p}$ interaction between :

- the valence band states and the Γ_{6c} state (matrix element P)

- the Γ_{6c} and the Γ_{7c} or Γ_{8c} (P')

- the valence band states and the Γ_{7c} or Γ_{8c} (Q)

The spin-orbit split-off energies $\triangle_0$ and $\triangle_0'$ also appear in the formula, as we see in the total expression (the leading order) for this coefficient

$$\gamma_c = P\,P'\,Q \left[\frac{1}{(E_g + \triangle_0)(E_g - E_g' - \triangle_0')} - \frac{1}{E_g(E_g - E_g')} \right] \tag{2.49}$$

For electrons confined to two dimensions, the bulk Hamiltonian cited in eq. (2.48) leads to two contributions. In this case we must take the expectation value of the Hamiltonian. To see how it works, we assume that the confinement direction is along the [001]. In this case, we can separate our solution to the Schrödinger equation in two parts. One of them contains the variables on the plane, while the other one depends on z. Due to the confinement, the energies associated to this latter part are well separated. Usually, only the lowest energy is taken, and an average over the corresponding state is performed. For our averaged BIA Hamiltonian, we must look at the expectation values $\langle k_z \rangle$ and $\langle k_z^2 \rangle$. Whereas $\langle k_z \rangle = 0$, the other value $k_z^2 \sim (\pi/d)^2$ [68], d being the small confinement width. As a consequence, one obtains a linear Dresselhaus term for 2D systems,

$$H_{D,2d}^{(1)} = \beta(k_x \sigma_x - k_y \sigma_y)$$

with $\beta = -\gamma_c (\pi/d)^2$ and a remaining cubic term given by

$$H_{D,2d}^{(3)} = \gamma_c k_x k_y (k_y \sigma_x - k_x \sigma_y)$$

The same average procedure will be applied in this thesis in our approach to quantum dots in nanowires, when the SOC is included in 2D-WZ systems.

Next we consider the spin-orbit coupling terms corresponding to the bulk wurtzite-type case.

Wurtzite structures

Let us briefly discuss the linear spin splitting that occurs in wurtzite materials. The focus is on the conduction band, even though it is also present in the valence band. The Theory of Invariants indicates that the only possible term linear in $\vec{k}$ is [55]

$$H \sim (k_x \sigma_y - k_y \sigma_x) \tag{2.50}$$

Note that there is no linear-in-k_z spin-splitting, if z is along the c-axis. It can be shown that the k-dependent SOC ($\sim (\nabla V_{crys} \times \vec{k}) \cdot \vec{\sigma}$) contribution is zero up to first-order perturbation for the conduction band, in contrast to the valence band where it yields a contribution. The leading term will then result from the second-order coupling between the electron state and the valence band states with Γ_9, Γ_7, and $\Gamma_{7'}$ symmetries. Nevertheless, due to its symmetry, the state associated to Γ_9 does not contribute anyway. In addition to this linear term, the C_{6v} double point group corresponding to the WZ symmetry also allows a cubic-in-k spin-splitting [73], given by

$$H \sim (b\, k_z^2 - k_\parallel^2)(k_x \sigma_y - k_y \sigma_x) \tag{2.51}$$

2.6.4 Rashba SOC

Another source of spin-splitting in semiconductor quantum structures is given by an inversion asymmetry in the *structure* (SIA) due to the confining potential $V(\vec{r})$, for example at a heterostructure. The potential producing the symmetry breaking may be a built-in potential, an external potential, etc, but also some experiments have shown that it is possible to tune the SIA spin-splitting by means of external gates [74, 75].

The lowest order in k and $V(\vec{r})$ in the conduction band Γ_c^6 is given by the Rashba [69]

$$H_{6c,6c}^R = r^{6c,6c}\overline{\sigma} \cdot (\vec{k} \times \vec{E}) \tag{2.52}$$

where $\vec{E}$ denotes the electric field caused to the asymmetry of $V(\vec{r})$. The constant $r^{6c,6c}$ is a material-specific parameter, that vanishes if the bulk split-off energies $\triangle_0$ and $\triangle_0'$ are zero. It is worth pointing out that the calculation of the Rashba coefficient can be made by using the subband $k \cdot p$ method in a 8×8 Kane Hamiltonian, in contrast to the Dresselhaus coupling, that needs a 14×14 model. Further details about the widely studied Rashba model can be found in [68] and references therein. The Theory of Invariants indicates that this is the only term that is linear both in k and the electric field $\vec{E}$ compatible with the symmetries of the conduction band. Assuming that the electric field $\vec{E} = (0, 0, E_z)$, the Rashba energy dispersion results

$$E_{\pm}(\vec{k}_{\parallel}) = \frac{\hbar^2}{2m^*}k_{\parallel}^2 \ \pm \ \langle r^{6c,6c}\,E_z\rangle k_{\parallel} \tag{2.53}$$

where $\vec{k}_{\parallel} = (k_x, k_y)$. The magnitude $\langle r^{6c,6c}\,E_z\rangle$ means an average over the confining dimension, and is usually denoted with α. It is interesting to note that, unlike the BIA case, the SIA spin-splitting depends both on the microscopic details of the underlying crystal (through $r^{6c,6c}$) and the macroscopic field given by E_z. We thus obtain a linear energy dispersion (that depends on the modulus of $\vec{k}_{\parallel}$), such that for each state labeled by (k_x, k_y) a spin orientation is determined, as shown in Fig. 2.7

Although the Rashba is derived for the case of a Structural Inversion Asymmetry, we could equally argue that the SOC induced by the electric field of an impurity (the extrinsic term) causes an asymmetry in the structure, and could be therefore also be dubbed "extrinsic". Furthermore, due to this equivalence it is not surprising that both the Rashba term and the extrinsic term look alike, as we will see in a subsequent section.

The Rashba term is widely used to take into account the structural asymmetry in quasi-2D problems. But an important remark is here noteworthy. This term must not be mistaken with the linear-in-k BIA spin-splitting already mentioned in eq. (2.50). There, the WZ symmetry allows such a linear term for the bulk inversion asymmetry, whereas for the ZB symmetry the lowest term is cubic.
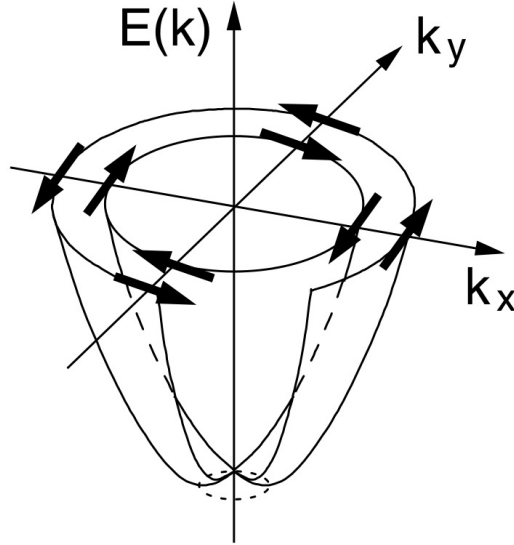
Figure 2.7: Energy dispersion of a state with Rashba splitting (bottom part) together with the spin orientations of electrons(arrows in the upper part).

In our approach to WZ quantum dots, which includes the computation of the energy dispersion of a quasi-2D system, we do not consider the Rashba term explicitly. Nevertheless, as our formulation includes the linear Dresselhaus term, Rashba is therein implicit. What it would merely change is the value of the coupling strength parameter, which for us will be given only by band structure calculations found in Ref. [57].

2.7 Impurities

Impurities or defects, despite the negative nuance in their names, can be useful in semiconductors, because they change the electronic properties in such systems. Depending on what kind of effect is desired, some defects (or impurities) prove to be appropriate and others do not. Obviously, the experimental control over these defects is a major task, and it also determines whether they can be used in a device or not.

At the theoretical level, the study of the electronic properties of defects is required. Although there is a full classification of impurities, we will mention only those corre-

sponding to our study. The GaAs semiconductor we consider here is doped with Silicon impurities. An impurity like Silicon, being different from the atoms in the host crystal (Gallium and Arsenide) is an *extrinsic* defect. Since Silicon appears isolated in the underlying crystal, it receives the name of *point defect*. Additionally, since it tends to substitute the Ga it gives an electron to the crystal, hence the name *donor*, in contrast to acceptor impurities. Conversely, Silicon may be an acceptor in another type of crystal or semiconductor. In GaAs, a Silicon atom substitutes a Ga atom of the host crystal, and in this situation, the defect is said to be *substitutional*. Compared to the Ga atom (group III), Silicon (group IV) has an extra negative charge, that interacts with the nucleus of the Si atom through the attractive Coulomb potential, but screened by the core and the other valence electrons. The other source for screening comes from the valence electrons of the neighboring atoms of the host crystal. This gives the intuitive idea that the Silicon atom behaves effectively as though it were an hydrogen atom embedded in a medium where the attractive potential is weaker due to the screening effect. The consequence for the electron is that it is loosely bound to the Si ion and it can be easily ionized by thermal or electrical excitations. The exact calculation of this screening is a difficult task, and one way to overcome it is to assume a screening controlled by the dielectric constant of the host crystal in the electrostatic potential:

$$U = -\frac{e}{\epsilon r} \tag{2.54}$$

where ϵ is the dielectric constant. We will use this as the Coulomb potential produced by the impurity ion. The Silicon impurity is also in our case a *shallow impurity*: the electronic states associated to it have an energy close to the conduction band such that they can be calculated in the effective-mass approximation, as we will see below. The approximation made for U is our starting point in our path towards the derivation of the equation describing the donor state. We recall that based on the previous ideas we expect an hydrogen-like equation. On the other hand, we are under the conditions required for the Envelope-function approximation described before, because the potential in (2.54) is a smoothly varying one. We thus anticipate an envelope function solution for the

donor, multiplied by some Bloch Function. We perform here anyway the full derivation in order to see a concrete example of the EFA. In what follows we develop the derivation based on Bloch Functions, although the same result can be achieved in terms of Wannier functions, as it is neatly developed in Ref. [70].

Our derivation starts by considering the crystal Hamiltonian H_0 and the impurity potential U. To solve the problem of the full Hamiltonian, we will consider the case that we have a (non-degenerate) minimum of the conduction band at $\vec{k} = 0$. The unperturbed Hamiltonian H_0 is

$$H_0 = -\frac{\hbar^2}{2m_0}\nabla^2 + V_{crys}(\vec{r}) \tag{2.55}$$

whose solution is $\Psi_{n,k}(\vec{r}) \sim u_{n,k}(\vec{r})e^{i\vec{k}\cdot\vec{r}}$.

For the perturbed problem $H = H_0(\vec{r}) + U(\vec{r})$, we will propose a solution of the kind

$$\Psi = \sum_{n,k} A_n(k)\Psi_{n,k} \tag{2.56}$$

As usual, we try to isolate an equation for the A's, and therefore we insert the proposed solution into the full Schrödinger equation and we subsequently multiply the equation by

$$\int d\vec{r}\ \Psi_{n,k}^*$$

The following equation results

$$(E_n(k) - E)A_n(\vec{k}) + \sum_{n',k'}\langle n,\vec{k}|U|n',\vec{k'}\rangle A_{n'}(\vec{k'}) = 0 \tag{2.57}$$

We now examine the matrix element of the potential, accounting for the coupling between different Bloch states via the perturbation.

$$\langle n,\vec{k}|U|n',\vec{k'}\rangle = \int \Psi_{n,k}^*(-\frac{e^2}{\epsilon r})\Psi_{n',k'}d\vec{r} = \frac{1}{V}\int u_{n,k}^*(\vec{r})u_{n',k'}(\vec{r})e^{i(\vec{k'}-\vec{k})\cdot\vec{r}}(-\frac{e^2}{\epsilon r})d\vec{r} \quad (2.58)$$

where the u's are the periodic part of the Bloch function.

One can cast this matrix element into the form

$$\langle n, \vec{k}|U|n', \vec{k}'\rangle = \frac{1}{V}\int dr u^*_{n,k} u_{n',k'} e^{i(\vec{k}'-\vec{k})\cdot\vec{r}} U(\vec{r}) \tag{2.59}$$

$$= \frac{1}{V}\int dr *_{n,k} u_{n',k'} e^{i(\vec{k}'-\vec{k})\cdot\vec{r}} \sum_{k_u} e^{i(\vec{k}_u\cdot\vec{r})} U(\vec{k}_u) \tag{2.60}$$

$$= \frac{1}{V}\sum_{k_u} U(\vec{k}_u)\int dr u^*_{n,k} u_{n',k'} e^{i(\vec{k}'-\vec{k}+\vec{k}_u)\cdot\vec{r}} \tag{2.61}$$

$$= \frac{1}{V}\sum_{k_u,\vec{G}} U(\vec{k}_u)\delta_{G,k'-k+k_u}\int dr u^*_{n,k} u_{n',k'} e^{-i\vec{G}\cdot\vec{r}} \tag{2.62}$$

where the periodicity of the function $u^*_{n,k} u_{n',k'}$ has been taken into account in the last step by using an expansion over the reciprocal vectors $\vec{G}$. The Fourier transform of the potential U has been introduced. We recall that the electron is weakly bound to the ion, and so its wave function must resemble a conduction state in the band minimum, with contributions coming from small $\vec{k}$'s. Hence, we can restrict the values of $\vec{k}$, $\vec{k}'$ and $\vec{k}_u$ to a small region around 0, which leads to the condition $G = 0$ for the matrix elements we are dealing with. On the other hand, if we take the limit of $\vec{k}_u \to 0$, the delta function $\delta_{G0,k'-k+0}$ implies that

$$\int d\vec{r} u^*_{n,k}(\vec{r}) u_{n',k}(\vec{r}) \propto \delta_{n,n'}$$

The eq. (2.57) is thus reexpressed as

$$(E_c(k) - E)A_c(\vec{k}) + \sum_{k'}\langle c, \vec{k}|U|c, \vec{k}'\rangle A_c(\vec{k}') \sum_{n'\neq c,k'}\langle c, \vec{k}|U|n', \vec{k}'\rangle A_{n'}(\vec{k}') = 0 \tag{2.63}$$

for the conduction band $n = c$. A valid approximation, based on our previous remarks, is to discard the equation for $n \neq c$ and assume that the leading contribution

comes from only one band. We can additionally use for E_c the dispersion relation given by the effective-mass $\frac{\hbar^2}{2m^*}k^2$ approximation (valid for small $\vec{k}$) and the matrix element $\langle c, \vec{k}|U|c, \vec{k}'\rangle \to -\frac{4\pi e^2}{V\epsilon|\vec{k}'-\vec{k}|^2}$. The final result is

$$\left(\frac{\hbar^2}{2m^*}k^2 - E\right) A_c(\vec{k}) - \frac{4\pi e^2}{V\epsilon}\sum_{k'}\frac{1}{|\vec{k}-\vec{k}'|^2}A_c(\vec{k}') = 0 \tag{2.64}$$

In this equation it must be noted that $\vec{k}$ and $\vec{k}'$ lie within the first Brillouin zone (FB) and the restriction can be safely omitted. By extending the sum over $\vec{k}'$ beyond the FB zone, we end up with the equivalent equation

$$\left(\frac{\hbar^2}{2m^*}k^2 - E\right) A_c(\vec{k}) - \frac{4\pi e^2}{V\epsilon}\sum_{\text{all k'}}\frac{1}{|\vec{k}-\vec{k}'|^2}A_c(\vec{k}') = 0 \tag{2.65}$$

The Schrödinger equation in momentum space is recognized by transforming $A_c(\vec{k})$ to the coordinate space $F(\vec{r}) = \frac{1}{V^{1/2}}\sum_{\text{all k}} A_c(\vec{k})e^{i\vec{k}\cdot\vec{r}}$ We thus get

$$\left(\frac{\hbar^2}{2m^*}\nabla^2 - \frac{e^2}{\epsilon r}\right) F(\vec{r}) = EF(\vec{r}). \tag{2.66}$$

The envelope function $F(\vec{r})$ represents the solution to the hydrogen-like problem of an electron with a renormalized mass m^* in the presence of a Coulomb potential diminished by a factor of ϵ. The eigenenergies for the problem are well-known

$$E_j = \frac{1}{j^2}\frac{(e^2/\epsilon)^2}{2\hbar^2 m^*} \quad \text{j} = 1,2,... \tag{2.67}$$

whereas the eigenfunction for the ground state is

$$F(\vec{r}) = \frac{1}{\sqrt{\pi a^{*3}}}e^{-r/a^*}. \tag{2.68}$$

The redefinition of the mass and the dielectric constant also determines the effective

Bohr Radius

$$a^* = \frac{\hbar^2 \epsilon}{m^* e^2}.$$

Even though this formulation leads us to the initial intuitive idea that a donor electron should effectively behave as in hydrogen-like landscape, it is worth pointing out that the function $F(\vec{r})$ is not the total wave function. The full wave function is in fact the linear combination

$$\Psi(\vec{r}) = \sum_k A_c(\vec{k}) \Psi_{c,k}(\vec{r}) = \frac{1}{\sqrt{V}} \sum_k A_c(\vec{k}) u_{c,k} e^{i\vec{k}\cdot\vec{r}} \tag{2.69}$$

As we said before, $A_c(\vec{k})$ is confined in a small range around $\vec{k} = 0$ and hence we only keep $u_{c,k}$ for small $\vec{k}$.

$$u_{c,k} \simeq u_{c,0}$$

which turns the aforementioned linear combination into

$$\Psi(\vec{r}) \sim u_{c,0}(\vec{r}) F(\vec{r}) = F(\vec{r}) \, u_{c,0}(\vec{r}) e^{i\mathbf{0}\cdot\vec{k}}$$

where we explicitly added in the last term the exponential in order to highlight that the total wave function is indeed an envelope function multiplying a Bloch function. The approximation made for $A_c(\vec{k})$ can be verified by noting that its magnitude is appreciable for $\vec{k}$ less than $1/a^*$. The contribution from the other bands can also be shown to be negligible as long as the effective Bohr radius is large

$$|A_n| \sim \frac{E_0}{E_g} \frac{a}{a^*} |A_0|$$

with E_0 the ionization energy and E_g the band gap. We have just treated the case of a single impurity, and found the shape of the ground state of the donor electron. Yet in

a bulk semiconductor sample there are many impurities. For our purposes, a model is needed for the electron in the presence of many randomly placed impurities. For this, we rely on the Matsubara-Toyozawa Model described in the end of this chapter.

Concerning the impurities, we finally address the SOC term calculation related to the electrical potential produced by themselves.

2.8 An effective SOC derivation

In this section we work out the derivation of an effective spin-orbit coupling term arising from the impurity potential. For this, we aim at decoupling the conduction band from the valence band, in a similar way as the one done in Ref. [76] by Nozieres and Lewiner. Though the procedure followed by the authors is physically transparent, it can also be stated in a more formal -yet less transparent- way known as quasi-degenerate perturbation theory. We make some remarks about this in the sequel.

We now start our derivation that goes along the same line as that of Ref. [76]. In our case, the time-independent Schrödinger equation is used instead, since we do not consider any time-dependent effect, but we arrive to the same result. We consider the Schrödinger equation in matrix form,

$$
E \begin{pmatrix} \psi_1 \\ \psi_2 \end{pmatrix} = \begin{pmatrix} H_1 & h \\ h^\dagger & H_2 \end{pmatrix} \begin{pmatrix} \psi_1 \\ \psi_2 \end{pmatrix} \tag{2.70}
$$

where we have split ψ into two parts. The term ψ_1 corresponds to the component in the conduction band "subspace", while all the other bands components are assigned to some ψ_2.

The origin of energy is set to the bottom of the conduction band, H_1 is thus of the order of a typical conduction electron energy, i.e. ϵ_F, and H_2 is of the order of the band gap. We redefine it as $H_2 = H'_2 + H_g$ in order to measure the valence state energies from the valence state at $\vec{k} = 0$. We also assume that H'_2 is an intraband Hamiltonian.

Despite the authors deal with time-dependent Hamiltonians, we restrict our case to the more simplified case of a static interaction denoted h. The approximation to be made considers that the band gap is much larger than the Fermi energy ϵ_F, and it is thus possible to make an expansion over $1/H_g$. We can formally express the solution

$$\psi_2 = \left(\frac{1}{E - H_2}\right) h^\dagger \psi_1$$

The term with the denominator can be approximated as

$$\frac{1}{E - H_2} = -\frac{1}{H_2}\frac{1}{\left(1 - \frac{E}{H_2}\right)} \approx -\frac{1}{H_2}\left(1 + \frac{E}{H_2}\right)$$

since H_2 is of the order of the band gap. On the other hand,

$$\frac{1}{H_2} = \frac{1}{H_g + H_2'} \approx \frac{1}{H_g}\left(1 - \frac{H_2'}{H_g}\right).$$

Within these approximations, the expression for ψ_2 translates into

$$\psi_2 = -\frac{1}{H_g}\left(1 + \frac{E}{H_g} - \frac{H_2'}{H_g}\right) h^\dagger \psi_1 \tag{2.71}$$

We will need later

$$\langle \psi_2 | \psi_2 \rangle = \langle \psi_1 | \Delta | \psi_1 \rangle \tag{2.72}$$

where we have consistently kept terms up to second order $1/H_g^2$ and defined

$$\Delta = h\frac{1}{H_g^2}h^\dagger$$

.

By replacing ψ_2 in the eq. (2.70), we finally get an eigenvalue equation for ψ_1.

$$\left(1 + h\frac{1}{H_g^2}h^\dagger\right)E\psi_1 \;=\; \left(H_1 - h\frac{1}{H_g^2}h^\dagger + h\frac{1}{H_g}H_2'\frac{1}{H_g}h^\dagger\right)\psi_1 \tag{2.73}$$

$$E(1 + \Delta)\psi_1 \;=\; \mathbf{H}\psi_1. \tag{2.74}$$

The operator $\mathbf{H}$ is defined in an obvious way. We then attained an equation for ψ_1 that is decoupled from the subspace ψ_2. Furthermore, an effective Schrödinger equation can be derived by multiplying from the left with $(1 - \frac{\Delta}{2})$.

$$\begin{aligned}
\left(1 - \frac{\Delta}{2}\right)E\left(1 + \Delta\right)\psi_1 &= (1 - \frac{\Delta}{2})\mathbf{H}\psi_1 \\
\left(1 - \frac{\Delta}{2}\right)E\left(1 + \Delta\right)\psi_1 &= \left(1 - \frac{\Delta}{2}\right)\mathbf{H}\left(1 - \frac{\Delta}{2}\right)\left(1 + \frac{\Delta}{2}\right)\psi_1 \\
E\left(1 + \frac{\Delta}{2}\right)\psi_1 &= \left(1 - \frac{\Delta}{2}\right)\mathbf{H}\left(1 - \frac{\Delta}{2}\right)\left(1 + \frac{\Delta}{2}\right)\psi_1
\end{aligned} \tag{2.75}$$

by noting that $(1 + \frac{\Delta}{2})(1 - \frac{\Delta}{2}) = 1$ up to second order.

The eq. (2.75) allows us to define the effective wave function

$$|\psi_{eff}\rangle = \left(1 + \frac{\Delta}{2}\right)\psi_1$$

and an effective Hamiltonian given by

$$H_{eff} = \left(1 - \frac{\Delta}{2}\right)\mathbf{H}\left(1 - \frac{\Delta}{2}\right) = H_0 - \frac{H_0\Delta + \Delta H_0}{2} + h\frac{1}{H_g}H_2'\frac{1}{H_g}h^\dagger \tag{2.76}$$

with $H_0 = H_1 - h\frac{1}{H_g}h^\dagger$. It is important to note that the newly defined effective function is properly normalized, since

$$\langle\psi_{eff}|\psi_{eff}\rangle = \langle\psi_1|1 + \Delta|\psi_1\rangle = \langle\psi_1|\psi_1\rangle + \langle\psi_1|\Delta|\psi_1\rangle = \langle\psi_1|\psi_1\rangle + \langle\psi_2|\psi_2\rangle = 1$$

for which the relation previously found in eq. (2.72) has been used.

As we mention in the beginning, the theory just exposed can be framed in quasi-perturbation theory as well. This is a more general and abstract avenue to treat the problem by means of a unitary transformation U, such that a new Hamiltonian

$$H' = UHU^\dagger \tag{2.77}$$

is made up out of the original one H. In general, the transformation operator U can be expressed as e^{-S} if S is an anti-Hermitian operator such that $S^\dagger = -S$. On the other hand, two subspaces must be distinguished here: a subspace A that for us are the conduction states, and another one B (the valence band). The idea behind this approach is the same as before: the transformation we seek is such that the rotated Hamiltonian H' does not have any off-diagonal matrix element linking the two subspaces. The next step is to separate the original Hamiltonian in two parts

$$H = H_D + H_{ND}$$

where H_D is a block-diagonal Hamiltonian that couples the states *within* their corresponding subspaces. In our notation, this is $H_D = H_1 + H_2$. H_{ND}, on the other hand, stands for the coupling term that connects the two subspaces -in our case this is h. What the method pursues is the transformation matrix S that makes the matrix elements of H' between A-states and B-states to vanish up to the desired order. In order to be able to work order by order, the operator e^S can be expanded

$$e^S = 1 + S + \frac{1}{2!}S^2 + \frac{1}{3!}S^3$$

The condition on the removal of the non-diagonal elements in H' leads to a system of

equations for the successive approximation of $S = S^1 + S^2 + S^3 + ...$, that according to the Ref. [69] is, up to second order in $1/H_g^2$:

$$S^{(1)} = \begin{pmatrix} 0 & -\frac{h}{H_g} \\ \frac{h^\dagger}{H_g} & 0 \end{pmatrix} \tag{2.78}$$

and

$$S^{(2)} = \begin{pmatrix} 0 & -\frac{1}{H_g}\left[\frac{H_1 h}{H_g} - \frac{h H_2'}{H_g}\right] \\ -\frac{1}{H_g}\left[\frac{h^\dagger H_1}{H_g} - \frac{H_2' h^\dagger}{H_g}\right] & 0 \end{pmatrix} \tag{2.79}$$

The effective Hamiltonian H' after computing all the commutators between H and S up to order $1/H_g^2$ is exactly the same as that of eq. (2.76).

To apply this method to the specific case of the conduction and the valence band in a wide gap semiconductor like GaAs, we must consider the aforementioned $\vec{k} \cdot \vec{p}$ equation or EFA equation with the electron mass renormalized. The interaction that couples the subspace A and B is the operator $\vec{k} \cdot \vec{\Pi} = h$ with $\vec{k} = -i\nabla$ (the canonical momentum) and $\vec{\Pi}$, the vector operator with matrix elements

$$\Pi_{nn'} = \langle u_{n,0}| - \frac{i\nabla}{m_0}|u_{n',0}\rangle, \tag{2.80}$$

i.e. those from the Kane Theory. In order to take into account the impurities, we introduce in the conduction band the impurity Coulomb-like potential "V_1" and in the valence band the equivalent one "V_2"; we consider that this potential does not contribute to the interband coupling v. Hence

$$V_1 = V_2 = V(\vec{r}) \tag{2.81}$$
$$v = 0$$

with $n = 1$, which must be multiplied with $k_\alpha k_\beta V_1$ and $V_1 k_\alpha k_\beta$. These two terms are symmetric under $\alpha \to \beta$ if they commute, and therefore, the multiplication with the spin-dependent part including $\epsilon_{\alpha\beta\gamma}$ cancels out. Conversely, the contribution of the impurity potential in the valence band yields a term proportional to

$$k_\alpha V_2 \, k_\beta \epsilon_{\alpha\beta\gamma} \tag{2.85}$$

Due to the *non-commutation* of k_β and V_2, the preceding equation transforms into

$$k_\alpha \left(k_\beta V_2 - \frac{\partial V_2}{\partial x_\beta} \right) \epsilon_{\alpha\beta\gamma} \tag{2.86}$$

The first term is again zero due to the "contraction" of a symmetric and an anti-symmetric tensor, while the second one gives the sought result

$$\left(\vec{k} \times \nabla V_2 \right) \cdot \mathbf{S} \tag{2.87}$$

Two important points to be mentioned are that according to eq. (2.84), the spin-orbit contribution of the impurities is zero if Δ_0 is set to zero. We have also made use of the commutation of k_β and k_α, which is no longer valid when a magnetic field (and thus the substitution $(\vec{k} \to -i\nabla - e\vec{A}/c$) is introduced.

In conclusion, for a conduction-band electron in the absence of spin-orbit interaction, the electron acquires an effective-mass and in a first approximation and close to the band extrema, the energy dispersion is quadratic with a renormalized mass. Due to the presence of the external potential $V(\mathbf{r})$, there appears a "Rashba-like" or "Structural Inversion Asymmetry" (SIA) spin-orbit interaction [69,76–78], that we call here *extrinsic* term to emphasize that it is an potential produced by the impurities

$$H_{\text{ext}} = \lambda^* \boldsymbol{\sigma} \cdot \nabla V \times \vec{k}, \tag{2.88}$$

where $\boldsymbol{\sigma}$ is the vector of Pauli matrices, $\mathbf{k} = \mathbf{p}/\hbar$, and λ^* is the effective spin-orbit coupling constant given by

$$\lambda^* = \frac{|P|^2}{3}\left[\frac{1}{H_g^2} - \frac{1}{(H_g + \Delta_0)^2}\right] \tag{2.89}$$

It is interesting to note that while the vacuum coupling constant is $\lambda_0 = \hbar^2/4\,m_0^2 c^2 \simeq 3.7 \times 10^{-6}\text{Å}^2$, the renormalized one is, for example, $\lambda^* \simeq -5.3\,\text{Å}^2$ for GaAs and $\lambda^* \simeq -120\,\text{Å}^2$ for InAs, that is, more than six orders of magnitude larger.

We have presented an illustrative way of deriving an effective Hamiltonian for the SOC, that allowed us to examine its precise origin. Nevertheless, there is yet another equivalent approach to take into account the effect of the spin-orbit coupling and the potential produced by the impurities. It consist of extending the Matsubara-Toyozawa in order to incorporate the spin-orbit interaction in the impurity states. We next continue in the next section with the description of the Matsubara-Toyozawa model in its original version, and leave the extension proposed in Ref. [79] for the first part of next chapter, as an intermediate step before we present our results for this extended model.

2.9 The Matsubara-Toyozawa Model

The Matsubara-Toyozawa tackles the problem of an electron in a random lattice. Their pioneering work dealt with a high degree of impurity concentration, but *not* as high as to set the Fermi energy in the conduction band. Some works before the MT publication had used perfectly mobile states (from the energy band), and took into account the effect of the disorder within a perturbative scheme. Alternatively, others started with localized states, and the effect of the disorder gives rise to hopping events of the carriers. The common point in both approaches is that the initial states differ little from an eigenstate. Matsubara and Toyozawa studied instead the case where the eigenstates of the system had neither a definite momentum nor a definite localization. In this theory, there is

no "disturbance" that cause the scattering of carriers, because the random potential is already included in the calculation of the impurity band. Based on the Green Function formalism, they analytically obtained the level density and the electrical conductivity. In this work we will be mainly concerned with their model and not with their results.

The MT model consists of a tight-binding approximation built from the ground state (the hydrogenic-like s state) of the doping impurities we have seen in Section (2.7).

$$\psi_\sigma(\vec{r}) = \sum_{\vec{k}} \phi(\vec{k}) \, e^{i\vec{k}\cdot\vec{r}} \, u_{\vec{k},\sigma}(\vec{r}) \approx \phi(\vec{r}) \, u_{\vec{k}=0,\sigma}(\vec{r}). \tag{2.90}$$

We denote $\phi(\vec{k})$ the Fourier transform of the hydrogenic envelope function, while $u_{\vec{k},\sigma}(\vec{r})$ represents the periodic part of the Bloch functions of the conduction band states. Its dependence on $\vec{k}$, is much smoother than that of $\phi(\vec{k})$, and leads to the last relation in eq. (2.90). In second-quantization notation, the Hamiltonian of the MT model can be simply expressed as

$$H_0 = \sum_{m\neq m',\sigma} t^{\sigma\sigma}_{mm'} \, c^{\dagger}_{m'\sigma} \, c_{m\sigma}, \tag{2.91}$$

where $c^{\dagger}_{m'\sigma}$ represents the creation operator of an electron eigenstate at the impurity site m'. The annihilation operation is $c_{m\sigma}$. The integral for the energy transfer from site m to m' is given by a sum over impurities p's

$$t^{\sigma\sigma}_{mm'} = \sum_{p\neq m} \langle\psi_{m'\sigma}|V_p|\psi_{m\sigma}\rangle \, , \tag{2.92}$$

while the Coulomb-like potential produced by the impurity placed at $\vec{r}_p$ is

$$V_p(\mathbf{r}) = -e^2/\epsilon|\mathbf{r} - \mathbf{r}_p|$$

We use ϵ for the static dielectric constant and e for the electron charge. Due to the exponential decay of the envelope functions, the dominant term in eq. (2.92) is the two-center integral corresponding to $p = m'$ and so

$$\langle\psi_{m'\sigma}|V_{m'}|\psi_{m\sigma}\rangle = -V_0 \left(1 + \frac{r_{mm'}}{a}\right) \exp\left(-\frac{r_{mm'}}{a}\right), \tag{2.93}$$

with $V_0 = e^2/\varepsilon a$ and $r_{mm'}$ being the distance between the two impurities.

Back in the beginning of the eighties, the Hamiltonian in eq. (2.91) was studied using different analytical and numerical techniques [80–83], yielding a thorough description of the impurity band and its electronic transport properties. In addition, MT was employed as a realistic model to study the Anderson Transition in three dimensional doped semiconductors [82]. It must be clear that the MT Model does not take into account the spin degree of freedom, and in consequence we must find the proper way to include it. This was firstly done in Ref. [79], where the model was extended and the impurity states modified accordingly.

We begin next chapter by describing this Impurity Spin-Admixture theory, and we subsequently apply it to study how the spin-orbit interaction affects the localization of the eigenstates.

Chapter 3

SOC in the impurity band

In this section we study numerically the effects of the spin-orbit interaction in n-doped semiconductors in a model closely related to the one we have just exposed: the Matsubara and Toyozawa. The influence of the SOC on the density of states (DOS) and the calculation of the so-called inverse participation ratio (IPR) are addressed. The latter term is utilized for characterizing the degree of localization of the spin-orbit perturbed states in the MT set of eigenstates.

In the numerical treatment of the problem, the finite sizes that we are able to consider force us to introduce an artificial enhancement of the spin-orbit coupling strength in order to obtain a sizeable perturbation. The IPR and DOS are then obtained as a function of an enhancement parameter. This study allows us on the one hand to appreciate the effect of the SOC on the impurity band, and at the same time, to examine the coexistence of localized and extended states in this band. In particular, the degree of spatial extension at the Fermi energy is of crucial importance in the ensuing problem of the spin relaxation, where besides the extrinsic contribution to the SOC, we also consider the Dresselhaus term. Although this latter term turns out to play a relevant role in relaxation, we do not include it here. The enhancement procedure followed in this chapter provides us with a qualitative description of the impurity band, and as we do not aim at any quantitative result, the inclusion of the Dresselhaus term is not determinant.

3.1 Presentation

In this chapter we focus on the effect of the spin-orbit interaction in n-doped semi-conductors when the doping density is close to the critical density associated to the metal-insulator transition (MIT). For a n-doped GaAs, the *critical* density occurs at $n_c = 2 \cdot 10^{16} cm^{-3}$. Since in the case of the n-doped semiconductors, the MIT appear at doping densities where the Fermi level is in the impurity band [84, 85], a description taking into account only the electronic states built from the hydrogenic ground state of the doping impurities is suitable. For densities slightly larger than the critical one (i.e. on the metallic side of the transition) non-interacting models, like the Matsubara-Toyozawa (MT) [80], are applicable. Furthermore, the description in terms of impurity sites can be regarded as an Anderson model of a tight-binding lattice with on-site or hopping disorder. In the profuse numerical work devoted to the Anderson model [86], the critical exponents obtained fit reasonably well those of the experimental measure-ments [87]. The inclusion of spin is equally interesting, in view of the fact that the maximum spin relaxation times in n-doped semiconductors have been observed for im-purity densities close to that of the MIT [25, 26, 30, 88]. At the level of models, the generalization of the Anderson model in order to include some spin-orbit coupling has been provided by Ando [89]. While this model turns out to be very useful to study the progressive breaking of the spin symmetry [90], its connection with experimentally relevant systems requires the estimation of coupling parameters which are not obtain-able from first principles. In order to adapt the problem of the spin-relaxation in three dimensional systems, Tamborenea and collaborators [79] reviewed the MT model and incorporated in it the spin-orbit interaction. In their proposition, the impurity states are no longer spin eigenstates, but a spin mixture of *up* and *down* states.

As we make use of the Impurity Spin-Admixture (ISA) model in this chapter, we start by describing it in the following section. Immediately after this, we present the results obtained in the context of this thesis, starting with a preliminary study of the "bare" MT model. After including the SOC interaction, we proceed with the characterization of the impurity band. We then identify the regions of extended and localized states, and

analyze the limitations of the model and the conditions of applicability.

3.2 Tight-binding model with impurity spin admixture

We found before that the donor wave function can be approximated by

$$\Psi(\vec{r}) = u_{c,0}(\vec{r})F(\vec{r}) \tag{3.1}$$

where $u_{c,0}$ denotes the periodic Bloch function in the band center ($\vec{k} = 0$) and $F(\vec{r})$ is an envelope function. In order to introduce the spin, we switch to the spinor notation and generalize this solution :

$$[\Psi_\sigma(\vec{r})] = F(\vec{r})[u_{c,0}(\vec{r})] \tag{3.2}$$

So far this spinor is trivial because it is an eigenstate of σ_z with eigenvalues $\sigma = \pm 1$. This will be no longer the case once the spin-orbit interaction is included. By way of reminder, we have observed before that the valence band is split at the Γ point due to the SOC, and its degeneracy is partially lifted. The *split-off* band ($j = 1/2$) separates from the *light-hole* and the *heavy-hole* bands ($j = 3/2$) by an amount equal to Δ_0. We have also found that the hydrogenic character of the envelope function fits very well in our intuitive conception of the donor electron. With SOC the expressions for these states are not so simple however, as it renders the description of the wave function a bit more sophisticated. To see how, we must step back to the very beginning, and recall that a Bloch Function can be written (in spinor language)

$$[\Psi_{n\vec{k}}](\vec{r}) = e^{i\vec{k}\cdot\vec{r}}[u_{n\vec{k}}]$$

Equivalently, one can use the following expansion

$$[\Psi_{n\vec{k}}](\vec{r}) = e^{i\vec{k}\cdot\vec{r}} \sum_n c_n(\vec{k})[u_{n\,\vec{k}=0}]$$

which turns out to be more convenient when the bands a weakly coupled. By setting a 8×8 Kane model, where the s-like ($j = 1/2$) and the three p-like valence ($j = 3/2$ and $j = 1/2$ separated by Δ_0) bands are taken into account, the $\mathbf{k} \cdot \mathbf{p}$ Hamiltonian can be exactly diagonalized. By solving for the eigenenergies and the eigenvectors, one finds that the conduction-band states at finite wave vector get spin-mixed, whereby the total wave function now becomes

$$[\Psi_{c\vec{k}}](\vec{r})] = e^{i\vec{k}\cdot\vec{r}} \sum_n c_n(\vec{k})[u_{n\,\vec{k}=0}] \rightarrow e^{i\vec{k}\cdot\vec{r}} [\tilde{u}_{\mathbf{k}\sigma}]$$

The periodic function $[u_{0,c}]$ in eq. (3.2) has been replaced by a spin-mixed conduction-band state, that in bra-ket notation, is given [91] by

$$|\tilde{u}_{\mathbf{k}\sigma}\rangle = |u^\sigma_{(0)}\rangle + \mathbf{k} \cdot |\mathbf{u}^\sigma_{(1)}\rangle, \tag{3.3}$$

where the second term reads

$$|\mathbf{u}^\sigma_{(1)}\rangle = \alpha_1 \left(|\mathbf{R}\sigma\rangle + \alpha_2 \mathbf{S} \times |\mathbf{R}\sigma\rangle \right). \tag{3.4}$$

The state $|u^\sigma_{(0)}\rangle$ is s-like and is equal to the original state $u_{c,0}(\vec{r})$ in eq. (3.2), since it describes the unperturbed wave function at the Γ-point. The vector $|\mathbf{R}\rangle = (|X\rangle, |Y\rangle, |Z\rangle)$ represents the three p-like valence states and $\mathbf{S}$ is the spin operator. Obviously, the state $|\tilde{u}_{\mathbf{k}\sigma}\rangle$ is then no longer an eigenstate of S_z. However, it is still labeled with σ since the mixing is small, and $\langle \tilde{u}_{\mathbf{k}\sigma}|S_z|\tilde{u}_{\mathbf{k}\sigma}\rangle$ is much closer to $\frac{\sigma\hbar}{2}$ than to $\frac{-\sigma\hbar}{2}$. In relation to this, the spin mixing is weighted by the small constants

$$\alpha_1 = i\hbar \left(\frac{3E_G + 2\Delta_0}{6m^* E_G(E_G + \Delta_0)} \right)^{1/2}$$

and

$$\alpha_2 = \frac{2\Delta_0}{i\hbar(2\Delta_0 + 3E_G)}.$$

where all the constants keep the same meaning as in the previous chapters.

In order to extend the MT model and incorporate the SOC in the model, Tamborenea *et al.* [79] propose to generalize the shallow-donor wave functions: these functions are built out of conduction states, and therefore they are expected to be modified accordingly. However the SOC coming from the microscopic crystal details does not modify in an appreciable way the envelope functions $\phi(r)$, and will mainly affect the spinor part $[u_{\mathbf{k}}]$. The mixing of different bands turns the complete donor state of an impurity centered at $\mathbf{r}_m$ into

$$
\left[\tilde{\psi}_{m\sigma}\right](\mathbf{r}) \;=\; \phi(\mathbf{r}-\mathbf{r}_m) \times \left(\left[u_\sigma^{(0)}\right](\mathbf{r}) + \frac{i}{a}\frac{(\mathbf{r}-\mathbf{r}_m)}{|\mathbf{r}-\mathbf{r}_m|}\cdot\left[\mathbf{u}_\sigma^{(1)}\right](\mathbf{r}) \right). \tag{3.5}
$$

In Appendix B the detailed derivation of this term is worked out. The hopping of an electron between different ISA states involve the hopping between different impurity sites, and it provides a mechanism for spin flip by connecting the σ and $\overline{\sigma} = -\sigma$ states. It must be noted that even a spin-independent potential like the impurity Coulomb potential induces spin-flip transitions, since it couples states with different spin orientations. Similarly to eq. (2.91), the EFA Hamiltonian expressed in second-quantization language is now

$$
H = H_0 + H_1 = \sum_{m\neq m',\sigma} t_{mm'}^{\sigma\sigma}\, c_{m'\sigma}^\dagger\, c_{m\sigma} + \sum_{m\neq m',\sigma} t_{mm'}^{\sigma\overline{\sigma}}\, c_{m'\overline{\sigma}}^\dagger\, c_{m\sigma}. \tag{3.6}
$$

where H_1 describes the spin-flip term. The transition matrix elements are given by

$$
t_{mm'}^{\sigma\overline{\sigma}} = \sum_{p\neq m}\langle\tilde{\psi}_{m'\overline{\sigma}}|V_p|\tilde{\psi}_{m\sigma}\rangle\,, \tag{3.7}
$$

whose addends read

$$
\begin{aligned}
\langle\tilde{\psi}_{m'\overline{\sigma}}|V_p|\tilde{\psi}_{m\sigma}\rangle =\;& C \int d^3r \frac{(r-r_m)_-(z-z_{m'})-(z-z_m)(r-r_{m'})_-}{|\mathbf{r}-\mathbf{r}_m|\,|\mathbf{r}-\mathbf{r}_p|\,|\mathbf{r}-\mathbf{r}_{m'}|} \\
& \exp\left(-\frac{[|\mathbf{r}-\mathbf{r}_m|+|\mathbf{r}-\mathbf{r}_{m'}|]}{a}\right)
\end{aligned} \tag{3.8}
$$

The following definitions have been used

$$C = V_0 |\alpha_1|^2 \alpha_3 / \pi a^4,$$

$$r_{\pm} = x \pm iy,$$

and

$$\alpha_3 = 3\Delta_0(\Delta_0 + 2E_G)/(2\Delta_0 + 3E_G)^2.$$

In order to calculate the integral in eq. (3.8), a rotation of coordinates from the crystallographic system (x, y, z) is performed. The new system has the z-axis along the line joining m and m'. Taking the origin at the middle point between these impurities, scaling all lengths with the distance $r_{mm'}/2$, and using dimensionless cylindrical coordinates $(\mathcal{Z}, \rho, \phi)$, the following expression is computed (see AppendixA)

$$
\begin{aligned}
\langle \tilde{\psi}_{m'\bar{\sigma}} | V_p | \tilde{\psi}_{m\sigma} \rangle &= \frac{C e^{i\varphi_{mm'}} r_{mm'}^2}{2} \int_{-\infty}^{+\infty} d\mathcal{Z} \int_0^{\infty} d\rho \int_0^{2\pi} d\phi \\
&\quad \cdot \frac{\rho^2 (\cos\phi + i \, \cos\theta_{mm'} \sin\phi)}{\left[\rho^2 + \rho_p^2 + (\mathcal{Z} - \mathcal{Z}_p)^2 - 2\rho\rho_p \cos(\phi - \phi_p)\right]^{1/2}} \\
&\quad \cdot \frac{\exp\left(-r_{mm'}\left[\sqrt{\rho^2 + (\mathcal{Z}-1)^2} + \sqrt{\rho^2 + (\mathcal{Z}+1)^2}\right]/2a\right)}{\sqrt{\rho^2 + (\mathcal{Z}-1)^2}\sqrt{\rho^2 + (\mathcal{Z}+1)^2}}
\end{aligned}
\tag{3.9}
$$

where $\varphi_{mm'}$ and $\theta_{mm'}$ are the polar angles of the vector $\mathbf{r}_{mm'}$ in the original coordinate system, and $(\mathcal{Z}_p, \rho_p, \phi_p)$ are the cylindrical coordinates of $\mathbf{r}_p$ in the new coordinate system.

As in the spin-conserving model, we first look at the case with $p = m'$. The corresponding two-center integral is obtained by putting $\mathcal{Z}_p = 1$, $\rho_p = 0$ in eq. (3.9). Interestingly, $\langle \tilde{\psi}_{m'\bar{\sigma}} | V_{m'} | \tilde{\psi}_{m\sigma} \rangle = 0$ due to the symmetry of the angular integral. As a remark, this important fact is ultimately responsible for the large values of the spin lifetime given by this type of coupling in the regime of impurity-band conduction. This said, looking back to the integral, the leading order is then determined by the three-center integrals

corresponding to $p \neq m, m'$, which are in general very difficult to calculate in closed form [92]. The angular integral in eq. (3.9) can be performed in terms of elliptic functions, but since only the small arguments of the latter are relevant for the remaining integrals, the following expression results

$$
\begin{aligned}
\langle \tilde{\psi}_{m'\bar{\sigma}} | V_p | \tilde{\psi}_{m\sigma} \rangle \quad = \quad & \frac{C e^{i\varphi_{mm'}} \pi r_{mm'}^2}{4} \rho_p (\cos \phi_p + i \, \cos \theta_{mm'} \sin \phi_p) \\
& \cdot \int_{-\infty}^{+\infty} d\mathcal{Z} \int_0^{\infty} d\rho \left(\frac{\rho^2}{\rho^2 + \rho_p^2 + (\mathcal{Z} - \mathcal{Z}_p)^2} \right)^{3/2} \\
& \cdot \frac{\exp \left(-r_{mm'} \left[\sqrt{\rho^2 + (\mathcal{Z} - 1)^2} + \sqrt{\rho^2 + (\mathcal{Z} + 1)^2} \right] /2a \right)}{\sqrt{\rho^2 + (\mathcal{Z} - 1)^2} \, \sqrt{\rho^2 + (\mathcal{Z} + 1)^2}} . \quad (3.10)
\end{aligned}
$$

Using this expression for the matrix element, we can next focus on how the character of the MT eigenstates changes under the spin-orbit coupling strength.

In order to characterize the electronic eigenstates in the impurity band from the point of view of their spatial extension, we obtain numerically the eigenvalues and eigenstates $\{\varepsilon_i, \psi_i\}$ of $\mathcal{H}$ for given configurations in which N impurities are randomly placed in a three-dimensional volume. For each configuration we calculate the energy-dependent density of states,

$$
\text{DOS} = \sum_i \delta(\varepsilon - \varepsilon_i), \quad (3.11)
$$

and the inverse participation ratio of the state $|\psi_i\rangle$,

$$
\text{IPR} = \left[\frac{\sum_m^N |\langle \phi_m | \psi_i \rangle|^4}{\left(\sum_m^N |\langle \phi_m | \psi_i \rangle|^2 \right)^2} \right]^{-1} . \quad (3.12)
$$

According to this definition, the IPR approaches the system size N for extended states, while it is equal to 1 for a localized one. In the following section we present the results for these two quantities obtained for the MT Model, before introducing the SOC.

3.3 The impurity band from the Matsubara-Toyozawa model

We first start by considering the bare MT model without spin. For this purpose, we perform an exact diagonalization of the MT Hamiltonian, for a given configuration, and calculate the Density of States from its energy spectrum. By solving also for the eigenstates, the corresponding IPR for each eigenstate is computed. This process is repeated for many disorder realizations, and the resulting averages for both quantities is shown in Fig. 3.1. Three densities on the metallic side of the transition were considered. Each of the panels contains different system sizes, distinguished by the solid, dashed and dotted lines. As we can see, the impurity band develops around the $E = 0$ level of the isolated impurity in an asymmetric fashion: the DOS exhibits a long low-energy tail while the high-energy part is bounded by $E = 1$ (in units of V_0). We also verify that the width of the impurity band increases with the doping density, as we expect due to the stronger coupling between sites.

The numerically obtained DOS for different densities are well reproduced by approximate methods like diagrammatic perturbation obtained by Matsubara and Toyozawa [80]. Also the moment-expansion presented in Ref. [93] resembles our results. There, an adapted version of the moment expansion technique for disordered systems in three dimensions is employed to estimate the electronic density of states in the impurity band.

By looking at the IPR values, we observe that the highest-energy states correspond to electronic wave functions localized on small clusters of impurities. In these clusters, the strong coupling of adjacent sites gives rise to high-energy states. To illustrate this situation we can think on the extreme case of a cluster as a group of n impurities close to each other but far from any other *not* in the cluster. In it, they interact with each other so strongly that this will be represented in the Hamiltonian as a block (with a dimension equal to the number of sites in the cluster in question) matrix full of 1 (in units of V_0). If the diagonal elements are zero (a finite value would introduce a shift in

this extreme case) it can then be shown that the maximum eigenvalue of such a matrix is 1, irrespective of the system size. Furthermore, this eigenvalue is $(n-1)$-fold degenerate. The other eigenvalue of the matrix is $\epsilon = -n$ (in units of V_0). Since all the clusters, no matter their size, contribute to the DOS for $\epsilon = 1$, there will be a strong peak at such a value, and a long tail arising from the remaining eigenvalue $\epsilon = -n$ (the size of each cluster) plus the eigenvalues not associated with a given cluster. This could explain the tendency for the DOS to develop a "peak" close to one, and a roughly flat region for negative energies. The clustering of impurities is known to happen in real physical systems since impurities have a very weak long-range interaction, resulting in a lack of hard-core repulsion on the scale of the lattice constant [79, 94]. As the lattice constant does not appear any more, we use the letter a for the effective Bohr radius henceforth. In our model, we do not impose any kind of limit for the distance between impurities and this feature thus emerges.

Before continuing with the analysis of the numerical results obtained from the MT model, we discuss some technical features of the model and the difficulties that we face in trying to improve upon it. Firstly, we notice that the chosen basis set is not orthogonal. In principle, we can deal with this issue by writing a generalized eigenvalue problem which includes the matrix of orbital overlaps [81, 95]. This procedure results in unphysical high-energy states (with $E \gg 1$) that necessitate the inclusion of hydrogenic states beyond the $1s$ orbital in order to be properly described. However, care must be taken since enlarging the basis set leads to the problem of overcompleteness. Fortunately, for the properties we are interested in, the effects arising from non-orthogonality are known to be small for moderate doping densities, and that is why we do not consider them in the numerical work, thus staying within the original MT model. Finally, another drawback of the MT model is that the high-energy edge of the impurity band overlaps with the conduction band, which starts at $V_0/2$ (the effective Rydberg) and this effect is not included in the MT description. As seen in Fig. 3.1 the DOS beyond $V_0/2$ is always very small, and therefore we can ignore the effects that the hybridization of the bands would yield in a more complete model. As another remark, the development of tails at

the band edges we observe in our results is a characteristic feature of random disorder potential with long-range interaction [96].

The determination of the mobility edges by studying the size scaling of IPR/N values in Fig. 3.1 is not straightforward. We expect the value IPR/N to vanish for increasing N if the state is localized, and become independent of N for extended states. The difficulty in the determination of E_c (the mobility edge) arises from the heavily structured DOS of the MT model [81]. At low energy the small values of the DOS translates into a poor statistics for feasible sizes. In the high-energy part of the impurity band the separation between the curves corresponding to different values of N is masked by the small values of the IPR/N. For the highest density (top panel) the IPR/N exhibits a relatively flat region at intermediate energies, which is approximately independent of N for the two largest system sizes. The lower mobility edge can be located roughly at $E \sim 3.5$, where the latter curves separate. For lower impurity densities (lower panels) the previous analysis becomes increasingly demanding in terms of system sizes. We see that the flat region of IPR/N shrinks, from which we can conclude that the lower mobility edge is shifting towards higher values of E, as the density diminishes.

3.4 Spin-orbit coupling in the MT Model

We next include the spin in our model and basically repeat the procedure followed previously for characterizing the energy eigenstates. We address this by means of the Impurity-spin admixture proposed in Ref. [79], focusing at the extrinsic SOC. We take the term

$$\mathcal{H}_1 = \sum_{m \neq m', \sigma} t_{m'm}^{\sigma \overline{\sigma}} \, c_{m'\overline{\sigma}}^{\dagger} \, c_{m\sigma} \tag{3.13}$$

($\overline{\sigma} = -\sigma$) and add it to $\mathcal{H}_0$. Similarly to the spin-conserving case, we have

$$t_{mm'}^{\sigma \overline{\sigma}} = \sum_{p \neq m} \langle \tilde{\psi}_{m'\overline{\sigma}} | V_p | \tilde{\psi}_{m\sigma} \rangle \tag{3.14}$$
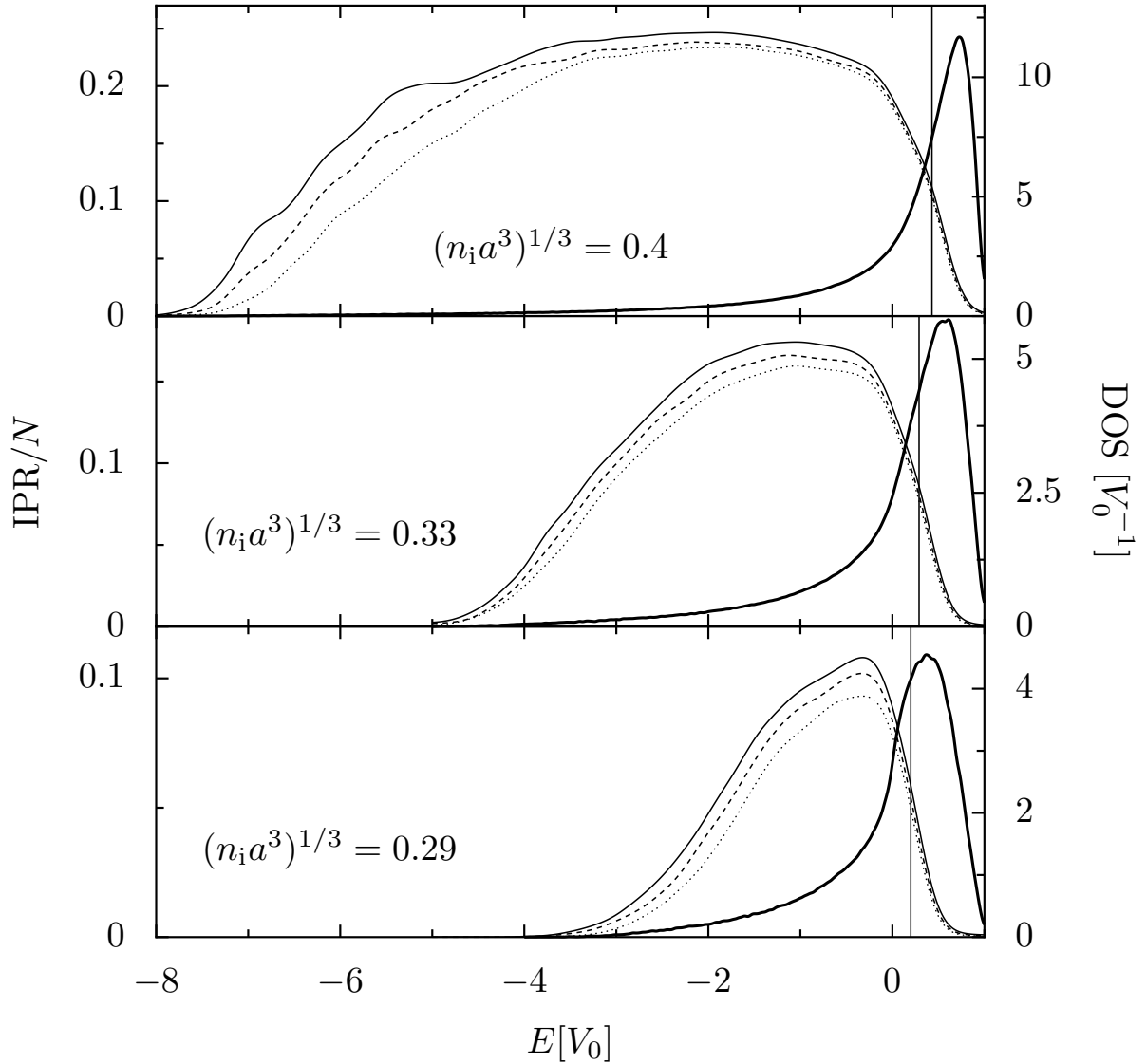
Figure 3.1: Density of states (DOS, thick line and right scale) and inverse participation ratio (IPR, thin lines and left scale) for three different densities on the metallic side of the metal-insulator transition, obtained through impurity averaging in the Matsubara-Toyozawa model. The solid, dashed and dotted curves of IPR/N are for a number of impurities $N = 2744, 4096$ and 5832, respectively. The vertical lines indicate the Fermi energy and the DOS are scaled with respect to the effective Bohr radius a.

with the wave function $\tilde{\psi}_{m\sigma}$ denoting the impurity spin-admixed (ISA) state. In Ref. [79] an approximate analytical expressions of $t^{\sigma\sigma}_{mm'}$ was provided using the saddle-point approximation, valid under the condition $r_{mm'} \gg a$. At the MIT, for example, this relation is $r_{mm'}/a = 3.7$. In this sense, we found that the analytical approximation proposed in [79] overestimates the real values. To avoid this approximation, we take the route of the numerical evaluation of the three-center integrals. We show typical absolute values of these matrix elements in Fig. 3.2 averaged over the orientation angles and over many realizations.

We next include the Hamiltonian $\mathcal{H}_1$ and carry out the diagonalization of the full Hamiltonian. Concerning the SOC strength, we note that the matrix element in eq. (3.14) is proportional to the effective spin-orbit coupling λ which for a zincblende semiconductor can be orders of magnitude larger than the one of vacuum $\lambda_0 \simeq 3.7 \times 10^{-6} \text{Å}^2$. For the case of GaAs we treat here, $\lambda \simeq -5.3 \text{Å}^2$ [69], which is notably different from bulk InAs with $\lambda = -120 \text{Å}^2$.

3.4.1 Spectral decomposition of MT states

The spin-admixture energy shifts are, even for the largest system sizes that we can treat numerically, orders of magnitude smaller than the MT level spacing. The consequence of this is that the eigenstates have either an almost-up spin orientation or an almost-down, and the spin-orbit-induced effects are not observable for the system sizes we are able to consider. We are then lead to consider an enhancement factor R_r that multiplies λ and makes the two previous energy scales comparable. The wave function are expected to acquire a stronger mixing of spin orientation. This effect is displayed in Fig. 3.3. In it, the spectral decomposition of a MT eigenstate (also called the local density of states LDOS) with $\sigma = 1$ in the basis of spin-admixed eigenstates of $\mathcal{H}_0 + \mathcal{H}_1$ is shown. The arrows $\uparrow$ and $\downarrow$ in the figures denote the two subspaces of the spin projection of the spin-admixed states. It must be noted that we leave this "tagging" even for the largely enhanced cases. We can observe that if there is no enhancement ($R_r = 1$), the spin
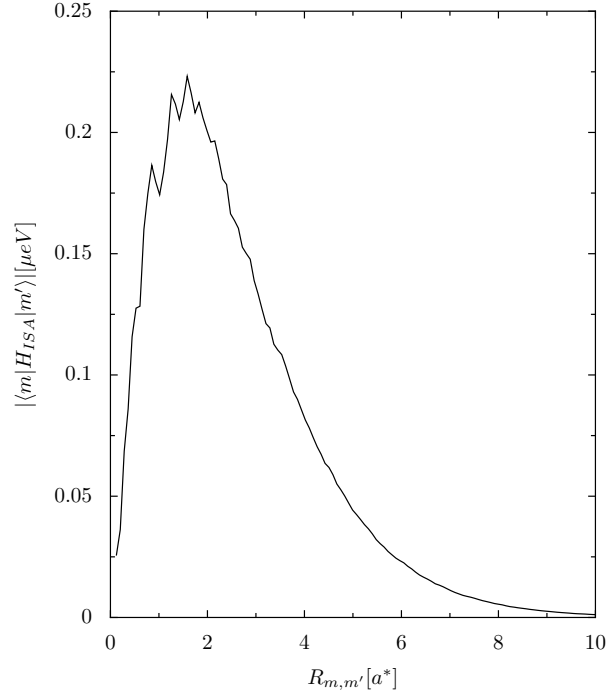
Figure 3.2: The absolute values of the matrix elements for the spin-flip hopping between two sites m and m' is shown as a function of the distance between them. H_{ISA} is the Coulomb potential generated by the randomly placed impurities.

polarized MT states projects very well onto one of the spin-admixed subspaces (look at the y-scale in the figure), in this case *up*. As R_r is increased, we obtain significant projections on both subspaces as a manifestation that the spin-admixture gets larger. This consideration on a given state shows the effect on a given MT state. Alternatively, the decomposition of an ISA eigenstate in the MT subspaces (each of them with a defined spin eigenvalue) is also expected to change in a similar way as the one just exposed. We study precisely the effect of the spin-orbit coupling both on the DOS and IPR of the ISA eigenstates, using R_r as a control parameter.

3.4.2 Inverse Participation Ratio and DOS

Since we have already described the procedure followed to calculate the DOS and the IPR in the spinless case, we only need to mention here the modification for the IPR as the spin degree of freedom is included.

Since the eigenstates of the full Hamiltonian are no longer spin eigenstates, the IPR should be calculated by projecting the state onto each impurity orbital including both spin orientations. The new IPR parameter is given by

$$
\text{IPR} = \left[\frac{\sum_m^N \left(\sum_\sigma |\langle \phi_{m\sigma} | \psi_i \rangle|^2 \right)^2}{\left(\sum_{m,\sigma}^N |\langle \phi_{m\sigma} | \psi_i \rangle|^2 \right)^2} \right]^{-1}. \tag{3.15}
$$

where $|\psi_i\rangle$ is the eigenstate whose localization degree is to be calculated. The states $|\phi_{m\sigma}\rangle$ are localized on site m and are assumed to be spin polarized. In Fig. 3.4 we present the DOS and IPR/N of the extended model for the three densities previously treated and various values of the spin-orbit coupling strength R_r. The DOS depicted with solid thick lines do not change noticeably with R_r, and that is why we only present the $R_r = 1$ case. Regarding the spatial extension, we show in each panel (for each density) how the IPR/N curves are modified as R_r changes. The increase of the IPR/N as a function of R_r in the region of extended states (central region) shows that the SOC tends to delocalize more and more these states as the IPR/N values grow towards 1.
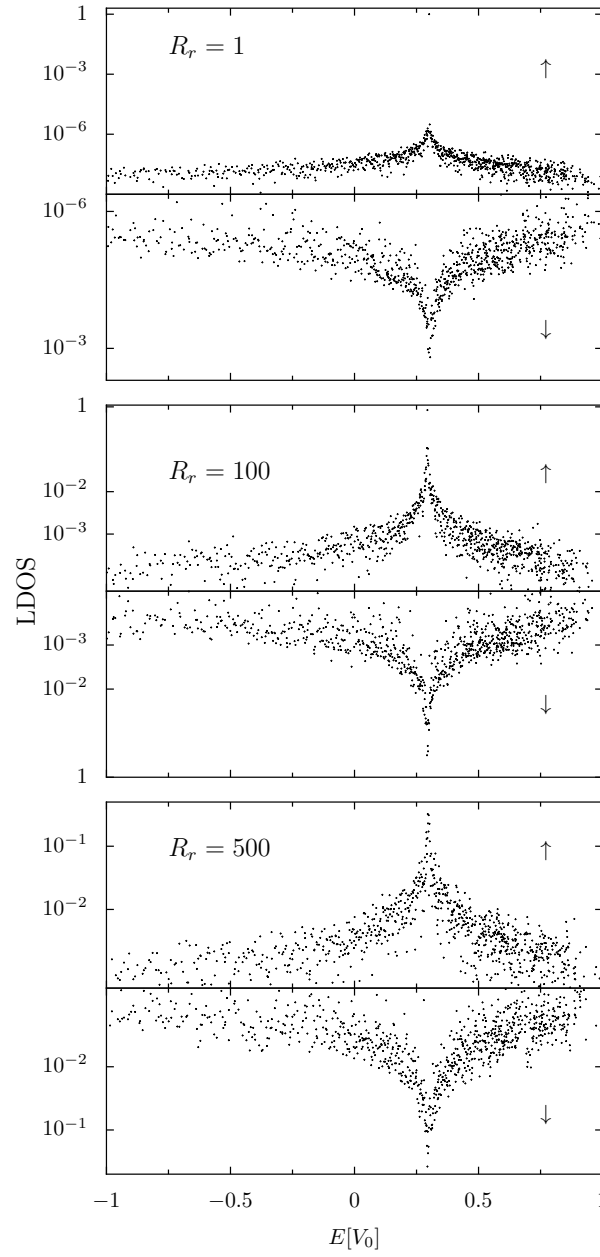
Figure 3.3: Spectral decomposition of a Matsubara-Toyozawa eigenstate into the basis set formed by the eigenstates of the spin-orbit extended model. The system size is $N = 1000$ and the density is given by $(n_i a^3)^{1/3} = 0.33$. The enhancement factor R_r is indicated in each panel.

This effect turns out to be even more pronounced for the larger density, where the curves belonging to different R_r's separate in a wider region. This latter effect becomes less prominent as the energy decreases. In the low-energy sector, where the MT model yields states identified as localized, we observe IPR/N curves approximately independent of N, which is a signature that the SOC is favouring their delocalization.

Finally, we also performed a finite-size scaling of the IPR/N for a given density above the MIT critical density and one value of the spin-orbit coupling enhancement factor, namely $R_r = 50$. The result in Fig 3.5 evinces that the relative insensitivity of IPR/N with N implies that the region of localized states (with vanishing IPR/N) has been considerably shifted towards a lower energy. We thus expect to have a lower mobility edge.

3.5 Conclusion

To sum up, we have considered the problem of the characterization of the eigenstates of the Matsubara-Toyozawa model regarding their spatial localization. We find that the obtained IPR values among the different eigenstates of the impurity band differ qualitatively from those given by a more thoroughly studied Anderson model. One reason for this is that we consider here a long-range potential that stems from the Coulombic impurity. Anderson models mostly deal with short-range potentials. In our physical system, the mobility edges do not appear as clear-cut limits, yet we observe a trend in the degree of localization of the eigenstates.

When a similar analysis is performed in the extended model including the spin-admixed nature of the donor states originated by the spin-orbit coupling, we have to take into account the spin-flip event caused by the electrostatic potential of the hydrogenic impurities (that in spite of being spin-independent, couples states of different spin). We found that while the density of states is not considerably modified by the spin-orbit interaction, the states tend to be more delocalized as the SOC gets stronger.
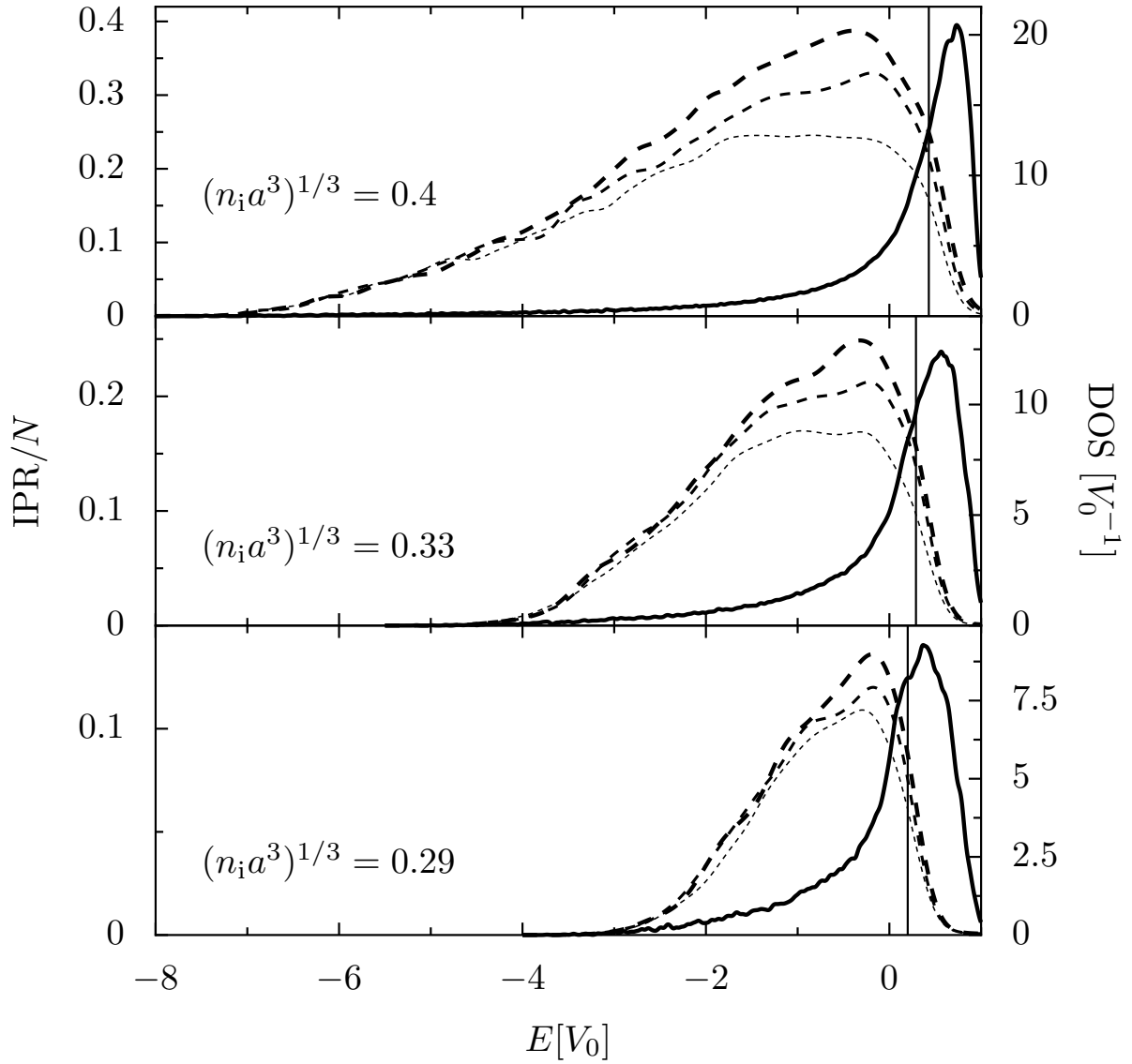
Figure 3.4: Density of states (DOS, solid line and right scale) and inverse participation ratio (IPR, dashed lines and left scale) for three different densities on the metallic side of the metal-insulator transition. Dashed lines with increasing thickness are for $R_r = 50$, 150 and 250, respectively. The vertical lines indicate the Fermi energy.
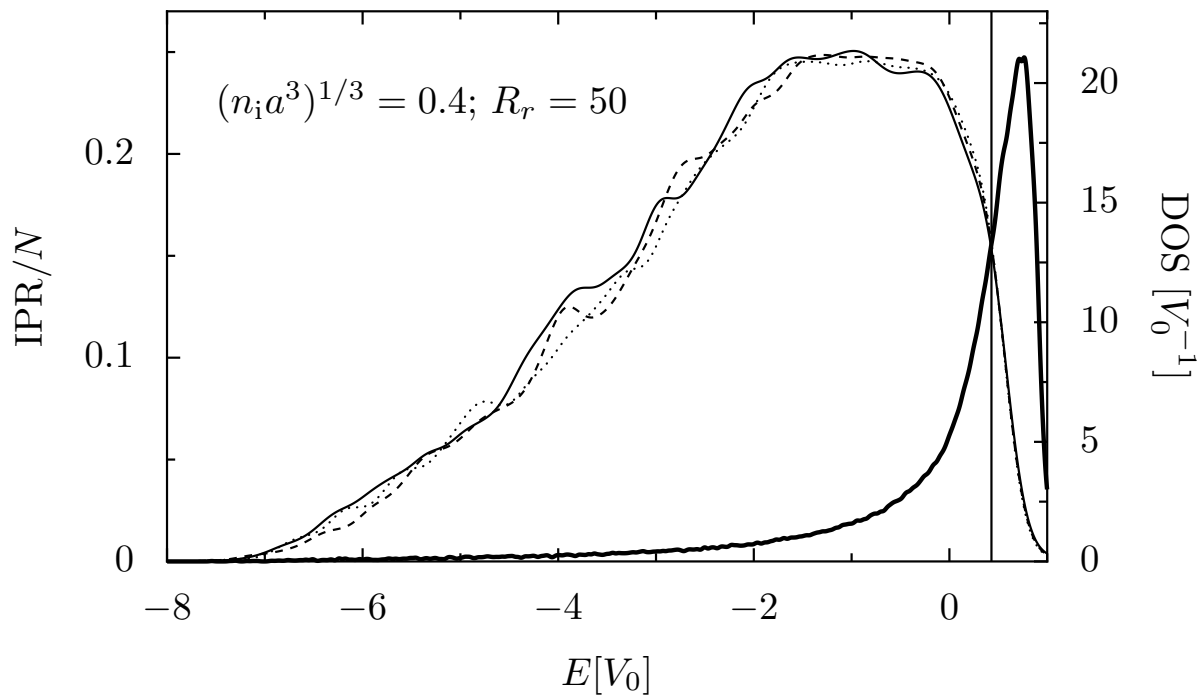
Figure 3.5: Density of states (DOS, thick line and right scale) and inverse participation ratio (IPR, left scale) for a density on the metallic side of the metal-insulator transition, three different system sizes, and a fixed spin-orbit enhancement factor of $R_r = 50$. The solid, dashed and dotted curves of IPR/N are for $N = 2744, 3375$ and 4096, respectively, and the vertical line indicates the Fermi energy.

Chapter 4

Spin-relaxation in the impurity band

In the previous chapter we studied the effects of the extrinsic-type SOC in the eigenstates of the impurity band. In what follows, we concentrate on the spin-relaxation driven by spin-orbit coupling in n-doped semiconductors, considering again a GaAs system in its zincblende phase. The tight-binding model of impurities including spin-orbit coupling due to the electrostatic impurity potentials, developed in Ref. [79], results in spin relaxation times much larger than the experimental values, suggesting that other mechanisms should be active in this density range. We include in this chapter the Dresselhaus term, and we unambiguously identify it as the source of the dominant spin-relaxation mechanism in the impurity band of a wide class of n-doped zincblende semiconductors. We conceive two complementary approaches. The first of them comprises an analytical diffusive time-evolution of the spin vector, while the second method treats the problem numerically and is based on a finite-size scaling study of the spin-relaxation time. The Dresselhaus hopping terms are derived and incorporated into an effective tight-binding model of impurity sites, and they are shown to unexpectedly dominate the spin relaxation, leading to spin-relaxation times in good agreement with experimental values.

4.1 Presentation

As we mentioned in the Introduction, a theoretical understanding of the spin-relaxation close to the MIT was still lacking before we undertook this work, in spite of some earlier attempts to identify the relevant mechanisms [33,79,97–99] in this regime. In particular, in Ref. [97], Shklovskii proposed the applicability of the well-known Dyakonov-Perel mechanism, usually valid in the conduction band, on the metallic side of the transition. Moreover, he considered the same spin-relaxation mechanism for the variable range hopping conductivity, which describes the conductivity in strong disorder systems at low temperatures. In this particular regime, the conductivity results from the electron hopps from one localized site to another one. This mechanism is therefore valid for density values below the critical one. As we emphasized before, the DP mechanism is based on the scattering of free electrons due to charged impurities. However, in the regime we are interested in, the electronic states are built from the impurity states, and hence, no scattering brought about by impurities is possible. Shklovskii's approach does not lead to a direct quantitative comparison with the experiment.

Our study starts with the construction of an effective spin-orbit Hamiltonian for the impurity system (an EFA Hamiltonian) and continues with an analytical and a numerical solution for the time evolution of a single spin in a random lattice. The resulting spin-relaxation times are in good agreement with the existing experimental values for GaAs and CdTe.

4.1.1 Temperature effects

Before addressing the description of our model and the obtained results, we consider the influence of the temperature on the spin-relaxation. The reason for this is that our theory does not include any temperature effect, whereby a justification is worth.

The influence of the temperature in the electron-spin relaxation has been thoroughly examined for various GaAs samples in Ref. [30] by Römer and collaborators, using a spin-noise technique. For high temperatures, as it was already known, the electrons become

delocalized and the spin dynamics can be described by the spin Bloch equations. This is also the situation when the density is well above the critical value. Here the conduction band is populated even at very low temperatures because the impurity band and the conduction band hybridize. The Fermi level is *in* the conduction band, and the spin-relaxation mechanism is understood in terms of the Dyakonov-Perel mechanism, the impurity scattering being the main electron-scattering phenomena.

On the other extreme, where the donors are far away from each other, the dominant mechanism is the hyperfine interaction with nuclear spins. A more doped sample ($n_d = 2.7 \times 10^{15} cm^{-3}$), but still below the MIT, is also studied in their experiment. In this case, the τ_s scarcely varies up to $20K$, which is consistent with the exchange interaction between the donor electrons. A decrease in τ_s is then observed for temperatures higher than $30K$, where the ionization of the donor levels starts being effective. The DP mechanism overcomes at this point the hyperfine interaction, whose efficiency decreases due to the interaction of the localized and the free electrons.

The last sample analyzed in Ref. [30] had a doping density right at the MIT. Although it led to a relaxation time of 267 ns, which is higher than the one reported in Ref. [26], they were able to confirm the longest spin-relaxation time for this sample at very low temperatures $\sim 4K$ and extend it up to $10K$. The spin-relaxation time remains approximately constant in between, and decreases above it. At $70K$, its value gets even smaller than that of the most doped sample. In fact, by measuring the conductivity they found that it followed a hopping transport formula governed by an exponential term, instead of the usual metallic behaviour. They then claimed that the temperature dependence of the spin relaxation in the hopping regime depends on the conductivity and would be described by the same exponential law. This hopping transport for such a density was shown to be valid for temperatures below 60 K.

The authors attempted to explain their results in this hopping regime appealing to two spin relaxation mechanism: the DP-like mechanism put forth by Shklovskii [97] that we have already discussed, and an anisotropic spin-exchange interaction found in Ref. [100] and [101]. For the latter, the estimation for the spin relaxation yielded consistent values

with the experimental result.

The convincing conclusion they drew was that the DP mechanism applies at high temperatures for all samples. Below $10\,$K and doping concentrations lower than n_c, τ_s is independent of temperature, because the electrons are localized. Up to the MIT, the hopping regime explains well the conductivity behaviour and the spin relaxation temperature dependence. The inelastic processes, as scattering due to phonons, on the other hand, are irrelevant at low temperatures anyway. According to this report, the longest spin-relaxation time occurs at the MIT. On the other hand, their evidence on the temperature-independent spin-relaxation over a region of low temperatures is what allows us to work within a zero-temperature formalism. We shall now present how we tackle the problem for spin-relaxation on the metallic side of the MIT.

4.1.2 Description of the model

The envelope-function approximation (EFA) for describing conduction-band electrons in zincblende semiconductors incorporates the lattice-scale physics (described by the periodic part of the Bloch wave function) into the effective one-body Hamiltonian [76,77]. As we saw in Chap.3, the resulting Hamiltonian operator comprises three terms

$$H = H_0 + H_{\text{extr}} + H_{\text{D}} \tag{4.1}$$

The first term represents the kinetic energy plus the potential of the impurities V:

$$H_0 = \frac{p^2}{2\,m^*} + V(\mathbf{r}), \tag{4.2}$$

the effective extrinsic term related to the effect of the impurities

$$H_{\text{extr}} = \lambda^* \boldsymbol{\sigma} \cdot \nabla V \times \mathbf{k} \tag{4.3}$$

and the Dresselhaus or BIA-driven spin-orbit coupling given by

$$H_{\text{D}} = \gamma \left[\sigma_x k_x (k_y^2 - k_z^2) + \text{cyclic permutations} \right]. \tag{4.4}$$

Here $\boldsymbol{\sigma}$ is the vector of Pauli matrices and $\mathbf{k} = \mathbf{p}/\hbar$ is the momentum operator in the absence of any magnetic field, and is therefore taken as the gradient (times $-i$).

The extrinsic term stems from $V(\mathbf{r})$ which includes all potentials aside from the crystal one. The effective spin-orbit coupling λ^* is usually orders of magnitude larger than the one of vacuum, and when calculated within the 8-band Kane model, for GaAs it yields $\lambda^* \simeq -5.3\,\text{Å}^2$ [77]. We include here the extrinsic term in eq. (4.3) as an equivalent approach as considering the Impurity Spin-Admixture model introduced in the previous chapter, as we will see. The potential $V(\mathbf{r})$ due to the ionized impurities is given by

$$V(\mathbf{r}) = \sum_p V_p(\mathbf{r}) = -\sum_p \frac{\mathrm{e}^2}{\epsilon|\mathbf{r} - \mathbf{R}_p|}, \tag{4.5}$$

where ϵ is the dielectric constant of the semiconductor and $\mathbf{R}_p$ represents the impurity positions. The potential of a single impurity V_p gives rise to the hydrogenic states centered at the impurity p. In order to build the basis of electronic states we only consider the ground state $\phi_p(\mathbf{r}) = \phi(|\mathbf{r} - \mathbf{R}_p|)$, with $\phi(\mathbf{r}) = (1/\sqrt{\pi a^3})\exp(-r/a)$, and a the effective Bohr radius.

In second-quantized form, the total Hamiltonian (4.1), reads

$$\mathcal{H}_0 = \sum_{m \neq m',\sigma} \langle m'\sigma|H_0|m\sigma\rangle \, c_{m'\sigma}^\dagger \, c_{m\sigma}, \tag{4.6}$$

$$\mathcal{H}_{\mathrm{SO}} = \sum_{m \neq m',\sigma} \langle m'\overline{\sigma}|H_{\mathrm{SO}}|m\sigma\rangle \, c_{m'\overline{\sigma}}^\dagger \, c_{m\sigma}, \tag{4.7}$$

where the label SO stands for "extr" or "D", and $\overline{\sigma} = -\sigma$.

4.1.3 Extrinsic Term matrix elements

The impurity potential given in eq. (4.5) may be regarded as an external potential producing a structural inversion asymmetry (or Rashba-like) spin-orbit coupling through eq. (4.3), and which we have been referring to as "extrinsic" along this thesis. In order to construct a tight-binding Hamiltonian including this SOC, we will now compute the matrix elements of H_{ext} between the $1s$ states of two different impurities. As we will see,

the final expression turns out to be equal to the one we found previously in the Impurity Spin-Admixture theory. The spin-flip hopping amplitudes complement the non-spin-flip hopping amplitudes of the Matsubara-Toyozawa model.

Let us first expand H_{ext}:

$$
\begin{aligned}
H_{\text{ext}} = {} & \lambda^* \left[\sigma_x \left(\frac{\partial V}{\partial y} k_z - \frac{\partial V}{\partial z} k_y \right) - \sigma_y \left(\frac{\partial V}{\partial x} k_z - \frac{\partial V}{\partial z} k_x \right) \right. \\
& \left. + \sigma_z \left(\frac{\partial V}{\partial x} k_y - \frac{\partial V}{\partial y} k_x \right) \right].
\end{aligned}
\tag{4.8}
$$

With the notation $\overline{\sigma} = -\sigma$, we obtain that $\langle \overline{\sigma} | \sigma_x | \sigma \rangle = 1$ and $\langle \overline{\sigma} | \sigma_y | \sigma \rangle = i\sigma$. Using these relations, the spin-flip hopping matrix element for the Hamiltonian in eq. (4.8) between impurities m and m' becomes

$$
\langle m' \overline{\sigma} | H_{\text{ext}} | m \sigma \rangle = \lambda^* \left(\langle m' | \frac{\partial V}{\partial y} k_z - \frac{\partial V}{\partial z} k_y | m \rangle - i\sigma \langle m' | \frac{\partial V}{\partial x} k_z - \frac{\partial V}{\partial z} k_x | m \rangle \right).
\tag{4.9}
$$

where $|m\sigma\rangle$ denotes a $1s$ state ($\phi_m(\mathbf{r}) = \langle \mathbf{r} | m \rangle$) with spin σ at an impurity located at $\mathbf{R}_m$. Carrying out an integration by parts and regrouping terms we obtain (see Appendix I for a derivation)

$$
\begin{aligned}
\langle m' \overline{\sigma} | H_{\text{ext}} | m \sigma \rangle = {} & \frac{\sigma \lambda^*}{a^2} \int d\mathbf{r} \, V(\mathbf{r}) \frac{\phi_{m'}(\mathbf{r}) \, \phi_m(\mathbf{r})}{|\mathbf{r} - \mathbf{R}_{m'}| |\mathbf{r} - \mathbf{R}_m|} \\
& [(z - z_m)(r_\sigma - R_{m'\sigma}) - (z - z_{m'})(r_\sigma - R_{m\sigma})],
\end{aligned}
\tag{4.10}
$$

where $r_\sigma = x + i\sigma y$ and $R_{m\sigma} = X_m + i\sigma Y_m$. This expression agrees with the matrix element in eq. (3.8) of the previous chapter, by replacing the impurity states by the corresponding $1s$ hydrogenic-like states and the impurity Coulomb potential. Of course, it also coincides with eq. (11) of Ref. [79], with a slight difference concerning r_σ that was overlooked in that reference. We recall that the term corresponding to $p = m'$ in $V(\mathbf{r})$ inside the integral (4.10) yields a vanishing contribution to the matrix element, due to the axial symmetry of the two-center integrals. Therefore, the remaining matrix elements are given by three-center integrals, resulting in very slow spin relaxation in

comparison with experimental results, as noted in [79]. We will come back to this later on this chapter.

In next section we make a similar calculation for the matrix elements coming from the Dresselhaus SOC. The typical matrix elements are presented and compared to these three-center integrals we have encountered in this section.

4.1.4 The Dresselhaus matrix elements

We now treat the Dresselhaus spin-flip hopping matrix elements between $1s$ eigenstates of donor impurities. The effective Dresselhaus Hamiltonian for the conduction band of zincblende semiconductors is cubic in the wave vector and is given by

$$H_D = \gamma[\sigma_x k_x(k_y^2 - k_z^2) + \text{c.p.}] \tag{4.11}$$

where γ is a material-dependent constant, and c.p. stands for cyclic permutations of x, y, and z. In order to calculate the matrix element between two sites, we consider as before two impurities located at $\mathbf{R}_m$ and $\mathbf{R}_n$, with $1s$ states ($\phi(|\mathbf{r} - \mathbf{R}_m|) = (1/\sqrt{\pi a^3}) \exp(|\mathbf{r} - \mathbf{R}_m|/a)$, with opposite spin, denoted as $|m\sigma\rangle$ and $|n\bar{\sigma}\rangle$. The matrix element between these states is

$$
\begin{aligned}
\langle n\bar{\sigma}|H_D|m\sigma\rangle &= \gamma[\langle n\bar{\sigma}|\sigma_x k_x(k_y^2 - k_z^2)|m\sigma\rangle + \langle n\bar{\sigma}|\sigma_y k_y(k_z^2 - k_x^2)|m\sigma\rangle] \\
&= \gamma[\langle n|k_x(k_y^2 - k_z^2)|m\rangle + i\,\text{sgn}(\sigma)\langle n|k_y(k_z^2 - k_x^2)|m\rangle],
\end{aligned} \tag{4.12}
$$

where the spin dependence was readily obtained using $\langle \bar{\sigma}|\sigma_x|\sigma\rangle = 1$, and $\langle \bar{\sigma}|\sigma_y|\sigma\rangle = i\,\text{sgn}(\sigma)$. For the orbital part, as the EFA formalism indicates, we replace $k_x = -i\partial/\partial x$, and analogously for k_y and k_z. Thus, by performing integration by parts once, we obtain

$$
\begin{aligned}
\langle n|k_x(k_y^2 - k_z^2)|m\rangle &= \frac{i}{a^2} \int d\mathbf{r} \, \frac{\phi_n(\mathbf{r})\,\phi_m(\mathbf{r})}{|\mathbf{r} - \mathbf{R}_n||\mathbf{r} - \mathbf{R}_m|^2}(x - x_n)[(y - y_m)^2 - (z - z_m)^2] \\
&\qquad \left[\frac{1}{a} + \frac{1}{|\mathbf{r} - \mathbf{R}_m|}\right],
\end{aligned} \tag{4.13}
$$

115

while for the second term in eq. (4.12) we obtain an analogous expression

$$
\begin{aligned}
\langle n|k_y(k_z^2 - k_x^2)|m\rangle \;=\;& \frac{i}{a^2} \int d\mathbf{r} \, \frac{\phi_n(\mathbf{r})\,\phi_m(\mathbf{r})}{|\mathbf{r}-\mathbf{R}_n||\mathbf{r}-\mathbf{R}_m|^2}(y - y_n) \\
& \cdot [(x-x_m)^2 - (z-z_m)^2]\left[\frac{1}{a} + \frac{1}{|\mathbf{r}-\mathbf{R}_m|}\right].
\end{aligned}
\qquad (4.14)
$$

Changing to coordinates $\mathbf{r} \to \mathbf{r} - \mathbf{R}_m$ and introducing $\mathbf{R}_{nm} \equiv \mathbf{R}_n - \mathbf{R}_m$ we get

$$
\begin{aligned}
\langle n\bar{\sigma}|H_D|m\sigma\rangle \;=\;& \frac{\gamma}{a^3} \int d\mathbf{r} \, \frac{\phi(|\mathbf{r}-\mathbf{R}_{nm}|)\,\phi(r)}{|\mathbf{r}-\mathbf{R}_{nm}|\,r^3}(a+r) \\
& \cdot [\mathrm{sgn}(\sigma)(y - y_{nm})(x^2 - z^2) + i\,(x - x_{nm})(y^2 - z^2)].
\end{aligned}
\qquad (4.15)
$$

Using the form of the $1s$ wave functions and expressing all distances within the integral in units of a we get

$$
\begin{aligned}
\langle n\bar{\sigma}|H_D|m\sigma\rangle \;=\;& \frac{\gamma}{\pi a^3} \int d\mathbf{r} \, \frac{\mathrm{e}^{-|\mathbf{r}-\mathbf{R}_{nm}|}\,\mathrm{e}^{-r}}{|\mathbf{r}-\mathbf{R}_{nm}|\,r^3}(1+r)[\mathrm{sgn}(\sigma)(y - y_{nm})(x^2 - z^2) \\
& +i\,(x - x_{nm})(y^2 - z^2)] \\
\equiv\;& \frac{\gamma}{\pi a^3}\left[\mathrm{sgn}(\sigma)\,I_{y,nm} + i\,I_{x,nm}\right],
\end{aligned}
\qquad (4.16)
$$

where we have defined the integrals $I_{y,nm}$ and $I_{x,nm}$ in an obvious way. We now perform a rotation of the coordinate system and then switch to cylindrical coordinates in order to perform analytically one (the angular) integral. We further use that $\mathbf{R}_{nm} = R_0(\sin\theta\cos\varphi, \sin\theta\sin\varphi, \cos\theta)$ and rotate the axis by the angles φ and θ so that the vector $\mathbf{R}_{nm}$ in the new system is given by $(0, 0, R_0)$. Since $I_{y,nm}$ has the same value as $I_{x,nm}$, provided x_{nm} and y_{nm} are interchanged, we evaluate hereafter only $I_{x,nm}$, which

in the rotated coordinate system is

$$
\begin{aligned}
I_{x,nm} &= \int d\mathbf{r}\, \frac{e^{-\sqrt{x^2+y^2+(z-R_0)^2}}\, e^{-r}}{\sqrt{x^2+y^2+(z-R_0)^2}\, r^3}(1+r) \\
&\quad \cdot (x\cos\theta\cos\varphi - y\sin\varphi + z\sin\theta\cos\varphi - R_0\sin\theta\cos\varphi) \\
&\quad \cdot [(x\cos\theta\sin\varphi + y\cos\varphi + z\sin\theta\sin\varphi)^2 - (-x\sin\theta + z\cos\theta)^2]. \quad (4.17)
\end{aligned}
$$

We switch to cylindrical coordinates $(x,y,z) = (\rho\cos\alpha, \rho\sin\alpha, z)$ and obtain:

$$
\begin{aligned}
I_{x,nm} &= \int d\rho\, dz\, \rho\, \frac{e^{-\sqrt{\rho^2+(z-R_0)^2}}\, e^{-\sqrt{\rho^2+z^2}}}{\sqrt{\rho^2+(z-R_0)^2}\,(\rho^2+z^2)^{3/2}}(1+\sqrt{\rho^2+z^2}) \\
&\quad \cdot \int d\alpha\, [\rho\cos\alpha\cos\theta\cos\varphi - \rho\sin\alpha\sin\varphi + (z-R_0)\sin\theta\cos\varphi] \\
&\quad \cdot [\, (\rho\cos\alpha\cos\theta\sin\varphi + \rho\sin\alpha\cos\varphi + z\sin\theta\sin\varphi)^2 \\
&\quad -(-\rho\cos\alpha\sin\theta + z\cos\theta)^2\,]. \quad (4.18)
\end{aligned}
$$

After performing the integral over α we obtain

$$
\begin{aligned}
I_{x,nm} &= \pi \int d\rho\, dz\, \rho\, \frac{e^{-\sqrt{\rho^2+(z-R_0)^2}}\, e^{-\sqrt{\rho^2+z^2}}}{\sqrt{\rho^2+(z-R_0)^2}\,(\rho^2+z^2)^{3/2}}(1+\sqrt{\rho^2+z^2}) \\
&\quad \times\; [c_1\,\rho^2 z + c_2\,\rho^2(z-R_0) + c_3\,z^2(z-R_0)] \quad (4.19)
\end{aligned}
$$

where

$$
\begin{aligned}
c_1 &= 2\sin\theta\cos^2\theta\cos\varphi\,(1+\sin^2\varphi) - 2\sin\theta\sin^2\varphi\cos\varphi, \\
c_2 &= \sin\theta\cos^2\theta\sin^2\varphi\cos\varphi - \sin^3\theta\cos\varphi + \sin\theta\cos^3\varphi, \\
c_3 &= 2\sin^3\theta\sin^2\varphi\cos\varphi - 2\sin\theta\cos^2\theta\cos\varphi. \quad (4.20)
\end{aligned}
$$

The integral $I_{y,nm}$ for the same geometry is obtained by evaluating $I_{x,nm}$ with $\varphi \to \frac{\pi}{2} - \varphi$.

The material dependence appears only in the prefactor in eq. (4.16), which depends on the Dresselhaus constant and the effective Bohr radius.

Concerning the parameters c's in eq. (4.20), it can be easily proved that the coefficients satisfy $c_1/2 = c_2$ and $c_3 = -c_1$. A more simplified formula is then obtained for the integral

$$
\begin{aligned}
I_{x,nm} &= \pi c \int d\rho \, dz \, \rho \, \frac{e^{-\sqrt{\rho^2+(z-R_0)^2}} \, e^{-\sqrt{\rho^2+z^2}}}{\sqrt{\rho^2+(z-R_0)^2} \, (\rho^2+z^2)^{3/2}} (1+\sqrt{\rho^2+z^2}) \\
&\quad \cdot \left[\frac{\rho^2}{2}(3z-R_0) - z^2(z-R_0) \right]
\end{aligned}
$$
(4.21)

where $c = c_1$. To further simplify the form of the integrals, we can now make a rigid shift in the z-direction, such that $z \to z' + R_0/2$ and rescale all distances with $R_0/2$. In the resulting integral, we make use of prolate spheroidal coordinates (η, ξ, ϕ), defined by

$$
\begin{aligned}
x &= (R_0/2) \, \sinh(\xi) \sin(\eta) \cos(\phi) \\
y &= (R_0/2) \, \sinh(\xi) \sin(\eta) \sin(\phi) \\
z &= (R_0/2) \, \cosh(\xi) \cos(\eta)
\end{aligned}
$$
(4.22)

with $\xi \in [0, \infty)$, $\eta \in [0, \pi]$, and $\phi \in [0, 2\pi)$. Remarkably, with the help of these coordinates, we have been able to preform the integral which leads to the simple expression

$$
I_{x,m'm} = \frac{\pi c}{6} \left(\frac{R_0}{a} \right)^2 e^{-R_0/a},
$$
(4.23)

where $c = 2\cos\varphi \sin\theta \left[1 - \sin^2\theta \left(1 + \sin^2\varphi \right) \right] = c_1$ and R_0 is the distance between the impurities involved in the matrix element.

In Fig. 4.1, the typical Dresselhaus matrix elements for GaAs as a function of the distance between impurities are exposed. A comparison with the equivalent values in Fig. 3.2 is meaningful, since it clearly hints at the dominance of the Dresselhaus coupling over the extrinsic counterpart. In this figure we present results for GaAs, whose $\gamma = 27.58\,\mathrm{eV\,\mathring{A}}^3$ [69], and $a \simeq 99\,\mathring{A}$. Other ZB materials exhibit rather different parameters. For example, for InAs $\gamma = 27.18\,\mathrm{eV\,\mathring{A}}^3$, $a \simeq 337\,\mathring{A}$, and for InSb $\gamma = 760.1\,\mathrm{eV\,\mathring{A}}^3$, $a \simeq 681\,\mathring{A}$ [69]. It is interesting to note that, considering these parameters, the Dresselhaus matrix elements result larger for GaAs than for InAs or InSb, an unusual situation among the semiconductor spin-orbit effects.
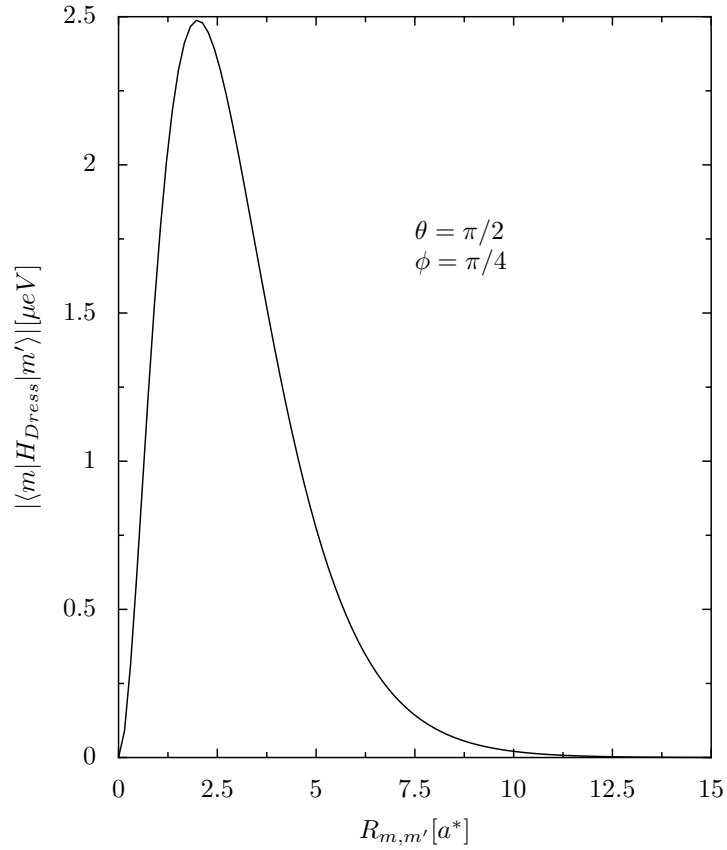
Figure 4.1: The absolute value of the Dresselhaus spin-orbit coupling is calculated for
GaAs for a fixed orientation of the impurities given by ϕ and θ. The x-axis
denotes the distance between the two impurities m and m' in units of the
effective Bohr radius a. The magnitude of these matrix elements are to be
compared to the values in Fig. 3.2.

So far we have shown the various elements that constitute the model we use to describe our system. We still have not explained how we study the spin dynamics in the impurity band. This is the subject of next section.

4.2 Diffusion on the Bloch sphere

The probability of a spin-flip at a hop given by the transition matrix elements, either by Dresselhaus or by extrinsic SOC, is much smaller than the probability of keeping the spin unchanged during the hop. Therefore, we need a scheme to account for the fact that the electron undergoes a spatial diffusion through the network of impurities, that is accompanied by a small spin-rotation angle at each hop. To combine these two processes, we introduce the Bloch sphere, a concept usually employed whenever the dynamics of a spin vector is analyzed. It appears typically in Rabi oscillations where a spin, under the influence of an external magnetic field, is studied. It turns out that if this magnetic field is conveniently set, a complete spin flip is possible. In our case, we start with an electron in an eigenstate of the MT Hamiltonian, i.e. a state with a definite spin, say, along the z-direction. Due to the perturbation produced by the spin-orbit coupling, this state evolves, and the spin direction rotates a small angle at each hop. The path stroked by the spin vector on the Bloch sphere is like a random walk, with very short steps (angles) along the surface of the sphere. Equivalently, the tip of the vector is a moving point on the sphere, and it is equally probable that it makes an angular displacement α in any direction. Hence, the goal is to find the distribution of this tip after a (asymptotically) large number of infinitesimal steps. This random behaviour yields a variance of the angle in the in-plane motion equal to

$$V_{ar} = \sum_{i=1}^{N} \alpha_i^2$$

where N is the total number of steps and α_i the infinitesimal displacement at the i-th step. If we assume second moments $\langle \alpha_i^2 \rangle = \langle \alpha^2 \rangle$, this result translates into

$$V_{ar} = N \langle \alpha^2 \rangle$$

In the specific case we treat here, the rotation of a vector occurring around each of the three x, y, z axis is taken into account. This implies that we have a spin rotation angle θ for each component, and we shall sum over all of them

$$\langle \theta^2 \rangle = \langle \theta_x^2 \rangle + \langle \theta_y^2 \rangle + \langle \theta_z^2 \rangle$$

However, for an isotropic problem where $\langle \theta_x^2 \rangle = \langle \theta_y^2 \rangle = \langle \theta_z^2 \rangle$ we obtain

$$\langle \theta^2 \rangle = 3 \langle \theta_x^2 \rangle$$

If we further choose to assign the initial direction at *every* step to be along z-direction, then the variance associated to the small rotation angle α means for us

$$\langle \alpha^2 \rangle = \langle \theta_x^2 \rangle + \langle \theta_y^2 \rangle$$

from which we conclude that

$$\langle \alpha^2 \rangle = \frac{2}{3} \langle \theta^2 \rangle$$

and therefore, the expression for the angle variance yields

$$V_{ar} = N \frac{2}{3} \langle \theta^2 \rangle \tag{4.24}$$

We have begun with this quantity because the time-dependent probability distribution $\rho(t)$ we need to calculate the spin behaviour, is given in terms of it. To show this, we rely on the formulation of Ref. [102], to be described now. In this Reference, the random walk of a moving point on a sphere is considered. The succession of random steps is equally probable for all directions from the starting point. Let us suppose that an initial probability distribution is given for a certain point r_0 on the sphere. A sequence of displacements brings this initial point to other points $r_1, r_2...$ on the sphere, each step having an displacement characterized by an angular distance, and equally probable to

any direction. The solution we need is the probability distribution of these points as a function of time. We take the length of the step -a rotation angle- to be constant.

Let us take an initial distribution at time $t = 0$ given by

$$\rho_0 = \sum_{n=0}^{\infty} \frac{2n+1}{4\pi} P_n(\cos\theta) \tag{4.25}$$

with P_n the Legendre Polynomial of order n and θ the angle with respect to the starting axis. As stated in Ref. [102], at a time t later, the same distribution will have evolved to

$$\rho(t) = \sum_{n=0}^{\infty} \frac{2n+1}{4\pi} e^{-\frac{1}{4}n(n+1)V_{ar}(t)} P_n(\cos\theta) \tag{4.26}$$

We note that the variance appears in the exponential and it bears the time dependence. Since we are interested in the evolution of the S_z operator, we project this distribution on the z-axis by multiplying it by $\cos(\theta)$ and calculate the spin expectation value by integrating over the angles as

$$\langle\sigma_z(t)\rangle = \int_0^\pi d\theta \sin(\theta) \int_0^{2\pi} d\phi \, \cos(\theta)\rho(t) \tag{4.27}$$

$$= 2\pi \int_0^\pi d\theta \cos(\theta)\sin(\theta)\rho(t) \tag{4.28}$$

Recalling that $\rho(t)$ only depends on $\cos(\theta)$, the substitution $u = \cos(\theta)$ is convenient. Furthermore, if we insert the expression of eq. (4.26) in (4.28), we are left with

$$\langle\sigma_z(t)\rangle = 2\pi \int_{-1}^{1} du \, u \sum_{n=0}^{\infty} \frac{2n+1}{4\pi} e^{-\frac{1}{4}n(n+1)V(t)} P_n(u) \tag{4.29}$$

$$= \frac{1}{2} \sum_{n=0}^{\infty} (2n+1) e^{-\frac{1}{4}n(n+1)V_{ar}(t)} \int_{-1}^{1} du P_1(u) P_n(u) \tag{4.30}$$

where the relation $P_1(u) = u$ has been used. The orthogonality relation over the integration region $[-1, 1]$ satisfied by the Legendre polynomials

$$\int_{-1}^{1} du \, P_m(u) \, P_n(u) = \frac{2}{2n+1} \delta_{nm}$$

brings the partial result of eq. (4.30) to

$$\langle \sigma_z(t) \rangle = e^{-\frac{1}{2} V_{ar}(t)}. \tag{4.31}$$

The variance V_{ar} contains the total number of steps N after a time t, and so we can easily estimate it as

$$N = \frac{t}{\tau_c}. \tag{4.32}$$

Here we introduced a new time scale given by τ_c, which is the mean time between hops and we name it *mean-hopping time* accordingly. In combination with our expression for the variance, we get

$$\langle \sigma_z(t) \rangle = \exp \left(-\frac{1}{3} \frac{\langle \theta^2 \rangle}{\tau_c} t \right) = \exp \left(-\frac{t}{\tau_s} \right) \tag{4.33}$$

The spin-relaxation time τ_s in the exponential has been defined through

$$\frac{1}{\tau_s} = \frac{\langle \theta^2 \rangle}{3\tau_c}. \tag{4.34}$$

This is our sought result. The last equation indicates that τ_c and $\langle \theta^2 \rangle$ must be next calculated. Let us take care of the first of them and postpone the second for the next section.

The typical time between two hopping events is much smaller that the time scale associated to spin-relaxation, since the energy given by the MT hopping terms are larger than transfer energies coming from the spin-orbit coupling, either by the extrinsic or the Dresselhaus terms. The time τ_c can then be estimated from time-dependent perturbation

theory, regarded as the time needed for the initial-state population on an impurity site to drop from 1 to 1/2. In order to calculate such a time, let us notice first that it is mainly determined by the MT Hamiltonian, since we can disregard the small effect of the spin-flip terms. Next we assume that the initial state is a localized state at the impurity site labeled m. In Ref. [79], it is shown that a similar result is obtained if this initial state is extended. From perturbation theory, we know that for short times, the evolved state satisfies

$$|\Psi(t)\rangle = \left(1 - i\frac{\mathbf{H}}{\hbar}t\right)|m\rangle$$

which must be projected over the other impurities (excluding the site m) using the projection operator

$$P_m = \sum_{m'\neq m} |m'\rangle\langle m'|$$

Setting the probability at time $t = \tau_c$ equal to 1/2, then

$$P(\tau_c) = 0.5 = \left|\frac{\tau_c}{\hbar}\sum_{m'\neq m}|m'\rangle\langle m'|\mathbf{H}|m\rangle\right|^2$$

The final result for τ_c, including the spin value σ of the initial state, then reads

$$\frac{1}{\tau_c} = \frac{\sqrt{2}}{\hbar}\left(\sum_{m\neq m'}|\langle m'\sigma|H_0|m\sigma\rangle|^2\right)^{1/2} \tag{4.35}$$

where we only keep the non-flip matrix elements as the leading contribution to this spatial diffusion since they largely exceed the spin-flip terms. It must be noticed that τ_c is neither the correlation time appearing in the Dyakonov-Perel mechanism nor the momentum relaxation time. We come back to this equation when we perform the average over impurity configurations, in which case we convert the sum to an integral.

4.3 The small spin rotation angle

In the preceding section we have found that our analytical approach necessitates the calculation of the small spin rotation angle between two hops. The calculation of this small angle assumes that it occurs in a very short time, so that first order perturbation theory can be used. In this case we consider the initial general state to be a localized state centered at the impurity m_0 and with a general spin-orientation $\widehat{n}$ given by the angles θ_0 and ϕ_0.

$$|\Psi(t=0)\rangle = |m_0, \widehat{n}\rangle = \cos(\theta_0/2)|m_0 \uparrow\rangle + \sin(\theta_0/2)e^{i\phi_0}|m_0 \downarrow\rangle \tag{4.36}$$

As time evolves, the state changes according to the unitary time evolution operator, which when expanded for short times leads to

$$
\begin{aligned}
|\Psi(t)\rangle &= (1 - \frac{i\mathbf{H}t}{\hbar})|\Psi_0\rangle \\
&= |\Psi_0\rangle - \frac{i\mathbf{H}t}{\hbar}\left(\cos(\theta_0/2)|m_0 \uparrow\rangle + \sin(\theta_0/2)e^{i\phi_0}|m_0 \downarrow\rangle\right) \tag{4.37}
\end{aligned}
$$

To proceed, we insert the unity operator

$$\mathbb{I} = \sum_{m',\sigma} |m'\sigma\rangle\langle m'\sigma|$$

in order to make the Hamiltonian matrix elements appear. We then obtain

$$
\begin{aligned}
|\Psi(t)\rangle &= |\Psi_0\rangle - \frac{it}{\hbar}\cos(\theta_0/2)\sum_{m'}\left(|m' \downarrow\rangle t^{-+}_{m'm_0} + |m' \uparrow\rangle t^{++}_{m'm_0}\right) \\
&\quad + \left(-\frac{it}{\hbar}\right)\sin(\theta_0/2)e^{i\phi_0}\sum_{m'}\left(|m' \downarrow\rangle t^{--}_{m'm_0} + |m' \uparrow\rangle t^{+-}_{m'm_0}\right) \\
&= |\Psi_0\rangle - \frac{it}{\hbar}\left\{\sum_{m'}\left(\cos(\theta_0/2)t^{-+}_{m'm_0} + \sin(\theta_0/2)e^{i\phi_0}t^{--}_{m'm_0}\right)|m'\rangle\right\} \otimes |\downarrow\rangle \\
&\quad + \left(-\frac{it}{\hbar}\right)\left\{\sum_{m'}\left(\cos(\theta_0/2)t^{++}_{m'm_0} + \sin(\theta_0/2)e^{i\phi_0}t^{+-}_{m'm_0}\right)|m'\rangle\right\} \otimes |\uparrow\rangle.
\end{aligned}
$$

By writing Ψ_0 explicitly, we have

$$|\Psi(t)\rangle = \left\{ |m_0\rangle \sin(\theta_0/2)e^{i\phi_0} + \left(\frac{-it}{\hbar}\right) \sum_{m'} \left(\cos(\theta_0/2)t^{-+}_{m'm_0} + \sin(\theta_0/2)e^{i\phi_0}t^{--}_{m'm_0} \right) |m'\rangle \right\} \otimes |\downarrow\rangle$$

$$+ \left\{ |m_0\rangle \cos(\theta_0/2) + \left(-\frac{it}{\hbar}\right) \sum_{m'} \left(\cos(\theta_0/2)t^{++}_{m'm_0} + \sin(\theta_0/2)e^{i\phi_0}t^{+-}_{m'm_0} \right) |m'\rangle \right\} \otimes |\uparrow\rangle.$$

If we start with an initial up state, i.e. $\cos(\theta_0/2) = 1$ and $\sin(\theta_0/2) = 0$, the last equation is reduced to

$$|\Psi(t)\rangle = \frac{-it}{\hbar} \sum_{m'} t^{-+}_{m'm_0} |m'\rangle \otimes |\downarrow\rangle$$

$$+ \left\{ |m_0\rangle + \left(-\frac{it}{\hbar}\right) \sum_{m'} t^{++}_{m'm_0} |m'\rangle \right\} \otimes |\uparrow\rangle \tag{4.38}$$

where it can be readily recognized, that the state acquires a $\downarrow$ contribution owing to the SOC matrix elements. If we write instead a general evolved state in the impurity basis set as

$$|\Psi(t)\rangle = \sum_{m'} c_{m'} \left(\cos(\theta_{m'}/2)|m' \uparrow\rangle + \sin(\theta_{m'}/2)e^{i\phi_{m'}}|m' \downarrow\rangle \right)$$

and compare the two expressions

$$\frac{-it}{\hbar} t^{-+}_{m'm_0} = c_{m'} \sin(\theta_{m'}/2)e^{i\phi_{m'}} \tag{4.39}$$

$$\frac{-it}{\hbar} t^{++}_{m'm_0} = c_{m'} \cos(\theta_{m'}/2) \tag{4.40}$$

we get an expression for the angle $\theta_{m'}$, required for our spin diffusion scheme.

$$\frac{|t^{-+}_{m'm_0}|}{|t^{++}_{m'm_0}|} = tg(\theta_{m'}/2) \sim \frac{\theta_{m'}}{2}. \tag{4.41}$$

We have assumed that the spin rotation angle $\theta_{m'}$ is small, since the SOC is weak.

For the general case of an initial state with an arbitrary spin orientation given by (θ_0, ϕ_0) we find the following formula

$$\cos\left(\theta_{m'}; \{\theta_0, \phi_0\}\right) = 1 - \frac{2|t_{m'm_0}^{++}|^2[1 + \sin^2(\theta_0)\cos^2(\phi_0)]}{|t_{m'm_0}^{++}|^2 + |t_{m'm_0}^{-+}|^2 + 2\sin(2\theta_0)\cos(\phi_0)Re[(t_{m'm_0}^{++})^*(t_{m'm_0}^{-+})]}$$

which is reduced for small angles to

$$\theta_{m'}(\theta_0, \phi_0) = 2\sqrt{1 + \sin^2(\theta_0)\cos^2(\phi_0)}\frac{|t_{m'm_0}^{-+}|}{|t_{m'm_0}^{++}|}.$$

We now need to average over (θ_0, ϕ_0) in order to take into account all the possible initial angles, and obtain the typical angle of rotation. The result is

$$
\begin{aligned}
\langle\theta_{m'}^2\rangle &= \frac{1}{4\pi}\int_0^\pi d\theta_0\sin(\theta_0)\int_0^{2\pi}d\phi_0\,\theta_{m'}^2(\theta_0, \phi_0) \\
&= \frac{1}{4\pi}\int d\theta_0\,d\phi_0 4\left(1 + \sin^2(\theta_0)\cos^2(\phi_0)\right)\frac{|t_{m'm_0}^{-+}|^2}{|t_{m'm_0}^{++}|^2} \\
&= \frac{16}{3}\frac{|t_{m'm_0}^{-+}|^2}{|t_{m'm_0}^{++}|^2} \qquad\qquad (4.42)
\end{aligned}
$$

where the 4π in the denominator accounts for the normalization of the initial angles. This formula thus gives the typical rotation angle -in terms of its variance- for an electron jumping from impurity m_0 to impurity m', no matter the initial orientation of the spin.

An ensemble average must still be done, taking into account the fact that there is a certain (homogeneous) distribution probability for the position between the impurities, and therefore, many configurations of disorder have to be considered.

4.4 An analytical expression for the spin-relaxation time

We now undertake the last stage of the calculation towards a formula of the spin-relaxation rate. In the sequel, we complete the calculation by performing the ensemble average explicitly and we arrive to an analytical expression for the spin-relaxation time, free of adjustable parameters. We complete the analysis with an alternative numerical approach afterwards.

In the next two subsections we take care of the impurity averages for the hopping time and for the typical rotation angle separately.

Mean-hopping time

We start by making the impurity average for the calculation of the mean-hopping time in eq. (4.35). We note that the formula for τ_c involves a sum over all the impurities, and so we convert this sum into a integral assuming a uniform distribution for the impurities positions, weighted by a doping density n_i. We take a random distribution for the impurity positions without hard-core repulsive effects on the scale of the effective Bohr radius [79, 103].

Let us first make a little digression about the *ensemble average*. An average over impurity configurations involves indeed a sum over different configurations and a sum over every impurity position in *each* realization. Such an average would read

$$\overline{f}(\vec{R}^c_{m\,m_0}) = \frac{1}{N_c} \sum_c \sum_{m\neq m_0} f(\vec{R}^c_{m\,m_0})$$

where c tags the realization, m labels the impurity and N_c is the number of realizations. The function $f(\vec{R}^c_{m\,m_0})$ is any function that depends on the distance between the impurities m and m_0. The same expression may be written as an integral in the following way

$$\frac{1}{N_c} \sum_c \int d^3\vec{R} \ f(\vec{R}) \sum_{m \neq m_0} \delta(\vec{R} - \vec{R}^{(c)}_{m\,m_0}) = \int d^3\vec{R} f(\vec{R}) \frac{1}{N_c} \sum_c \sum_{m \neq m_0} \delta(\vec{R} - \vec{R}^{(c)}_{m\,m_0})$$

$$= \int d^3\vec{R} f(\vec{R}) \left(\frac{1}{N_c} \sum_c \sum_m \delta(\vec{R} - \vec{R}^{(c)}_{m\,m_0}) - \frac{1}{N_c} \sum_c \delta(\vec{R}) \right). (4.43)$$

If we further consider an homogeneous independent impurity distribution, we have that

$$\frac{1}{N_c} \sum_c \sum_m \delta(\vec{R} - \vec{R}^{(c)}_{m\,m_0}) = n_i$$

where the impurity density n_i has been introduced. In eq. (4.43), the second term within the brackets yields no contribution, and so the final result is

$$\frac{1}{N_c} \sum_c \sum_m f(\vec{R}^c_{m\,m_0}) = \int d^3\vec{R} f(\vec{R}) \, n_i = 4\pi \int dR R^2 f(R) \, n_i. \qquad (4.44)$$

The second equality holds as long as the function depends only on the distance between impurities and not on their relative position. As we see in eq. (4.44), the probability of finding an impurity in an infinitesimal volume around the position coordinates (θ, ϕ, R) is $n_i \, R^2 \sin(\theta) \, d\theta \, d\phi \, dR$, and the configuration averaging is implicit.

This said, let us resume the calculation. The sum we must take care of is given in eq. (4.35). We now concentrate on the average and perform the integral

$$\sum_{m \neq m'} |\langle m'\sigma|H_0|m\sigma\rangle|^2 = \sum_{m \neq m'} V_0^2 \left(1 + \frac{R_{m'}}{a} \right)^2 e^{-\frac{2R_{m'}}{a}}$$

$$= V_0^2 \int_0^\pi d\theta_{m'} \sin(\theta_{m'}) \int_0^{2\pi} d\phi_{m'} \int_0^\infty dR_{m'} R_{m'}^2$$

$$n_i \left(1 + \frac{R_{m'}}{a} \right)^2 e^{-\frac{2R_{m'}}{a}} \qquad (4.45)$$

$$= 7\pi n_i a^3 V_0^2. \qquad (4.46)$$

The final result for τ_c then is

$$\frac{1}{\tau_c} = \frac{\sqrt{2}}{\hbar}\sqrt{7\pi n_i a^3 V_0^2}. \tag{4.47}$$

It is worth pointing out that only the density n_i, the effective Bohr radius and V_0 appear.

Typical spin rotation angle

An electron hopping between the impurities m and m' rotates by a typical angle given in eq. (4.42). On can also estimate the probability of jumping from an impurity m_0 to an impurity m' as

$$\frac{|t_{m_0 m'}^{\sigma\sigma}|^2}{\sum_{m''\neq m_0}|t_{m_0 m''}^{\sigma\sigma}|^2}$$

containing only non-flip matrix elements due to the larger magnitude of the MT energies over the SOC terms. This allows us to extract the mean-squared rotation angle per hop

$$\langle\theta^2\rangle = \frac{1}{\sum_{m''\neq m_0}|t_{m_0 m''}^{\sigma\sigma}|^2}\sum_{m'\neq m_0}\langle\theta_{m'}^2\rangle|t_{m'm_0}^{\sigma\sigma}|^2 \tag{4.48}$$

where we can still replace $\langle\theta_{m'}^2\rangle$ and obtain

$$\langle\theta^2\rangle = \frac{16}{3}\frac{\sum_{m'\neq m_0}|t_{m_0 m'}^{\bar{\sigma}\sigma}|^2}{\sum_{m''\neq m_0}|t_{m''m_0}^{\sigma\sigma}|^2} \tag{4.49}$$

The impurity average is to be done now. However we note that the sum in the denominator has just been calculated in the preceding section -see eq. (4.46)- upon the calculation of τ_c. We are then left with the numerator. Recalling that

$$t_{m'm_0}^{\bar{\sigma}\sigma} = \frac{\gamma}{\pi a^3}\left(\sigma I_{y,m'm_0} + iI_{x,m'm_0}\right)$$

we need to calculate the following integral

$$\sum_{m' \neq m_0} |t^{\bar{\sigma}\sigma}_{m_0 m'}|^2 \quad \rightarrow \quad \int dR_{m'}\, R^2_{m'}\, \sin(\theta_{m'})\, d\theta_{m'}\, d\phi_{m'}\, n^3_i \left(\frac{\gamma^2}{\pi a^3}\right)^2$$
$$\left(|I_{y,m'm_0}|^2 + |I_{x,m'm_0}|^2\right). \tag{4.50}$$

Replacing the corresponding terms in eq. (4.49), we obtain

$$\langle \theta^2 \rangle = \frac{16}{3} \left(\frac{\gamma}{\pi a^3}\right)^2 \frac{n_i a^3}{7\pi V_0^2 n_i a^3} 2 \cdot \langle c^2 \rangle (\pi/6)^2 \int dR R^2 R^4 \mathrm{e}^{-2R}. \tag{4.51}$$

The partial results

$$\langle c^2 \rangle = 4\pi \frac{16}{105}$$

and

$$\int dR R^2 R^4 \mathrm{e}^{-2R} = \frac{45}{8}$$

allow us to conclude

$$\langle \theta^2 \rangle = \frac{16}{3} \left(\frac{\gamma}{V_0 a^3}\right)^2 \frac{1}{7\pi} 2 \cdot 4\pi \frac{16}{105} \frac{1}{6^2} \frac{45}{8} = \left(\frac{\gamma}{V_0 a^3}\right)^2 \left(\frac{8}{21}\right)^2. \tag{4.52}$$

We observe that in the previous derivation, the integral has been split since the angular dependence appears in the parameter c of the function $I_{y,m'm_0}$ and $I_{x,m'm_0}$, whereas the radial integration variable enters as $(R/a)(\mathrm{e}^{-R/a})^2$. We underline that we now have the mean squared rotation angle as a function of the coupling parameter γ, the effective Bohr radius a, and the energy $V_0 = e^2/\epsilon a$ coming from the MT matrix element. By combining the values we have for τ_c and the just calculated $\langle \theta^2 \rangle$, we attain the formula for the spin-relaxation time

$$\frac{1}{\tau_\mathrm{s}} = \frac{1}{2} \frac{\langle \theta^2 \rangle}{\tau_\mathrm{c}} \simeq 0.48 \frac{\gamma^2}{a^6 V_0 \hbar} \mathcal{N}^{1/2}_\mathrm{i}. \tag{4.53}$$

where $\mathcal{N}_i = n_i a^3$. A point to be stressed is that the expression in (4.53) is free of adjustable parameters, and depends only on the properties of the material. We remark also that this expression for the spin-relaxation time is somewhat universal as it is valid for all n-doped zincblende semiconductors, in the vicinity of the MIT. Our analytical prediction for the spin-relaxation time using this formula is shown in Fig. 4.5 with solid lines. As it is evident, this result agrees very well with the experimental values for GaAs. The dashed line in the left lower part of the graphic corresponds to the analytical prediction for another ZB material, namely CdTe. The comparison with other relaxation mechanisms lets us conclude that the Dresselhaus coupling we have considered dominates in the impurity band for all zincblende semiconductors except the narrow-gap ones. To support this statement, we have also performed a numerical calculation of the spin-relaxation time, as described in next section.

4.5 Numerical calculation of the spin-relaxation time

Numerical calculations of the spin-relaxation time within our model provide an alternative path which is free of the simplifications used in the analytical approach. The numerical procedure starts with the calculation of the matrix elements (4.16) for H_D (and similarly for H_extr, numerically performed without approximations) for a given impurity configuration. We then diagonalize the total Hamiltonian $\mathcal{H}$ including the two contributions to the spin-orbit coupling and perform the time evolution of a given initial state. To determine this, we also diagonalize the bare MT Hamiltonian so as to take the initial state out of its set of eigenstates. In particular, only a reduced number of states with energies equal or slightly larger than the Fermi level are employed, all of them with $\sigma = 1$. We follow their spin evolution by calculating the mean value of $\sigma_z(t)$ numerically and extract the spin lifetime thereof.

The weakness of the spin-orbit coupling translates into spin-admixture perturbation energies which are, even for the largest system sizes (in terms of number of impurities,
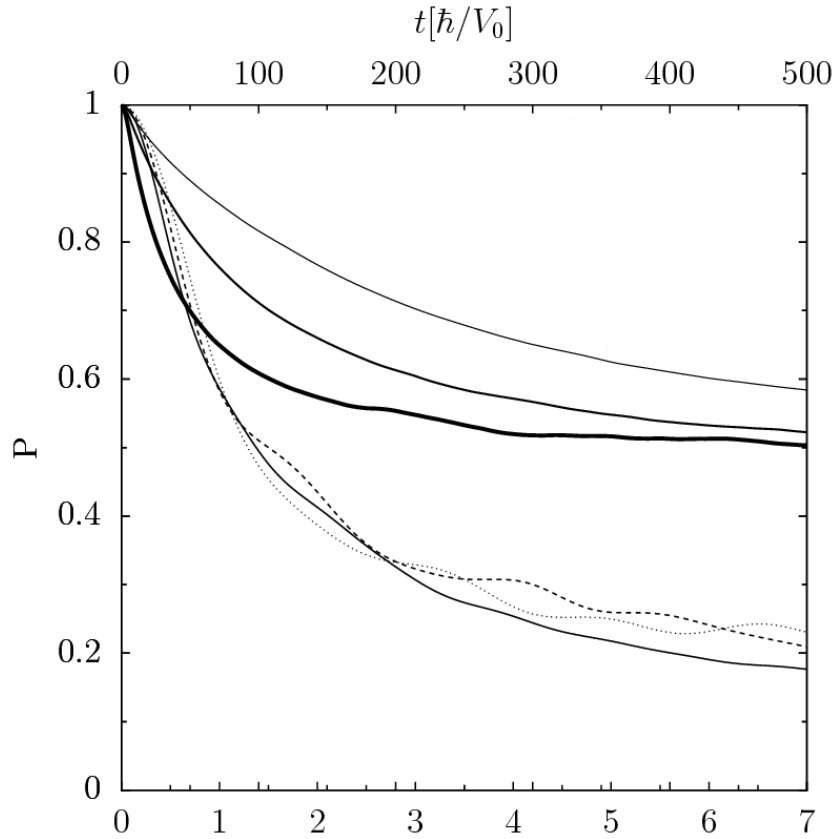
Figure 4.2: Spin survival probability P for an initial MT eigenstate at density $\mathcal{N}_i = 0.029$ and system size $N = 3375$ are shown with solid lines of increasing thickness (for $\eta =$75, 100, and 150). The corresponding time scale is in the upper x-axis. The other three curves are the average (over configurations) of the survival probability of an initial totally localized state (randomly taken), evolved under the influence of the full Hamiltonian (including SOC) for the same three different η values. Another time scale in the lower x-axis is used for them.

N) that we are able to treat numerically, orders of magnitude smaller than the typical MT level spacing. This large difference between the two energy scales in finite size simulations masks the spin-orbit-driven physics, and forces us to follow an indirect path: we introduce, as we did before, an artificially enhanced coupling constant $\eta\gamma$, where the control parameter is η, while γ is the real SOC coupling.

In Fig. 4.2, two different time-evolution curves are plotted. The curves with varying thickness correspond to the calculation of the average of the spin operator as a function of time t, in units of $[\hbar/V_0]$, shown in the upper x-scale. In this case, a single system size $N = 3375$ and density $\mathcal{N}_i a^3 = 0.029$ just above the MIT transition is considered, and the three lines of increasing thickness are produced with three different enhancing values $\eta = 75, 100, 150$. The largest η value generates, as expected, the fastest decay (thickest curve). The initial state is an eigenstate of the MT model at the Fermi level. For long times, the asymptotic behaviour is reached for the three curves indistinctly.

The other family of curves in Fig. 4.2 display the *survival probability* of an initial localized state, where the full Hamiltonian including SOC has been used for the time evolution. Here, a state localized on an initial randomly chosen site is evolved under the influence of the full Hamiltonian. Since this is not an eigenstate of the full $\mathcal{H}$, its projection onto the same site results in what is known as the *survival probability*. At time $t = 0$, this probability starts with a value of 1 and decays as the electron visits other impurities, although there is a quantum probability to return back. The three curves correspond to the same three different η values just mentioned, and the time scale for them is placed in the lower x-axis. As it is clearly shown, the survival probability does not depend on the enhancing factor, and is consistent to our previous assumption: the survival probability related to the mean-hopping time is mainly driven by the MT Hamiltonian, which is of course not affected by the enhance procedure. On the other hand, this probability tends asymptotically to zero in the long-time regime as the initial localized states diffuses and covers more and more sites. Upon observing the two sets of survival curves, the two largely different time scales (upper and lower x-axes) are to be noticed.
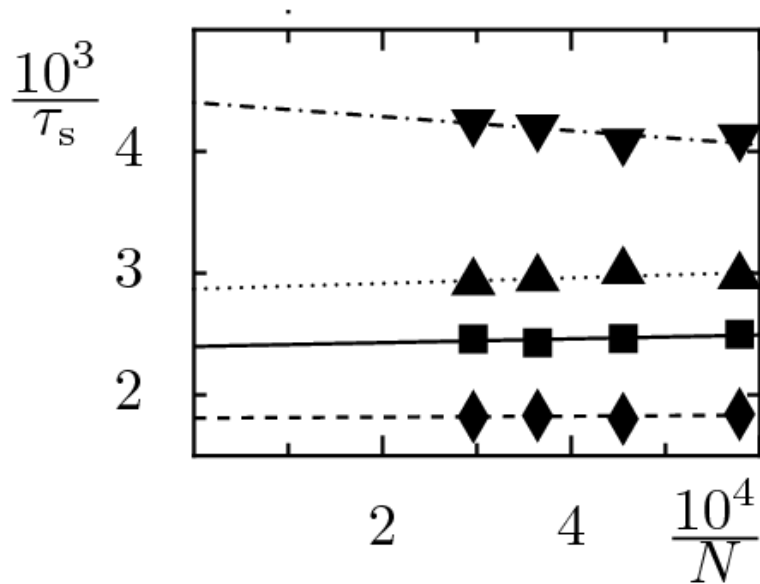
Figure 4.3: Size dependence of τ_{s}^{-1} for $\eta = 50$ at densities $\mathcal{N}_{\mathrm{i}} = 0.02$ ($\blacklozenge$), 0.029 ($\blacksquare$), 0.037 ($\blacktriangle$), and 0.06 ($\blacktriangledown$). Lines are linear fits to the data that allow to extrapolate to the infinite-size values.

The procedure for the calculation of the spin-relaxation time continues with a fitting of the spin survival curve, restricting the time interval to a certain window. After the initial perturbative regime characterized by a quadratic time decay, the spin survival continues with an exponential-like (though not strictly) decay. It was precisely this latter energy window that was identified and selected for the fitting stage, from which the relaxation rate τ_{s}^{-1} was calculated. For long times instead, the finite size effects manifest, giving rise to logarithmic decays.

In the same way as the standard finite-size scaling is used to extrapolate the infinite-size result, we have done something similar for the η scaling. Before this, we considered different systems sizes in order to perform a finite size-scaling for each value of η.

We devised thus a method that combines both scalings: for each density and effective coupling constant $\eta\gamma$, the asymptotic value of τ_{s}^{-1} was obtained by extrapolating the finite-N values to the infinite size limit. In Fig. 4.3, the curves correspond to different densities, and for each of those, various sizes were considered. The infinite-size limit was
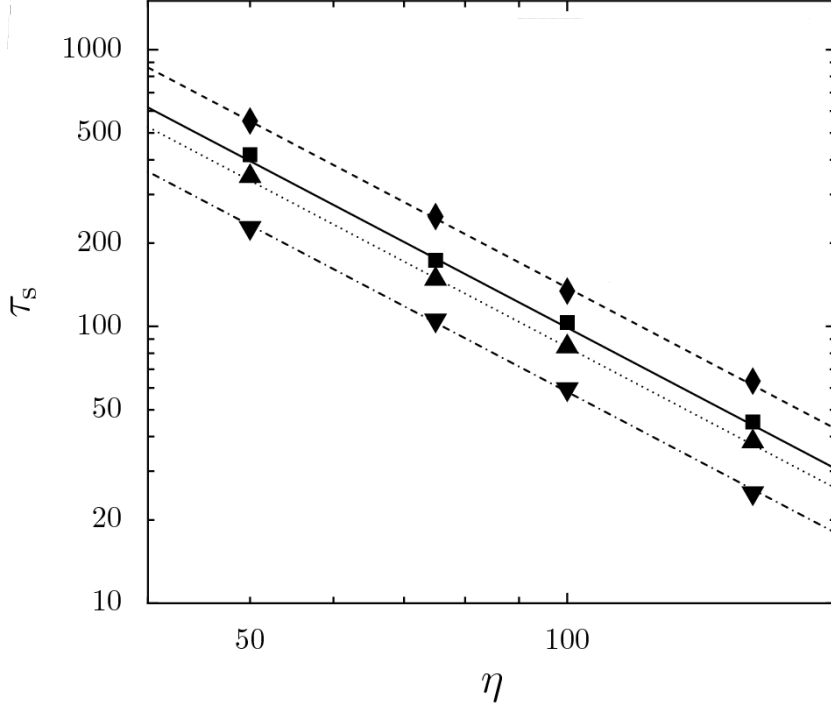
Figure 4.4: Scaling figure of the spin relaxation time extrapolated to infinite system size with the spin-orbit enhancement factor η, for densities $\mathcal{N}_i = 0.02$ ($\blacklozenge$), 0.029 ($\blacksquare$), 0.037 ($\blacktriangle$), and 0.06 ($\blacktriangledown$). The lines are fits of a quadratic dependence of the relaxation rate on η. Times are given in units of $\hbar/V_0$.

obtained by calculating the crossing with the y-axis. The same procedure was followed for each value of η. We so obtained a set of values $\tau_s(N \to \infty, n_i, \eta)$ for each η. The extra scaling was then performed for the parameter η (for each doping density), aiming at the real physical value $\eta = 1$ (see Fig. 4.4). The four extrapolated values for each density are our best estimation of the spin-relaxation time.

Applying the numerical procedure just described to the widely studied case of GaAs, we find that the numerically extracted values of the spin relaxation times associated with H_{extr} are, consistently with the results of Ref. [79], considerably larger than the ones observed experimentally. Therefore, we neglected this term in the numerical calculations, and concentrated on the spin evolution governed by H_{D}. We then ran a sufficiently large number of impurity configurations (typically 200) to make the statistical errors negligible

(smaller than the symbol size in the Fig. 4.4). In agreement with our analytical results, an inverse quadratic dependence of τ_s on the coupling strength is obtained (also shown in Fig. 4.4). The fitting of this dependence of τ_s on η allows us to extrapolate the spin-relaxation values to the physical values ($\eta = 1$) of the SOC strength. The results following this procedure are shown in Fig. 4.5 with purple filled circles for GaAs. The agreement with the experimental results is here remarkable as well, and we discuss them in the next section.

Other materials with other coupling parameters can be used by applying the same method. Moreover, we use the numerical results extracted for GaAs for the case of CdTe, which has a different γ value. To do this, the η values used for GaAs are renormalized and redefined so that the relation $\eta\gamma|_{GaAs} = \eta\gamma|_{CdTe}$ holds. For CdTe, the red plus symbols in Fig. 4.5 show our numerical results.

4.6 Results and conclusion

In Fig. 4.5 we present the spin-relaxation times resulting from our numerical approach for GaAs at four different impurity densities above the MIT (filled circles). We include the prediction of eq. (4.53) (solid line), and the available experimental data from Refs. [25,26, 29,30]. The vertical lines depict the critical (dark) and the hybridization (light) densities. We note that both approaches describe the data within the experimental uncertainty and correctly reproduce the density dependence of the spin-relaxation time. The departure of the analytical and numerical results is not significant, taking into account the different approximations of both paths and the arbitrariness associated with the definition of relaxation times in both formulations.

While in the critical region and deep into the localized regime there is some dispersion of the experimental values for GaAs, depending on the different samples and measurement technique, on the metallic side of the MIT, values of $\tau_s \gtrsim 100\,\text{ns}$ are consistently obtained. Our analytical and numerical results in Fig. 4.5 (solid line and filled circles, respectively) are obtained using for GaAs the values $V_0 = 11.76\,\text{meV}$ and $\gamma = 27\,\text{eV\AA}^3$
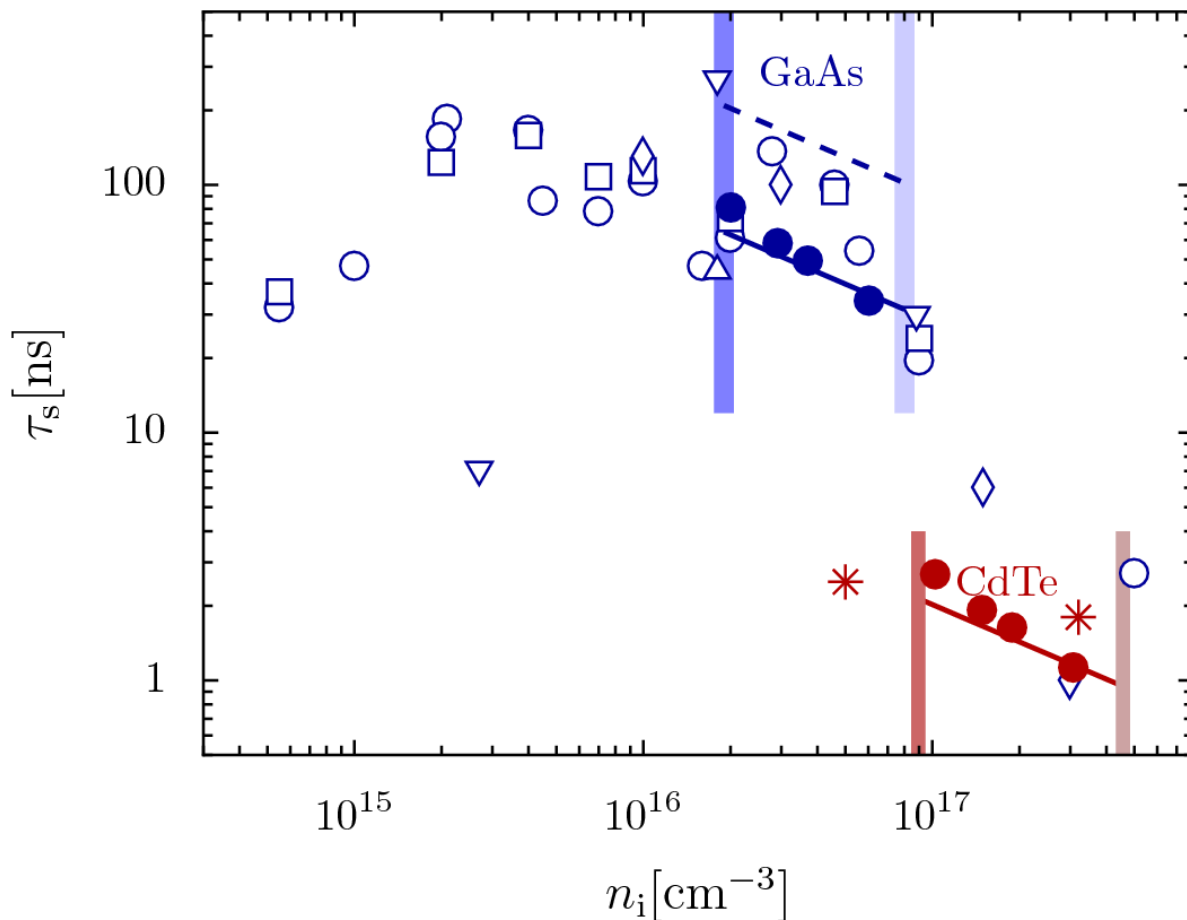
Figure 4.5: Spin relaxation time as a function of doping density. For n-doped GaAs (blue), the prediction of eq. (4.53) (solid line) and our numerical results (●) for the metallic regime between the metal-insulator transition (dark thick vertical line) and the hybridization of the impurity band with the conduction band (light thick vertical line) obtained using $\gamma = 27\,\text{eV\AA}^3$ are compared to experiments. Data are taken from Ref. [26] for $T = 2\,\text{K}$ (○) and $T = 4.2\,\text{K}$ (□), Ref. [25] (◇), Ref. [29] (△), and Ref. [30] (▽). The case of CdTe is shown by the red solid line (eq. (4.53)), numerical results (●) and experimental data from Ref. [104] (∗).

without any adjustable parameter. We also remark that these results are quite sensitive to the value of γ. For example, taking the smaller values suggested in the literature [24, 105] results in larger relaxation times. The identification of the Dresselhaus coupling as the dominant channel for spin relaxation close to the MIT provides a strong motivation to pursue further experimental and theoretical work in order to determine a more precise value of γ.

Regarding other materials, spin-relaxation measurements have recently been performed in bulk CdTe at various doping densities [104]. A non-monotonic behaviour was obtained and in particular, an substantial increase of the spin-relaxation time for density values larger than $5 \times 10^{15} cm^{-3}$ was observed. The authors estimated an optimal value of $\tau_s = 2.5$ ns close to the MIT, at a density $n^{opt} = 5 \times 10^{16} cm^{-3}$ (shown in Fig. 4.5). After this, a decrease in τ_s was measured for densities $\geq 10^{17} cm^{-3}$. Also in this case the experimental data for densities near the MIT ($*$ in Fig. 4.5) are well described by the numerically extracted values of τ_s (+) and by the prediction of eq. (4.53) from our theory. Our numerical calculations are universal and the material parameters enter upon performing the scaling procedure.

The agreement between theory and experiment for both GaAs and CdTe in spite of their dissimilar material parameters illustrates the wide applicability of our results. In narrow-gap semiconductors, like InAs and InSb, the particularly large Bohr radii lead to very long Dresselhaus relaxation times, which in the first case are even longer than those yielded by the extrinsic coupling [79]. However, the extremely low critical densities of these materials make it difficult to probe the physics of spin relaxation in the impurity band, and in these cases of low-densities, the spin relaxation has been proposed to be governed by other mechanisms [91].

In conclusion, we have identified a spin-relaxation mechanism characteristic of electrons on the metallic side of the metal-insulator transition in the impurity band of semiconductors, thereby solving a longstanding problem in spintronics. Our mechanism is based on the Dresselhaus spin-orbit coupling, and we find that it dominates over the usually stronger extrinsic counterpart, and provides relaxation times that are in good

agreement with the experimentally measured values.

Chapter 5

Quantum Dots

In the last part of the thesis we study the effects of spin-orbit interaction on the electronic states of cylindrical quantum dots defined on quantum wires having wurtzite lattice structure. The linear and cubic contributions of the bulk Dresselhaus spin-orbit coupling are taken into account, along with the influence of an external magnetic field, pointing in the direction along the wire. The previously found analytic solution to the one-particle Schrödinger equation for an electron in a quantum dot with a cylindrical hard-wall confining potential in a zincblende lattice structure with Rashba interaction is extended to the case of nanowire-based quantum dots, where the nanowire presents a wurtzite-type structure. We display the effect of the spin-orbit coupling on the energy levels and present examples for the spin structure of the one-particle eigenstates. We also address the experimentally accessible effective g-factor of the quantum dots, and analyze in the sequel the spin relaxation due to the coupling to phonons. After that, we discuss the conclusions.

5.1 Presentation

Nowadays, it is possible to produce sharply defined quantum dots with square-well confinement in the longitudinal direction of a nanowire, with highly controllable lengths. An important aspect of these semiconductor nanorods is that they often display the wurtzite

crystal structure even though the constituting material has a zincblende structure in the bulk [53]. Since the dot is built by confining a conduction electron, this structural change affects the spin properties of the dots. Notably, while in the zincblende semiconductors the leading Dresselhaus spin-orbit coupling term is cubic in $\mathbf{k}$, in wurtzite crystals a linear term appears [55]. While this last term has been known for some time [55], the cubic term in $\mathbf{k}$ has been obtained only recently within the $\mathbf{k} \cdot \mathbf{p}$ approximation for different wurtzite semiconductors [56,73]. De and Pryor [57] calculated the band-structure parameters of several binary compounds which normally display the zincblende structure in the bulk assuming that they have the wurtzite structure. These parameters are thus available for the study of wurtzite nanowires. These new data pave the way to a realistic study of nanowire-based quantum dots with wurtzite structure, which we next undertake.

Disk-shaped quantum dots with the Rashba structural SOC have been shown to admit an analytical solution for their energy eigenstates, without [106] and with [107] an applied perpendicular magnetic field. This solution, as we show here, can be conveniently extended to wurtzite quantum dots having cylindrical symmetry around the crystal c-axis, either with flat (disk) or elongated ("rod") geometry. This is the case since the linear wurtzite Dresselhaus coupling is mathematically equivalent to the Rashba linear spin-orbit coupling characteristic of asymmetric semiconductor quantum wells, and furhermore, the newly obtained cubic term of wurtzite admits in the quasi-two-dimensional case the same eigenstates as the linear term. In this work we exploit these similarities in order to give solutions of the eigenvalue problem of the wurtzite quasi-two-dimensional structures and cylindrical quantum dots. As we will see, in a confined geometry, the wurtzite cubic term of the Dresselhaus coupling gives rise to an additional linear contribution that reinforces or counteracts the bare linear term. This reinforcement can be actually much bigger than the original linear term, opening up an unexplored regime of strong "Rashba-like" spin-orbit coupling in quantum wells and dots. Also, the combination of these linear Dresselhaus terms with the standard Rashba term due to structural asymmetry could give rise to new possibilities. For instance, flexible schemes of spin-

orbit coupling cancellation could be implemented leading to very long spin relaxation times in wurtzite structures having particular geometric shapes [108].

We next continue with the spin-orbit coupling terms in a quasi-two-dimensional confined system, including both the spin-orbit coupling for wurtzite structures and a Zeeman interaction. Afterwards, we make use of these solutions to address problem of a cylindrical quantum-dot problem with a variable length and hard-wall confinement potential.

5.2 Intrinsic spin-orbit coupling in wurtzite-based confined geometries

Within the envelope-function approximation for conduction-band electrons in wurtzite semiconductors, the effective Hamiltonian [76, 77] incorporating the linear [55] and cubic [56, 73] Dresselhaus spin-orbit couplings reads

$$H = H_0 + H_1 + H_3 + H_{\mathrm{Z}}, \tag{5.1}$$

$$H_0 = \frac{p^2}{2\,m^*} + V_{\mathrm{c}}(x, y, z), \tag{5.2}$$

$$H_1 = \alpha\,(k_y\sigma_x - k_x\sigma_y), \tag{5.3}$$

$$H_3 = \gamma\,\left(bk_z^2 - k_x^2 - k_y^2\right)(k_y\sigma_x - k_x\sigma_y), \tag{5.4}$$

$$H_{\mathrm{Z}} = \frac{1}{2}g^*\mu_{\mathrm{B}}B\sigma_z, \tag{5.5}$$

where V_{c} is a nanoscale confinement potential, $\boldsymbol{\sigma}$ is the spin operator, α, γ, and b are material-dependent parameters, g^* is the bulk effective gyromagnetic factor, μ_{B} is the Bohr magneton, and B is an external magnetic field assumed to be applied in the z-direction. Here we include the magnetic field only through a Zeeman term since we consider only relatively weak fields whose orbital effects can be safely ignored.

The catalytically grown nanorods made out of materials which have the zincblende crystal structure in the bulk can adopt either the zincblende or the wurtzite structure depending on the size of the nanoparticle seed and other growth conditions. However, experimental data allowing to determine α, γ, and b are not yet available, so in our study

we will rely on the theoretical estimates obtained by De and Pryor [57]. These authors calculated all the relevant band-structure parameters assuming a wurtzite structure for the semiconductor binary compounds that have a zincblende structure in the bulk. In order to give a wider applicability to our results, whenever possible we present them for reasonably large ranges of parameters so that they can be adapted to different materials and to parameters newly obtained, either experimentally or theoretically.

In what follows we consider quasi-two-dimensional systems, whose solutions are used for the quantum dot problem.

5.3 Quasi-two-dimensional systems

Before tackling the quantum-dot problem it is useful to consider the eigenvalue problem of a quasi-two-dimensional system. Thus, we choose $V_c = V_c(z)$ which confines the electrons only along the z-direction, such that H_0 can be separated as $H_0 = H_0^{xy} + H_0^z$, with an in-plane term $H_0^{xy} = (p_x^2 + p_y^2)/2m^*$ and $H_0^z = p_z^2/2m^* + V_c(z)$.

5.3.1 Linear term

If we leave aside for the moment the cubic term H_3 and the external magnetic field, we are left with a situation analogous to the classic Rashba problem in which the spin-orbit coupling originates from an asymmetric potential. Since the Hamiltonian is separable we can start working with the two-dimensional problem in the (x, y) plane given by $H_0 = H_0^{xy} + H_1$. Its well-known solution is [78]

$$\Psi_{\mathbf{k}s}(\mathbf{r}) = \frac{1}{\sqrt{2A}} e^{i\mathbf{k}\cdot\mathbf{r}} \begin{pmatrix} se^{-i\left(\varphi_k - \frac{\pi}{2}\right)} \\ 1 \end{pmatrix}, \tag{5.6}$$

$$E(k, s) = \frac{\hbar^2 k^2}{2m^*} - s\alpha k. \tag{5.7}$$

In these expressions and in what follows $\mathbf{r} = (x, y)$, $\mathbf{k} = (k_x, k_y)$, $k = \sqrt{k_x^2 + k_y^2}$, φ_k is the angle of $\mathbf{k}$ in polar coordinates, and A is the area of the sample. The spin quantum number $s = \pm 1$ denotes spin-up and spin-down eigenstates with respect to the spin

quantization axis which lies in the xy-plane and is perpendicular to $\mathbf{k}$ with a polar angle $\varphi_k - \pi/2$. Note that the spin-orbit term in the energy has a minus sign compared to the usual Rashba expression, coming from the minus sign used in eq. (5.3). The states (5.6) are degenerate for given k and s. This plane-wave solution is convenient in most contexts and has the advantage that its spin quantization direction is position independent. However, (5.6) does not profit from the fact that the z-component of the total angular momentum J_z commutes with the Hamiltonian and therefore provides a good quantum number, which is an extremely useful property when one tackles cylindrically symmetric nanostructures. The common eigenstates of H and J_z are given by [106]

$$\Psi_{m,k,s}(r, \varphi) = \begin{pmatrix} J_m(kr)\, e^{im\varphi} \\ sJ_{m+1}(kr)\, e^{i(m+1)\varphi} \end{pmatrix}. \tag{5.8}$$

The states (5.8) are degenerate with those of (5.6) for given k and s, and can be expressed as superpositions of them. Note that while the spin of the basis states (5.6) lies always in the xy-plane, that is not the case for the states (5.8), which are superpositions of the states (5.6) within degenerate subspaces. Furthermore, the spin direction in the latter is space-dependent while in the former it is not.

5.3.2 Cubic term

Let us now include the cubic-in-k term of the Hamiltonian, H_3, given in eq. (5.4), and the Zeeman energy, eq. (5.5). As usual, we work in the envelope-function approximation where the Hamiltonian H is expressed by replacing $\mathbf{k}$ by $-i\nabla$. We adopt cylindrical coordinates (r, φ, z) and for the in-plane coordinates we have

$$k_x = -i\frac{\partial}{\partial x} = -i\cos\varphi\frac{\partial}{\partial r} + i\frac{\sin\varphi}{r}\frac{\partial}{\partial\varphi} \tag{5.9}$$

$$k_y = -i\frac{\partial}{\partial y} = -i\sin\varphi\frac{\partial}{\partial r} - i\frac{\cos\varphi}{r}\frac{\partial}{\partial\varphi} \tag{5.10}$$

$$\nabla^2 = \frac{\partial^2}{\partial x^2} + \frac{\partial^2}{\partial y^2} = \frac{1}{r}\frac{\partial}{\partial r} + \frac{\partial^2}{\partial r^2} + \frac{1}{r^2}\frac{\partial^2}{\partial\varphi^2}. \tag{5.11}$$

Note that we use the symbol ∇^2 to represent the two-dimensional Laplacian. Leaving H_1 unexpanded for the moment, the Hamiltonian reads

$$H = -\frac{\hbar^2}{2m^*}\left(\nabla^2 + \frac{\partial^2}{\partial z^2}\right) + V_c(z) + H_1$$
$$+\frac{\gamma}{\alpha}\left[b\left(-\frac{\partial^2}{\partial z^2}\right) + \nabla^2\right]H_1 + H_Z. \tag{5.12}$$

Assuming that $V_c(z)$ is an infinite potential well of length L, the proposed solution of the time-independent Schrödinger equation $H\Phi = E\Phi$ is

$$\Phi_{nm}(r, \varphi, z) = \Psi_{nm}(r, \varphi)\sin\left(\frac{n\pi z}{L}\right), \tag{5.13}$$

$$\Psi_{nm}(r, \varphi) = \begin{pmatrix} u_{nm}(r)\,e^{im\varphi} \\ v_{nm}(r)\,e^{i(m+1)\varphi} \end{pmatrix}, \tag{5.14}$$

where $u_{nm}(r)$ and $v_{nm}(r)$ are real functions and $\Psi_{nm}(r, \varphi)$ is an eigenstate of J_z with eigenvalue $j_z = m + 1/2$. The corresponding total energy is

$$E_n^t = E_n + E_n^z, \tag{5.15}$$

with the radial part E_n and the longitudinal energy $E_n^z = (\hbar^2/2m^*)(n\pi/L)^2$ from the confinement in z-direction. After plugging (5.13) in the Schrödinger equation, we obtain the following coupled equations for u_{nm} and v_{nm}

$$\left(-\nabla_m^2 + h\right)u_{nm}(\rho) + \left(\alpha_n' + \gamma'\nabla_m^2\right)\left(\frac{m+1}{\rho} + \frac{\partial}{\partial\rho}\right)v_{nm}(\rho) = \varepsilon_n u_{nm}(\rho) \tag{5.16}$$

$$\left(-\nabla_{m+1}^2 - h\right)v_{nm}(\rho) + \left(\alpha_n' + \gamma'\nabla_{m+1}^2\right)\left(\frac{m}{\rho} - \frac{\partial}{\partial\rho}\right)u_{nm}(\rho) = \varepsilon_n v_{nm}(\rho) \tag{5.17}$$

where

$$\nabla_m^2 \equiv \frac{1}{\rho}\frac{\partial}{\partial\rho} + \frac{\partial^2}{\partial\rho^2} - \frac{m^2}{\rho^2}. \tag{5.18}$$

In eqs. (5.16) and (5.17) we have introduced R, a parameter to be defined in the quantum-dot context, and $u_E = \hbar^2/2m^*R^2$, as units of length and energy, respectively. This allows to define dimensionless parameters as $\rho = r/R$, $K = kR$, $\gamma' = \gamma/u_E R^3$, and $h = g\mu_B B/2u_E$. The dependence on the ("longitudinal") quantum number n has been

incorporated to the in-plane problem via the redefinition of the coupling constant α to write the dimensionless

$$\alpha'_n = \left[\alpha + \gamma b \left(\frac{n\pi}{L}\right)^2\right]/u_{\text{E}}R\,,\tag{5.19}$$

and the in-plane dimensionless energy is given by $\varepsilon_n = E_n/u_{\text{E}}$.

To solve eqs. (5.16) and (5.17) we make the ansatz

$$u_{nm}(\rho) = J_m(K\rho), \quad v_{nm}(\rho) = d_n J_{m+1}(K\rho).\tag{5.20}$$

Using the property of the Bessel functions

$$\left(\frac{m}{\rho} - \frac{\partial}{\partial\rho}\right) J_m(K\rho) = K J_{m+1}(K\rho),\tag{5.21}$$

$$\left(\frac{m+1}{\rho} + \frac{\partial}{\partial\rho}\right) J_{m+1}(K\rho) = K J_m(K\rho),\tag{5.22}$$

one obtains from (5.16) and (5.17) the 2×2 eigenvalue equation

$$\begin{pmatrix} K^2 + h - \varepsilon_n & \alpha'_n K - \gamma' K^3 \\ \alpha'_n K - \gamma' K^3 & K^2 - h - \varepsilon_n \end{pmatrix} \begin{pmatrix} 1 \\ d_n \end{pmatrix} = 0\tag{5.23}$$

whose solutions are

$$\varepsilon_{n\pm} = K^2 \pm \sqrt{K^2 \left(\alpha'_n - \gamma' K^2\right)^2 + h^2}.\tag{5.24}$$

Then, the total energy is given by

$$E_{n\pm}^{\text{t}} = (\varepsilon_{n\pm} + \varepsilon_n^z) u_{\text{E}}\,,\tag{5.25}$$

with $\varepsilon_n^z = E_n^z/u_{\text{E}} = (n\pi R/L)^2$. The coefficients in the eigenvectors are determined by

$$d_{n\pm} = \frac{\varepsilon_{n\pm} - K^2 - h}{\alpha'_n K - \gamma' K^3}\,.\tag{5.26}$$

The obtained solution, eqs. (5.24) and (5.26), reduces to the one of the linear Hamiltonian analyzed in Sec. 5.3.1, given by eqs. (5.7) and (5.8), when the cubic term and the Zeeman energy are neglected. As in the linear Rashba problem, there are two possible energies $\varepsilon_{n\pm}$ for a given value of K. The energies $\varepsilon_{n\pm}$, being a function of K^2, are independent of the sign of K. Because of the (anti-)symmetry of the Bessel functions with respect to a change of sign in the argument, considered along with the change of sign of $d_{n\pm}$,

the wavefunctions corresponding to $\pm K$ are not independent. We therefore keep only positive values of K.

In the presence of a magnetic field, and for in-plane energies ε_n close to zero, eq. (5.24) has solutions with imaginary $K = i\kappa$. Since $J_m(i\kappa\rho) = i^m I_m(\kappa\rho)$, where I_m is the modified Bessel function of order m of the first kind, the corresponding wavefunctions grow exponentially with increasing ρ and are thus not normalizable in an infinitely large system. Such solutions are therefore discarded in the context of two-dimensional systems, yet they become relevant for the case of quantum dots discussed in Sec. 5.4.

In Fig. 5.1 we present (solid lines) the dispersion relation (5.25) for InAs with the parameters suggested in Ref. [57] from band-structure calculations (we label them with an index r)

$$\alpha_r = 0.571 \text{ eVÅ} \qquad \gamma_r = 571.8 \text{ eVÅ}^3,$$

$b = 4$ and an effective mass $m^* = 0.026\, m_e$ [48]. The two energy branches are plotted for $B = 0\,\text{T}$ (left) and $B = 20\,\text{T}$ (right). In this figure we consider a large value of the magnetic field just for illustrating more clearly its effects on the energy levels. We also show the effect of suppressing the cubic term, but keeping the contribution of γ in eq. (5.19) on the linear term (dashed line), and also the usual Rashba case with $\gamma = 0$ (dotted line). Blue (red) lines correspond to ε_{n-} (ε_{n+}). Thick lines correspond to $n = 1$, as indicated between the two panels. Also shown are the curves of ε_{2-} and ε_{3-} including the linear and cubic spin-orbit contributions (thin lines). For $n = 1$ and $B = 0\,\text{T}$ there is a crossing of the two branches at $K = \sqrt{\alpha'/\gamma'}$ ($K = 19.34$ in our plot). This feature has been discussed in the literature as a possible opportunity to implement long-lived spin qubits [109]. The crossing becomes avoided for finite B, although the level splitting can hardly be seen on the right panel of Fig. 5.1. For this reason we plot in the inset the energies subtracting the trivial parabolic contribution. This allows for a smaller energy range such that one can clearly note the Zeeman splitting at $K = 0$ and the avoided crossing.

In Fig. 5.1, the thin solid lines are the lower branches of subbands $n = 2$ and 3. Even though they lie at sufficiently high energies so as not to affect our further analysis, which
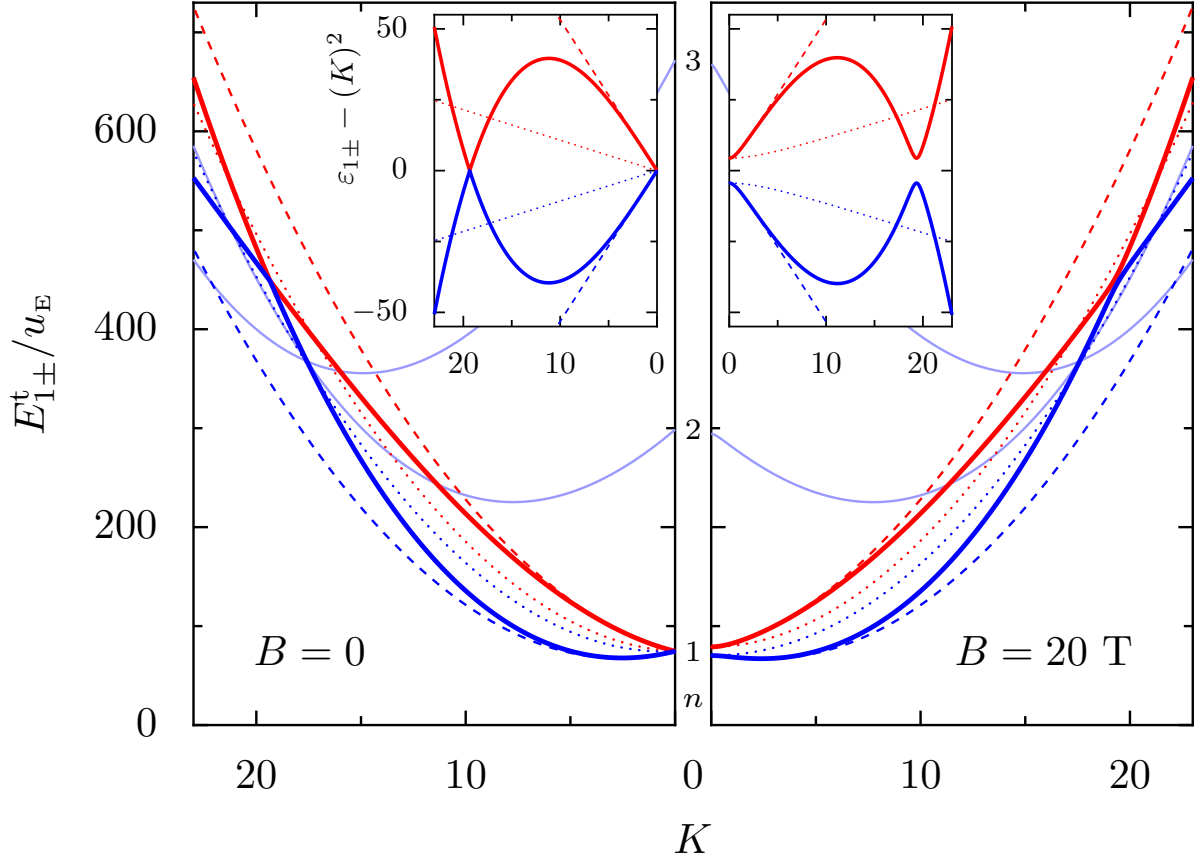
Figure 5.1: Energy dispersion from eq. (5.25) with (right) and without magnetic field (left). For subband $n = 1$, three cases are considered: thick solid lines correspond to the full SOC, dashed lines to an intermediate case with no cubic-in-k SOC, but with the α parameter renormalized by γ (5.19), and dotted lines to the bare Rashba interaction, linear in k. Blue (red) lines correspond to ε_{n-} (ε_{n+}). The thinner solid lines are the lower branches of subbands $n = 2$ and 3. *Inset*: Full SOC dispersion relation without the parabolic contribution for $n = 1$. The Zeeman effect and an avoided crossing are more clearly distinguished on this energy scale.

concentrates on low energies, we note that they could become relevant if the region of the avoided crossing mentioned above is explored. Also, we point out a potentially interesting degeneracy point of all the lower branches of the different subbands, which happens at $K = 1/b\gamma'$ ($K = 17.58$ in our plot), where the curves become independent of n. This massive degeneracy is due to the renormalized linear spin-orbit term. Although this feature may be physically relevant, we mention that higher values of n correspond to higher k_z and eventually the energies of eq. (5.25) obtained in third-order perturbation theory in wavevector cease to be reliable.

5.4 Quantum dots

5.4.1 Effect of spin-orbit coupling on the energy levels

We now consider cylindrical quantum-dots with hard-wall quantum confinement having radius R and length L. The discrete eigenenergies and states of this problem will be obtained from the quantum-well solutions found in the previous Section. In order to get the energetically lowest states, we keep only the lowest subband, $n = 1$, and omit the subindex n from now on. In all cases we work with k low enough to stay in the perturbative regime of SOC.

The eigenstates of the disk-shaped quantum dot have to satisfy the circular boundary condition (the hard-wall confinement forces a zero of the wave function at the dot boundary). This can be achieved at particular values of the in-plane energy ε for linear combinations of two degenerate eigenstates of the quantum-well problem. Those quantized energies are then the eigenenergies of the quantum dot. In the general case including a finite magnetic field, there are three energy ranges (see Fig. 5.1) with different situations:

i) energies in the low "belly" of the ε_- branch, $\varepsilon < -|h|$;

ii) energies above the energy gap caused at $K = 0$ by the Zeeman splitting, $\varepsilon > |h|$;

iii) energies in the Zeeman gap, $-|h| < \varepsilon < |h|$.

We now consider these three cases separately.

Case i): two real values of K, K_a and K_b, associated to the ε_- branch (in the "belly" region) are involved in the dot solution. The in-plane wave function is thus written as

$$\Psi_m(\rho, \varphi) = c_a \begin{pmatrix} J_m(K_a\rho)e^{im\varphi} \\ d_-(K_a)J_{m+1}(K_a\rho)e^{i(m+1)\varphi} \end{pmatrix} + c_b \begin{pmatrix} J_m(K_b\rho)e^{im\varphi} \\ d_-(K_b)J_{m+1}(K_b\rho)e^{i(m+1)\varphi} \end{pmatrix}, \quad (5.27)$$

with the boundary condition $\Psi_m(\rho = 1, \varphi) = 0$. A non-trivial solution (K_a, K_b) will be given by the condition

$$J_m(K_a)\,d_-(K_b)J_{m+1}(K_b) - J_m(K_b)\,d_-(K_a)J_{m+1}(K_a) = 0\,. \quad (5.28)$$

Case ii): the two quantum-well states involved in the dot solution belong to different branches, ε_+ and ε_-, with real values of K, K_a and K_b:

$$\Psi_m(\rho, \varphi) = c_a \begin{pmatrix} J_m(K_a\rho)e^{im\varphi} \\ d_+(K_a)J_{m+1}(K_a\rho)e^{i(m+1)\varphi} \end{pmatrix} + c_b \begin{pmatrix} J_m(K_b\rho)e^{im\varphi} \\ d_-(K_b)J_{m+1}(K_b\rho)e^{i(m+1)\varphi} \end{pmatrix}. \quad (5.29)$$

The boundary condition $\Psi_m(\rho = 1, \varphi) = 0$ leads to

$$J_m(K_a)\,d_-(K_b)J_{m+1}(K_b) - J_m(K_b)\,d_+(K_a)J_{m+1}(K_a) = 0\,. \quad (5.30)$$

Case iii): one imaginary value of K, $K_a \equiv i\kappa_a$, and a real value K_b are involved. The energy associated to K_a is

$$\varepsilon_{\pm,a} = -\kappa_a^2 \pm \sqrt{-\kappa_a^2 \left(\alpha_n' + \gamma'\kappa_a^2\right)^2 + h^2}, \quad (5.31)$$

and the coefficient for the wave function

$$d_\pm(K_a) = (-i)\frac{\varepsilon_{\pm,a} + \kappa_a^2 - h}{\alpha_n'\kappa_a + \gamma'\kappa_a^3} \equiv -i\delta_\pm(\kappa_a)\,. \quad (5.32)$$

With $J_m(i\kappa\rho) = i^m I_m(\kappa\rho)$, the quantum-dot wave function is then written as

$$\Psi_m(\rho, \varphi) = i^m c_a \begin{pmatrix} I_m(\kappa_a\rho)e^{im\varphi} \\ \delta_\pm(\kappa_a)I_{m+1}(\kappa_a\rho)e^{i(m+1)\varphi} \end{pmatrix} + c_b \begin{pmatrix} J_m(K_b\rho)e^{im\varphi} \\ d_-(K_b)J_{m+1}(K_b\rho)e^{i(m+1)\varphi} \end{pmatrix}. \quad (5.33)$$

The boundary condition $\Psi_m(\rho = 1, \varphi) = 0$ leads to

$$I_m(\kappa_a)d_-(K_b)J_{m+1}(K_b) - J_m(K_b)\delta_\pm(\kappa_a)I_{m+1} = 0\,. \quad (5.34)$$
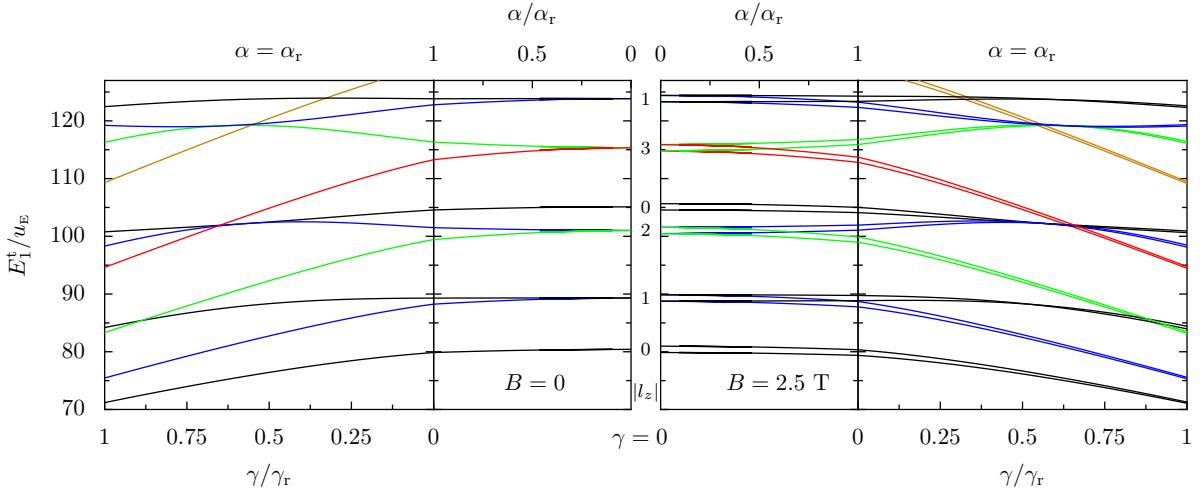
Figure 5.2: The discrete eigenenergies of a quantum dot with radius $R = 275\text{Å}$ and height $L = 100\text{Å}$ for $n = 1$, shown as a function of the spin-orbit coupling strengths α and γ, without magnetic field (left side) and with $B = 2.5\,\text{T}$ (right side). States with $|j_z| = 1/2, 3/2, 5/2, 7/2,$ and $9/2$ are represented by different black, blue, green, red, and orange lines, respectively. In the central panels we keep $\gamma = 0$ and vary α from zero up to $\alpha_r = 0.571\,\text{eVÅ}$, reported in [57]. Conversely, in the following curves (outside panels) α is fixed at α_r, and γ increases from zero to its final value of $\gamma_r = 571.8\,\text{eVÅ}^3$. In between the panels, the values of the quantum numbers l_z associated to the nearby states at zero SOC are indicated.

Equations (5.28), (5.30), and (5.34) express a root-finding problem, which we solve numerically. We find a family of solutions for each value of m that correspond to the discretized energies of the quantum dot. All of these solutions carry a well-defined value of $j_z = m + 1/2$, and in the absence of a magnetic field, the j_z and $-j_z$ solutions are degenerate.

The results for the energy levels are presented in Fig. 5.2 as a function of the SOC coupling strength. The states of different $|j_z|$ are shown in different color. To show the effect of the spin-orbit coupling, we start from the case of vanishing SOC in the center of the figure and increase the SOC strength up to the predicted values α_r and γ_r

corresponding to the left and right edge of the figure.

Without SOC (inner edges of the plot), the electronic states can be characterized by the orbital angular momentum l_z along the z-axis and the spin $s = \pm 1/2$, in addition to the total angular momentum $j_z = l_z + s$. The values of $|l_z|$ corresponding to the states are indicated in the center of the figure. Without magnetic field (left side), the states characterized by $(l_z, s) = (\pm|l_z|, \pm 1/2)$ are degenerate. When a magnetic field is included (right side), the Zeeman energy splits the different spin orientations. In the presence of SOC, the orbital angular momentum and the spin get mixed, l_z and s cease to be good quantum numbers. In this case only the total angular momentum quantum number j_z, shown by the different colors in Fig. 5.2 characterizes the states. It can be seen that the SOC splits states characterized by different values of j_z, while they correspond to the same $|l_z|$ at zero SOC.

In order to separate the effects of the different SOC terms, we increase the SOC in two steps. We first consider the usual Rashba problem by setting $\gamma = 0$ and varying the linear coupling strength α from zero up to $\alpha_r = 0.571 \text{eVÅ}$. This situation is depicted in the inner part of Fig. 5.2, where the left side corresponds to the case of zero magnetic field and the right side to $B = 2.5 \, \text{T}$. The ensuing step is to fix α at α_r and increase the γ value from zero to $\gamma_r = 571.8 \, \text{eVÅ}^3$. The result is matched with the previous one and traced by the adjoining curves in the outer panels of the figure. It must be noted that γ determines not only the cubic-in-k SOC coupling, but it also enters in the linear-in-k coupling (cf. eq. (5.19)). Consequently, at the end of each curve we find the energy of the quantum dot for the corresponding α_r and γ_r. This way of presenting the results shows separately the contribution of each of the SOC parameters.

The significant effect of γ on the eigenenergies, that leads to much stronger energy changes than α alone, must be noted. It brings, for example, the lowest pair of levels with $j_z = \pm 1/2$ (lowest black curves) down to energies that are below E_1^z. Moreover, level crossings occur as a function of γ, changing the order of the states in energy with respect to the case of vanishing SOC. This happens mainly for the lowest energy states of a given $|j_z|$ that are pulled down by the SOC below the higher energy states with

lower values of $|j_z|$. We remark that the full range of eigenenergies that we consider has not been explored in previous studies, and that we explicitly include allowed energy values that lie within the gap of the two-dimensional dispersion relation of Fig. 5.1, that is $-|h| < \varepsilon_1 < |h|$. It can also be observed that the Zeeman splitting shrinks as the SOC increases, while the spin mixture brought about by the latter increases accordingly. This indicates that the effective g-factor in quantum dots is affected by the SOC and depends on the geometry. We come back to this after next section, where we study the spin texture.

## 5.4.2 Spin structure of the eigenstates

We now examine the spin structure of the quantum dot states. The spinor states of eqs. (5.27), (5.29), and (5.33) determine the spin texture of states across the dot. Without SOC and in the presence of a magnetic field, even a very weak one, the states are spin polarized, and the spin texture of the one-electron states is uniform throughout the dot. The appearance of a non-trivial spin texture is therefore a signature of the SOC, and can be seen as the degree of mixing of the two spin components in an eigenspinor. To obtain the spin texture corresponding to a state, we compute the expectation value of the spin operator

$$\langle \boldsymbol{\sigma} \rangle(\mathbf{r}) = \frac{\Psi^\dagger(\mathbf{r}) \boldsymbol{\sigma} \Psi(\mathbf{r})}{\Psi^\dagger(\mathbf{r}) \Psi(\mathbf{r})} \tag{5.35}$$

for each spatial point $\mathbf{r}$ inside the quantum dot. Because of the separability of the wavefunctions (5.13), the spin orientation is independent of the longitudinal coordinate z. Moreover, the rotational symmetry of the dots around the z-axis imposes that the resulting spin orientations present the same symmetry. Therefore, their projection on the $\hat{\varphi}$-direction vanishes, such that the local spin direction

$$\langle \boldsymbol{\sigma} \rangle(\mathbf{r}) = \hat{r} \cos(\beta(r)) + \hat{z} \sin(\beta(r)) \tag{5.36}$$

has only a radial component and a component along the z-axis. The angle of the local spin orientation with respect to the xy-plane β depends only on the radial coordinate r. We construct the full eigenstate solution Ψ with energy ϵ as (5.27), (5.29), and (5.33),
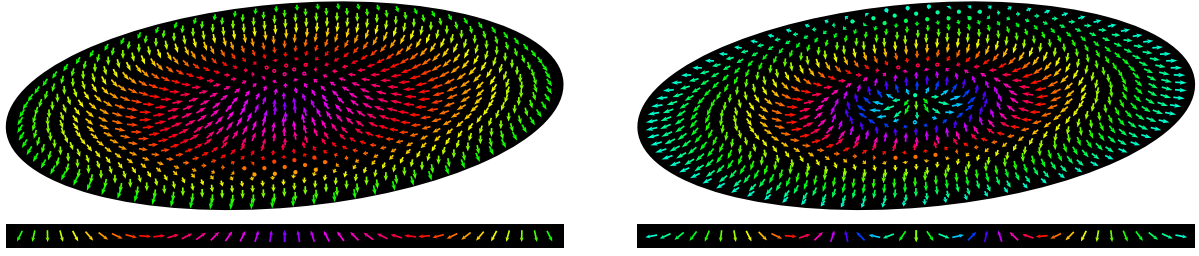
Figure 5.3: Spin textures in cylindrical quantum dots with $L = 100$ Å and $R = 275$ Å. Left and right panels show results for the lowest and the second lowest states with $|j_z| = 1/2$, respectively. The arrows and colors indicate the spin orientation as a function of the position in the xy-plane. Below the disks, the same data are shown for a linear cut through the center of the sample

depending on the value of ϵ, with the corresponding $K_a(\epsilon)$, and $K_b(\epsilon)$ obtained from a numerical solution of the quantization conditions (5.28), (5.30), or (5.34).

In Fig. 5.3, we present two examples of spin textures in cylindrical quantum dots of length $L = 100$ Å and radius $R = 275$ Å, in the presence of the full linear and the cubic SOC terms with the coupling strengths α_r and γ_r predicted in Ref. [57]. The left panel shows the dependence of the spin orientation on the position in the xy-plane for the lowest energy states that have $|j_z| = 1/2$. This spin texture corresponds to the ground state of the dot, shown in Fig. 5.2 by the two lowest levels depicted in black. The right panels show the spin texture for the next higher levels that are characterized by $|j_z| = 1/2$, corresponding to the second pair of levels (black lines starting at $|l_z| = 1$ in Fig. 5.2).

We next examine the effective g-factor of the dot.

5.4.3 Effective g-factor in quantum dots

From the experimental point of view, the effective g-factor is an accessible quantity, and it is thus a widely studied property. The measurements reported in Ref. [48] are an example. In that reference, the effective g-factor has been observed to depend on the dot size with absolute values that are reduced as compared to the bulk effective g-factor
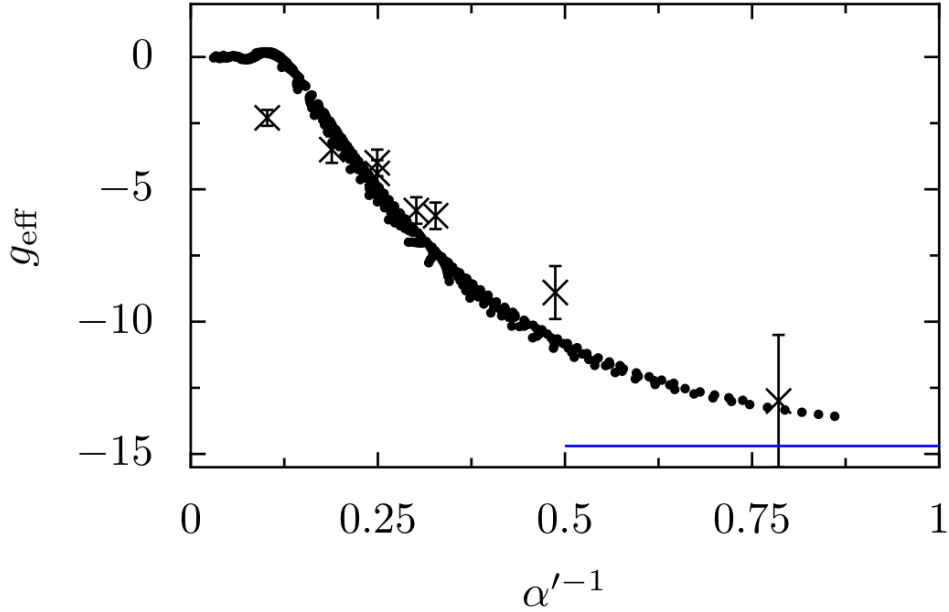
Figure 5.4: The calculated effective g-factors (full black circles) for cylindrical quantum
dots of different length L and radius R, plotted versus $1/\alpha'$ defined in (5.19),
with the SOC parameters from Ref. [57]. The data points are for dots with
radii R from 150 Å to 500 Å, and lengths values L in the range between 50 Å
and 200 Å. The crosses represent experimental data from Ref. [48], obtained
with a magnetic field perpendicular to the symmetry axis of the quantum
dot. The blue horizontal line indicates the bulk effective value $g^* \approx -14.7$.

$g^* \approx -14.7$ (value from Ref. [110]). Experimentally the effective g-factor is extracted
from the linear term of the magnetic-field induced energy splitting

$$\Delta E = |g_{\text{eff}} \mu_B B| \tag{5.37}$$

of two states that are characterized by the same $|j_z|$ and degenerate in the absence of a
magnetic field. According to this definition, each quantum-dot state has its own effective
g-factor, and we will focus on the effective g-factor of the ground state which is often the
most relevant. To calculate the effective g-factor we can use different approaches. The
most direct way is to set the magnetic field strength to a small finite value, $B = 0.1\,\text{T}$,
and to calculate the difference between the two lowest dot energies, using the procedure

of Sec. 5.4.1. To avoid the finite value of the magnetic field, we express the effective g-factor as

$$g_{\text{eff}} = \frac{1}{\mu_B} \frac{\partial \Delta E}{\partial B} = g^* \frac{\partial \epsilon}{\partial h} \tag{5.38}$$

in terms of the sensitivity $\partial \epsilon / \partial h$ of the quantized dot energy levels with respect to the magnetic field, at $h = 0$.

To determine this derivative, we proceed as in the case of Rashba SOC treated in Ref. [107], and derive the quantization condition, (5.28) for negative in-plane energy $\varepsilon < 0$, and (5.30) for positive $\varepsilon > 0$. The resulting expression for the effective g-factor is

$$g_{\text{eff}} = -g^* \frac{\text{sgn}(\varepsilon)u(K_{\text{a}}) + u(K_{\text{b}})}{u(K_{\text{a}})u(K_{\text{b}})} \tag{5.39}$$

$$\frac{J_m(K_{\text{a}})J_{m+1}(K_{\text{b}})}{\zeta(K_{\text{a}}, K_{\text{b}}) \left[2K_{\text{a}} + \text{sgn}(\varepsilon)u'(K_{\text{a}})\right]^{-1} + \text{sgn}(\varepsilon)\zeta(K_{\text{b}}, K_{\text{a}}) \left[2K_{\text{b}} - u'(K_{\text{b}})\right]^{-1}}$$

where we have defined the functions

$$\zeta(K_{\text{a}}, K_{\text{b}}) = J_m(K_{\text{b}})J'_{m+1}(K_{\text{a}}) + \text{sgn}(\varepsilon)J'_m(K_{\text{a}})J_{m+1}(K_{\text{b}}) \tag{5.40}$$

and $u(K) = \alpha'K - \gamma'K^3$. We denote by $J'_m(K)$ and $u'(K)$ the derivatives of the functions J_m and u with respect to K.

The expression of eq. (5.39) is a generalization of the result of Ref. [107], and reduces to the result given in eq. (13) of that publication in the case of vanishing cubic-in-k SOC ($\gamma = 0$). In order to compute the effective g-factor using the analytic expression (5.39), we first determine the eigenenergies and the corresponding pair of wave-vectors K_{a} and K_{b} by solving numerically the quantization condition of eqs. (5.28) and (5.30) at $h = 0$, and then evaluate (5.39) using the obtained values.

In Fig. 5.4 we present our results for different dot dimensions with length ranging from $50\,\text{Å}$ to $200\,\text{Å}$ and radii from $150\,\text{Å}$ to $500\,\text{Å}$. We have checked that a direct numerical evaluation of the level splitting from numerically calculated energies at small values of magnetic field B yields consistent results.

In the figure, the numerical data for g_{eff} (black dots) is plotted as a function of the inverse effective dimensionless linear in-plane spin-orbit coupling α'^{-1} (see eq. (5.19)). The data corresponding to different dot sizes approximately collapses on a single curve. While a plot as a function of α' shows the same data collapse, the presentation of Fig. 5.4 allows for greater clarity in the comparison with experiment. Such a single-parameter scaling shows that the dependence of the ground state effective g-factor g_{eff} on L and R is, at least within the range of explored sizes, to a good approximation given by a function of α'. Thus, the main mechanism giving rise to a size-dependence of the effective ground-state g-factor is the L-dependent renormalization of the effective linear coupling strength α' by the cubic SOC γ, and its scaling with R.

For a fixed value of L, the renormalized linear-in-k coupling strength α' is proportional to $1/u_{\text{E}}R$. Since $u_{\text{E}} \propto R^{-2}$, we have $\alpha' \propto R$ such that the effective linear coupling decreases with decreasing R. It can be seen in Fig. 5.4 that the value of g_{eff} increases (in absolute value) towards the bulk effective g-factor g^* (blue line) as R and thus the effective coupling α' decreases. An increase in R leads to a larger α', and according to Fig. 5.2, the Zeeman splitting of the levels decreases as the SOC increases. The consequence is that $|g_{\text{eff}}|$ diminishes. Conversely, for a given radius R, the increase in L leads to a decrease of the effective linear-in-k coupling α', with the result of an approach of g_{eff} to g^*.

The effective cubic-in-k coupling $\gamma' \propto 1/u_{\text{E}}R^3 \propto 1/R$ increases when R decreases, and a competition between α' and γ' can be expected. However, the spectrum of the lowest energies is related to small values of K and mainly dominated by the linear SOC (see Fig. 5.1), at least for the not too small values of R that we consider. The scaling of the results with α' leads to the conclusion that the main effect of the cubic Dresselhaus coupling γ is the renormalization of the effective linear-in-k coupling, and that the impact of the effective cubic-in-k coupling strength γ' seems to be of minor importance. However, the above arguments are relevant for the case under study of not too small R and low-energy dot states. More important effects of the cubic-in-k coupling γ' can be expected for the g-factor of excited states and in dots with very small R.

Similarly to the results presented in Ref. [110], where a zincblende Hamiltonian with adjustable parameters such as the energy band gap magnitude was used, we find negative values for the ground state g-factor of the dot. However, in our case small positive values do occur for short pillbox-shaped dots. In general, and similarly to the theoretical results for Rashba SOC [107] as well as the experimental values of Ref. [48] (crosses in Fig. 5.4), our effective g-factors are of reduced absolute value as compared to the bulk effective g-factor g^*. While the qualitative behavior and size-dependence of our results are clearly consistent with the data of Ref. [48], a direct quantitative comparison cannot be made since in the experiment the magnetic field direction is not aligned with the symmetry axis of the dots. Also, while the effective g-factor has been measured for very different values of L, only a small range of radii has been covered in Ref. [48].

The last topic we analyze in the following section is the spin-relaxation rate due to acoustic phonons.

5.4.4 Phonon-induced spin-relaxation rate

The spin lifetime may be limited by interactions with acoustic phonons. Therefore, we study here spin-relaxation rate due to phonon scattering between a final eigenstate $|f\rangle$ and an initial state $|i\rangle$ is given by Fermi's Golden Rule

$$\Gamma_{i \to f} = \frac{2\pi}{\hbar} \sum_{\mathbf{Q},\lambda} |\langle f|U_\lambda(\mathbf{Q})|i\rangle|^2 n(Q)\delta(\Delta E - \hbar\omega_\lambda) \tag{5.41}$$

where $\mathbf{Q}$ is the phonon momentum; the label $\lambda = l, t$ refers to the longitudinal and the transverse modes, respectively; $n(Q)$ is the Bose-Einstein phonon distribution with energy $\hbar\omega_\lambda = \hbar c_\lambda Q$, where c_λ is the sound velocity of the corresponding mode; $\Delta E = E_f - E_i$ is the energy difference between the two electronic states and determines, owing to the δ-function, the energy of the phonons involved in the relaxation process. The potential $U_\lambda(\mathbf{Q})$ comprises both the deformation and the piezoelectric phonon potentials [111–113] that in our case involves the wurtzite structure. For the longitudinal mode, we have

$$U_l(\mathbf{Q}) = [\,\Xi_l(\mathbf{Q}) + i\Delta_l(\mathbf{Q})\,]\,e^{i\mathbf{Q}\cdot\mathbf{r}} \tag{5.42}$$

with $\Xi_l(\mathbf{Q})$ being the deformation potential given by

$$\Xi_l(\mathbf{Q}) = \Xi_0 A_l \sqrt{Q} \tag{5.43}$$

where Ξ_0 is a bulk-phonon constant. The quantity $A_l = \frac{1}{\sqrt{V}}\sqrt{\frac{\hbar}{2\vartheta c_l}}$ contains the mass density ϑ and the sample volume V. It must be noted the deformation has an identical form as the zincblende case. The term $\Delta_l(\mathbf{Q})$ accounts for the piezoelectric contribution and upon introducing spherical coordinates (Q, θ_p, φ_p) for the phonon momentum, it reads

$$\Delta_l(\mathbf{Q}) \;=\; A_l \, \frac{1}{Q^{1/2}} \Delta_0 \cos(\theta_p) \left(h_{33} - \sin^2 \theta_p \, h_x\right) \tag{5.44}$$

where $h_x = h_{33} - 2h_{15} - h_{31}$. In general, h_{ij} are bulk phonon constants and $\Delta_0 = 4\pi e/\kappa$; where κ is the dielectric constant and e the electronic charge. We emphasize that θ_p is the angle between $\mathbf{Q}$ and the z-axis (defined as the c-axis of the wurtzite structure).

The transverse mode is given by

$$U_t(\mathbf{Q}) = \Delta_t(\mathbf{Q})e^{i\mathbf{Q}\cdot\mathbf{r}} \tag{5.45}$$

with

$$\Delta_t(\mathbf{Q}) = A_t \frac{1}{Q^{1/2}} \Delta_0 \sin(\theta_p) \left(h_{15} + \cos^2(\theta_p)h_x\right) \tag{5.46}$$

The parameter A_t is obtained by substituting c_l by c_t in the expression for A_l. We emphasize that in wurtzite, the transverse piezoelectric potential yields only one term, unlike the GaAs case which presents two contributions.

The calculation of the relaxation rate involves the integral over the phonon and the electron degrees of freedom in such a way that eq. (5.41) can be written as

$$\Gamma_{i\to f} = \frac{2\pi}{\hbar} \sum_{\mathbf{Q},\lambda} |M_\lambda(\mathbf{Q})|^2 |\langle f|e^{i\mathbf{Q}\cdot\mathbf{r}}|i\rangle|^2 n(Q)\delta(\Delta E - \hbar\omega_\lambda) \tag{5.47}$$

where $M_l = \Xi_l(\mathbf{Q}) + i\Delta_l(\mathbf{Q})$ and $M_t = \Delta_t(\mathbf{Q})$. We first note that the modulus of the momentum $\mathbf{Q}$ is fixed by the δ-function. Concerning the integral over the electronic coordinates, we remark that both the initial and the final states denoted by

$\Phi_{nm}^{f(i)}(\rho, \phi, z) = \psi_{nm}^{f(i)}(\rho, \phi, z) \sin(n\pi z/L)$ have the same z-dependent function. Therefore, the integral can be further split into two parts by using cylindrical coordinates, leading to

$$|\langle f|e^{i\mathbf{Q}\cdot\mathbf{r}}|i\rangle|^2 = |Z(\theta_p)|^2|\Upsilon(\theta_p, \varphi_p)|^2 \tag{5.48}$$

The integral over z can be analytically done, yielding

$$|Z(\theta_p)|^2 = (L/2)^2 q_z^2 (1 - \cos(q_z)) \left[\frac{1}{(2\pi n)^2 - q_z^2} + \frac{1}{q_z^2}\right]^2 \tag{5.49}$$

where the definition $q_z = QL\cos(\theta_p)$ has been used. The other integral $\Upsilon(\theta_p, \varphi_p)$ reads

$$
\begin{aligned}
\Upsilon(\theta_p, \varphi_p) &= \int_0^1 d\rho\rho \left[\left(c_a^f J_{m_f}(K_a^f\rho) + c_b^f J_{m_f}(K_b^f\rho)\right)\left(c_a^i J_{m_i}(K_a^i\rho) + c_b^i J_{m_i}(K_b^i\rho)\right)\right. \tag{5.50}\\
&+ \left.\left(c_a^f d_a^f J_{m_f+1}(K_a^f\rho) + c_b^f d_b^f J_{m_f+1}(K_b^f\rho)\right)\left(c_a^i d_a^i J_{m_i+1}(K_a^i\rho) + c_b^i d_b^i J_{m_i+1}(K_b^i\rho)\right)\right]\\
&\int_0^{2\pi} d\varphi\, e^{-i(m_f-m_i)\varphi}\, e^{iQ\sin(\theta_p)\cos(\varphi_p-\varphi)\rho R}
\end{aligned}
$$

The integral over φ can be easily performed by applying the Jacobi-Anger relation:

$$e^{ix\cos(\varphi)} = \sum_{m=-\infty}^{\infty} i^m J_m(x) e^{im\varphi} \tag{5.51}$$

Upon replacing eq. (5.51) in eq. (5.50) and carrying out the integration over φ, all the m-th terms vanish except when $m = m_i - m_f$. The integral then results

$$\int_0^{2\pi} d\varphi\, e^{-i(m_f-m_i)\varphi} e^{iQ\sin(\theta_p)\cos(\varphi_p-\varphi)\rho R} = 2\pi e^{-i(m_i-m_f)(\varphi_p+\pi/2)} J_{m_i-m_f}(\rho RQ\sin\theta_p) \tag{5.52}$$

As it can be seen in eq. (5.52), the complex exponential becomes a common factor in eq. (5.50) and leads to $|\Upsilon(\theta_p, \varphi_p)|^2 = f(\theta_p)$, which is not surprising, since the cylindrical symmetry is not broken by the phonon potential.

The calculation of the spin-relaxation rate still involves an integral over ρ, and a subsequent integration over θ_p (since neither $|\Upsilon(\theta_p, \varphi_p)|^2$ nor $|M_\lambda(\mathbf{Q})|^2$ depend on φ_p, cf. eqs. (5.43), (5.44) and (5.46)) that have to be done numerically.

We present the results for the spin relaxation as a function of magnetic field in Fig. 5.5. The initial and final eigenstates are the two lowest energy states (i.e the first Zeeman sublevel). As the piezoelectric bulk constants for WZ InAs nanowires have not

been obtained so far from microscopic calculation, we follow the standard prescription [111, 112, 114, 115] of estimating them from the cubic structure by the use of the relations $h_{15} = h_{31} = (-1/\sqrt{3})h_{14}$, $h_{33} = (2/\sqrt{3})h_{14}$ with h_{14} being the ZB constant $(3.5 \cdot 10^8 V m^{-1}$ [111]). In Fig. 5.5, the family of black curves correspond to the case of zero temperature, each denoting the contribution from the different phonon potentials separately. The parameters we use are $\rho = 5900 kg/m^3$, $c_l = 4410 m/s$, $c_t = 2130 m/s$, and $\Xi_0 = 5.8 eV$, taken from Ref. [111]. Our results show that the transverse piezoelectric mode yields the leading relaxation rate for the magnetic field range below $1.25\,T$. We have checked that our results are not very sensitive to the precise value of h_{14}: increasing the latter by a factor of two results in an increase by a factor of 4 for the range of studied parameters.

As it can be noted in eq. (5.41), the temperature dependence enters through the Bose-Einstein distribution, and therefore, the change with temperature of the spin-relaxation rate can be easily obtained. The result for the dominating TA-piezo mechanism is shown as a grey curve in Fig. 5.5

We also observe that our results are within the same order of magnitude compared to those in Ref. [111], in which the singlet-triplet relaxation for an InAs nanowire-based quantum dot is calculated. Nevertheless, in that work, only the deformation coupling is taken into account. The same assumption was made in Ref. [112], where the electron spin relaxation in a similar quantum dot was calculated. In both references, the dominance of the deformation over the piezoelectric potential was justified on the fact that they considered small semiconductor nanostructures. As explained in Ref. [116], there is a competition between the two components that depends on the size of the nanostructure. For instance, the leading role of the piezoelectric coupling for weak magnetic fields has also been reported [117] for quasi-one-dimensional quantum dots in zincblende GaAs nanowires, for "cigar-like" quantum dots. Also by considering GaAs quantum dots, a crossing between the deformation and piezoelectric-induced rate curves as a function of the magnetic field was found in Ref. [118]. In our case this occurs as well, though for lower values than those in Ref. [118]. However, numerical calculations on InSb nanowires
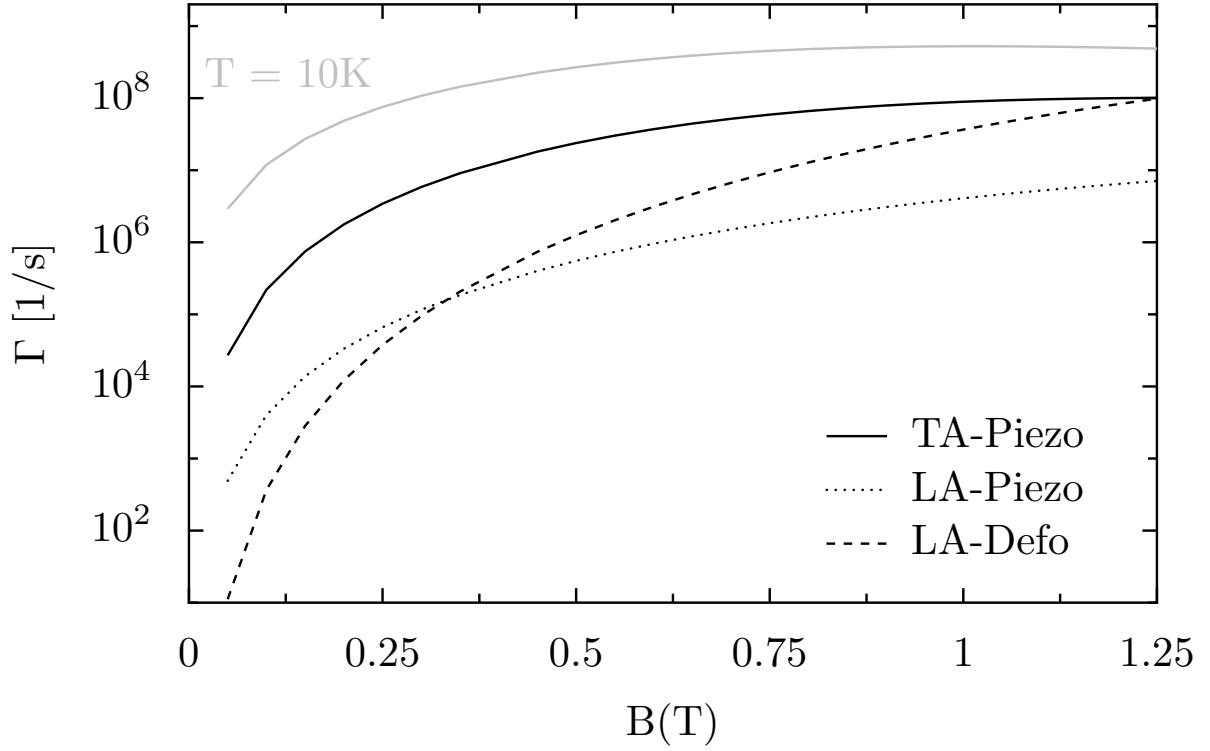
Figure 5.5: The spin-relaxation rate due to different acoustic-phonon potentials as a function of magnetic field, for InAs. The dark curves correspond to the relaxation rate at zero temperature yielded by the piezoelectric transverse (TA-Piezo), the piezoelectric longitudinal (LA-Piezo), and the deformation (LA-Defo) potentials. The grey line shows the spin-relaxation rate at $T = 10K$, only due to TA-Piezo.

show that the deformation potential dominates [117,118] for this material, and in general, this is believed to be the case for all narrow-gap semiconductors [119]. Yet this is in contrast with some recent results on an InAs nanowire quantum dot [115], where the piezoelectric coupling is crucial for the determination of the phonon spectrum.

Our result show that for InAs, which has a larger band gap than InSb, but smaller than GaAs, the spin relaxation rate is mainly driven by the (transverse) piezoelectric phonon potential for magnetic fields below 1.25 T. Beyond this value, the deformation seems to overcome the piezoelectric contribution, but our theory does not allow us to treat stronger magnetic fields.

5.5 Conclusion

We have presented an analytic solution to the problem of an electron in a quantum dot in the presence of Zeeman interaction and spin-orbit coupling. The effective Dresselhaus terms for this last interaction have been included taking into account the fact that we are dealing with a crystalline structure of wurtzite type. We have first considered the quasi-two-dimensional system, where two energy branches have been obtained. The effect of the linear and the cubic SOC terms have been separately examined.

The particular feature of two branches in the energy spectrum of the quasi-two-dimensional problem provides two degenerate solutions that can be combined in order to build a spinor that satisfies the boundary conditions imposed in the cylindrical quantum dot problem. We then come across an equation for the discretization of energies, which must be numerically addressed. By solving this root-finding problem, we obtain the allowed eigenenergies of the quantum dot. In order to examine and exhibit the contributions of the linear SOC term and the cubic SOC term, we calculate the energies as a function of the spin-orbit coupling strength. We find that the inclusion of the cubic term leads us to a range of coupling strength not explored before (cf. Ref. [107]), and allows us to conclude that the cubic term is of considerable relevance.

The calculation of the eigenstates also permits the study of the spin structure across

the dot. In particular, two spin textures of states with different energies -both of them with $|j_z = 1/2|$- are displayed.

We have also tackled the problem of the effective g-factor of the quantum dot. In agreement with the results of Ref. [110], we also observe negative values for the effective g-factor as a function of the dot size. Remarkably, we have found that our results scale very well with the inverse effective dimensionless linear in-plane spin-orbit coupling α'^{-1} defined in eq. (5.19))

We have also been able to calculate the spin-relaxation rate due to phonons. We then analyzed the phonon-induced rates as a function of magnetic field for the first Zeeman sublevel, by taking into account the electron-phonon potential for the wurtzite structure. The different rates arising from the longitudinal deformation, longitudinal piezoelectric, and transverse piezoelectric contribution have been studied by using Fermi's Golden Rule. We obtain a good agreement between our results for the spin-relaxation rate due to the deformation mechanism and the values shown in Ref. [111], where only the deformation potential is included. In the same Ref. [111], it is claimed that the deformation potential is the leading mechanism, under the assumption that they deal with small nanostructures. However, our result shows that the transverse piezoelectric phonon potential gives the largest rate.

Chapter 6

Concluding Remarks and outlook

The spin-orbit interaction resulting from the coupling between the motion of the electron and its spin, is the fundamental driving mechanism of many novel spintronic devices. The promising possibilities for technological applications are thus a strong motivation for exploring the various aspects of this interaction. Particularly important among them is the influence on the spin-relaxation time, that is the time during which the spin keeps its initial orientation. The subject of the first part of this thesis is the study of this important time for the case of bulk semiconductors. More precisely, we focus on n-doped semiconductors, GaAs doped with Silicon atoms representing a typical example. Although this specific material has been deeply studied over the last years, open questions have remained unsolved. This was firstly posed in 1998 by Kikkawa and Awschalom [25], who measured the spin-relaxation time in GaAs for several doping densities, employing a time-resolved Faraday rotation technique. They observed a non-monotonic behaviour of the spin-relaxation time as a function of the doping density and maximum values of the order of hundreds of nanoseconds. The confirmation was reported 4 year later, by Dzhioev and collaborators [26]. They found, using an optical orientation technique, two maximum values for the spin-relaxation time. While one of them is observed at a density of $3 \times 10^{15} cm^{-3}$ and yields a relaxation time of the order of 180 ns, the other one occurs at the critical density of the metal-insulator transition (MIT), which for GaAs is $2 \times 10^{16} cm^{-3}$. For this value, the relaxation time reaches

150 ns. At still higher doping levels, the spin-relaxation times decrease strongly with increasing doping.

Throughout the first part of this thesis, we consider the metallic side of this transition, i.e. we work with density values slightly larger then the critical one. For this range, we examine the effect of the spin-orbit coupling on the spin-relaxation time occurring in the impurity band. A zero-temperature formalism, properly justified, is put forth for donor electrons populating this band, without taking into account the electron-electron interaction. As it is explained in Chap. 2, we work within the Envelope-Function Approximation, and two different effective spin-orbit coupling terms have been included in our model.

On the one hand, the SOC associated to the *extrinsic* Coulomb potential of the disorder impurities is used in a preliminary study of the influence of the SOC on the impurity band (Chap. 3). We are interested in the characterization of the band, and in particular in the density of states (DOS) and the degree of spatial extension of the electronic levels. For the latter, we make use of the so-called Inverse Participation Ratio (IPR) parameter in order to estimate how localized a state is. Our theoretical approach to an electron in the impurity band is based on the Matsubara-Toyozawa (MT) Model, conceived for the study of electron conduction at zero temperature in the presence of randomly placed impurities. It consists of a tight-binding approximation built from the ground state of the doping centers. For shallow donors, the impurity states are described by an envelope function. The final MT Hamiltonian for the envelope function contains a kinetic energy term with an effective mass, plus a Coulomb-like potential, resulting from the sum of each Coulombic impurity center, in which the screening effect enters via a dielectric constant. While the MT states are eigenstates of the spin operator S_z, this is no longer the case once the SOC is included. In order to take into account the SOC, we rely on the Impurity Spin Admixture (ISA) theory proposed in Ref. [79], in which the SOC introduces a spin admixture in the original spherical-symmetric (s-like) MT impurity states. Our study then continues with the exact diagonalization of the MT Hamiltonian in the basis of ISA states. This Hamiltonian matrix now contains a new spin-flip

term connecting two different sites, brought about by the spin-independent Coulomb potential. As it turns out that two-center integrals -those in which the Coulombic center coincides with any of the two sites involved in the hopping element- give vanishing contributions, the spin-flip term is given by three-center integrals, which in this work are numerically performed, for no analytical expression is available. For the systems sizes we can treat numerically, the vanishing of the two-center integrals translates into a very weak SOC compared to the MT energy level spacing, and the spin-driven physics becomes masked. We are thus led to introduce an enhancement factor that multiplies the real SOC parameter, in order to increase at will the coupling strength. Considering only the MT model, we obtain localized states for the highest and lowest energy states, in agreement with the Anderson Model. However, we are not able to clearly identify well-defined mobility edges in the spectra, an observation already reported in Ref. [81]. We find that the DOS has a peak at zero energy (the isolated impurity level), and that it decreases towards the band extremes. Upon the inclusion of the SOC, we repeat this study by controlling its strength through the enhancement parameter. While the DOS is not apparently affected by the SOC, the IPR evidences some variations for certain energy regions. The effect of the SOC on the central part of the spectra, which contains the most extended states, is to reinforce the degree of delocalization. This effect gets more pronounced as the density is increased. On the other hand, the states with highest energy, with a strong localization feature, are scarcely modified due to the presence of SOC. This is not the case for the lower energy region. Here we note that the SOC also tends to delocalize states, even though its influence is diminished as we approach the band extreme. This permits us to claim that the SOC likely "pushes" the lower mobility edge to a lower energy value. The general behaviour we observe is the tendency to delocalize states caused by the SOC. We also focus our attention on the state at the Fermi level. Since the states in its vicinity undergo spin relaxation, the determination and characterization of it is of particular interest for our study about spin dynamics in the impurity band. The work and the original results that have just been discussed can be found in Ref. [21].

Still within a tight-binding approximation, we tackle the problem of electron spin relaxation for doping densities close to the metal-insulator transition. We incorporate in our description a SOC term associated to the bulk-inversion asymmetry (named BIA or Dresselhaus-like) of the zincblende structure we consider. We also keep the extrinsic term, but in this case we take an alternative path. Since the ISA formalism and an effective theory of spin-orbit interaction driven by the electrostatic potential of impurities are equivalent, we include here the extrinsic SOC term and work in the basis of hydrogenlike impurity states, that is to say, in the MT basis. The Hamiltonian operator describing an electron in the impurity band thus contains four terms altogether: the spin conserving part includes the ever present kinetic energy term plus the Coulomb potential of the impurities, while the terms leading to spin-flip scattering are the Dresselhaus interaction along with the extrinsic coupling. In order to study the spin dynamics, we develop a scheme of spin diffusion on the Bloch sphere. Two different time scales emerge thereof. One of them is related to the SOC, and consequently to the spin-relaxation time. The other time arises when the electron hop between two sites, no matter whether it entails a spin-flip or not, is considered. This diffusive process is therefore governed by the MT term, and its characteristic magnitude is much shorter than the spin decay time. We complement the analytical approach with a numerical estimation of the spin-relaxation time, which consists of tracking the spin evolution of an initial spin-polarized state under the influence of the full Hamiltonian. We then extract from its decay the spin-relaxation value. The size of the systems we are able to treat forces us, as before, to consider an enhancement parameter for the SOC. We next devise a double-step scaling procedure. We first calculate the spin-relaxation time (obtained as an average value over many disorder configurations) for a fixed enhancement factor and several system sizes, and extrapolate it to the infinite-size limit. Then, in a second extrapolation stage, the enhancement factor is varied approaching unity, aiming at the spin-relaxation time without enhancement.

We are able to confirm the result given in Ref. [79] concerning the too long spin-relaxation times yielded by the extrinsic SOC, justifying why we only keep the Dres-

selhaus term in the rest of our work. This last term involves two-center integrals, for which we are able to find a closed expression. We then carry on the analytical derivation and finally achieve a formula for the spin-relaxation time in terms of the doping density, the renormalized Bohr radius of the donor state, the MT energy scale, and the Dresselhaus coupling parameter. It is worth pointing out that our result is free of adjustable parameters. We find that the prediction it provides is in remarkably good agreement with the experimental values, and the density dependence approaches the experimental values. Nevertheless, the rather scattered experimental results do not allow us to reach a firm conclusion on this point. Not only have we got an accurate analytical result, but also the numerical procedure's results fit very well with the measured values of Ref. [26]. Also the behaviour of the extracted spin-relaxation times approach and follow the aforementioned analytical results. We can so identify the Dresselhaus SOC as the dominant interaction in the spin-relaxation problem in the impurity band. This original and relevant result has been published in Ref. [36]. We also claim that our theory is applicable to all zincblende semiconductors, except the very narrow-gap ones. This statement is supported by the observation that our theory yields for another recently studied material, CdTe, spin-relaxation times very close to the measured ones.

Nevertheless, more accurate experimental values would permit us to test the validity of our model, as well as the wide applicability we assign to it. In narrow-gap semiconductors, like InAs and InSb, the particularly large Bohr radii would lead to very long Dresselhaus relaxation times. In this cases, the competition between the extrinsic and the BIA terms brings up an interesting question.

Our description of the impurity band may be improved by considering the spatial overlap between the localized site states. This renders the original basis non-orthogonal, which would ultimately results in a time-independent Schrödinger equation in the form of a generalized eigenvalue problem. This issue has already been studied in Ref. [81]. According to it, to a first approximation the DOS with overlap are like mirror images of the densities obtained without overlap, the point of reflection being at $E = O$. In their study of the IPR, they do not observe any sensitive variation of the critical concentra-

tion due to overlap effects. We do not expect any modification in the IPR landscape including SOC, either, since its effect is of lower order than the MT-driven physics. In this sense, we do not believe the spin-relaxation values should change appreciably. A much harder task would be to include the electron-electron correlations. It is known that this interaction leads to a metal-insulator transition, known as the Mott-transition, in contrast to the disorder-driven Anderson transition, and occurs even in perfectly ordered systems. Nevertheless, it has been shown that the interaction effects are much more important on the insulating side of the transition than on the metallic side [120]. In Ref. [85] the metal-insulator transition is studied considering both the disorder (only off-diagonal) and the electron-electron interaction (in terms of a Hubbard U model with on-site repulsion). It is shown that the one-particle DOS in the impurity band is well defined and does not exhibit any gap on the metallic side of the transition, where the one-particle states at the Fermi energy are extended. They also claim that for uncompensated samples, as is the case of this thesis, the electron-electron interaction and disorder play an almost equally important role in the determination of the critical concentration, while for compensated semiconductors the disorder was the mechanism dominating the phenomenon of the MIT. However, by 1990, Mott concludes that the disorder is more important than the on-site Coulomb repulsion in the MIT even for uncompensated samples, in which only off-diagonal disorder is present [121, 122]. Therefore, the one-particle approach seems to be properly justified for the density range we consider in this thesis. Nevertheless, none of the works cited above treat the spin-orbit coupling in the impurity band description.

In our numerical study about spin-relaxation, we consider an enhancement factor η that allows us to make the SOC observable. This aspect of the calculation could be improved by increasing the size of the system (thereby making the MT level spacings smaller), and diminishing the value of η accordingly. Anyhow, we do not expect any considerable change in the extracted spin-relaxation times, as the values of the spin-relaxation times corresponding to smaller η's should fit the curve of the enhancement scaling.

The second part of this thesis deals with zero-dimensional systems. Here we consider a nanowire, within which the quantum dot is hosted. The nanowire material is InAs, that, similar to other materials, presents the wurtzite-type lattice structure when grown one dimensionally, whereas it is a zincblende material in its bulk phase. By taking this particular feature into account, we consider the corresponding effective spin-orbit coupling terms for the conduction band of a bulk wurtzite material. We then derive an analytical solution to the problem of a confined electron in a quantum dot in the presence of both Zeeman and spin-orbit interactions. The SOC that we consider is associated to the bulk inversion asymmetry of the crystal (Dresselhaus) and contains two different contributions for the three-dimensional system. On the one hand, a linear-in-k term, with the same mathematical form as the Rashba coupling. In addition to this, there is a cubic-in-k term, whose expression is different from the Dresselhaus SOC derived for zincblende materials. We first consider the quasi-two-dimensional system. Analogously to the Rashba problem, two energy branches are obtained. We examine the effect of the linear and the cubic SOC terms separately, and the existence of a crossing point in the energy spectrum due to the inclusion of the cubic term is shown.

A solution for the quantum dot can be built from these two branches in the following way. The two branches provide two independent degenerate solutions that can be combined in order to form a new spinor, which must satisfy the boundary conditions of the cylindrical quantum dot problem, with lateral hard-wall confinement. This last condition leads to an equation, whose solutions are the allowed discretized energies of the system. By solving this root-finding problem, which requires a numerical solution, we obtain the eigenenergies of the quantum dot. The results we present exhibit the effect of the linear and the cubic SOC term. By calculating the allowed energies as a function of the spin-orbit coupling strength, we find that the inclusion of the cubic term is of utmost importance and leads us to a range of coupling strength values that had not been reached in other works.

We next calculate the effective g-factor that is an accessible quantity from the experimental point of view. We obtain negative values for the g-factor in the range of dot

sizes and for the coupling parameters that we consider, in agreement with the results of Ref. [110]. Interestingly, we find that our results fit very well with the inverse effective dimensionless linear in-plane spin-orbit coupling α'^{-1} (see Eq. (5.19)), and which allows to establish a relation between the g-factor and the dot sizes. Unfortunately, we cannot directly compare our results for the g-factor with the experimental values reported in Ref. [48], since in the experiment the magnetic field is aligned perpendicularly to the wire.

The exact calculation of the eigenstates allows us to display the spin texture across the dot for two states with different energies. After that, we compute the spin-relaxation rate due to phonons. For this, we analyze the phonon-induced rates as a function of magnetic field for the lowest energy Zeeman sublevel. Consistently with our description of the system, we consider the acoustic electron-phonon potentials for the wurtzite structure, which present various terms, namely the longitudinal deformation, the longitudinal piezoelectric, and transverse piezoelectric terms. By using the Fermi's Golden Rule, we obtain a good agreement between our results for the spin-relaxation rate due to the deformation potential and the values reported in Ref. [111], where the singlet-triplet relaxation is studied, including only the deformation potential. The justification for this, given in the same Ref. [111], is that for small nanostructures, the deformation potential is the leading mechanism. The competition between the deformation and the piezoelectric mechanisms in relaxation rates is studied as a function of the radius of a semiconductor nanocrystal in Ref. [116]. According to their results, the deformation potential dominates for small sample sizes, while for the larger ones, the piezoelectric potential prevails. Our result indicates that the transverse piezoelectric phonon potential gives the largest spin-relaxation rate for the dot sizes that we consider, and within the range of magnetic field strength values that our theory allows us to study. A preprint of this work can be found in Ref. [58].

As we have pointed out, we have included in our model the effect of an external magnetic field only through the Zeeman interaction, and discarded the orbital effect of the magnetic field. In Ref. [107], where only the Rashba coupling is taken into

account, such a limitation is worked out by exchanging the Bessel functions by some other functions (confluent hypergeometric series), which renders the whole formulation more difficult in mathematical terms. However, since the analytical solution hinges upon the cylindrical symmetry of the dot, our problem including the cubic-in-k SOC term, which preserves this symmetry, would allow likewise an analytical solution if the full effect of magnetic field were treated. Nevertheless, we believe that our results should be useful in view of the rather weak magnetic fields considered in several related works (c.f. [17,123]).

For the coupling strength parameters, we have relied on the theoretical estimations performed in Ref. [57], where the parameters of the electronic band structure are predicted for many III-V semiconductors in the wurtzite phase. An experimental measurement of the parameters characterising the conduction band is desirable, since it would allow us to test our results. The spin-relaxation rate due to phonons also involves an approximation for the bulk phonon constants of a wurtzite material. We resort to a widely accepted relation in which the various phonon potential couplings are related to a single value corresponding to the bulk phonon constant h_{14} of a zincblende structure. A precise determination of the validity of this relation, or alternatively, the measurements of the WZ bulk phonon constants, would help us to clarify the dominance of the transverse piezoelectric mechanism over the other ones in the phonon-induced spin-relaxation problem.

Finally, we mention and emphasize that we study the relaxation due to bulk phonons. However, in small nanostructures, not only the electronic levels but also the vibrational modes become discrete due to the confinement. A multi-peak structure of the singlet-triplet relaxation rate as a function of magnetic field has been theoretically calculated in an InAs-based quantum dot (see Ref. [111]). The electron spin relaxation induced by confined phonons has already been studied in Ref. [112], but only for the deformation phonon potential and the Rashba spin-orbit coupling. Further research is thus needed in this sense.

We would like to cite the work in Ref. [17] as a strong motivation for continuing the study on InAs-based quantum dots. In that reference, a spin-orbit qubit in an InAs

semiconductor nanowire is implemented, and the so-called electric-dipole spin-resonance (EDSR) is invoked to account for the resonant transitions between spin-orbit states. It would thus be interesting to incorporate our study about spin-orbit coupling effects to the EDSR mechanism.

Chapter 7

Acknowledgements

Antes que nada, quisiera agradecer a mis directores de tesis, Rodolofo Jalabert y Pablo Tamborenea, por su continuo apoyo a lo largo de estos años. En el plano científico, trabajar con ambos ha sido más que enriquecedor y gratificante. Muchas gracias por la paciencia y por las respuestas a las preguntas (y por las preguntas a las respuestas). También quiero agradecer a ambos por haberme dado la posibilidad y el apoyo imprescindible para llevar a cabo una tesis entre dos universidades tan distantes. Quisiera agradecer y reconocer especialmente toda la ayuda brindada por Rodolfo para hacer posible mis estadías en Estrasburgo.

I am also utterly grateful to Dietmar Weinmann who has been to me like another thesis advisor. I've learnt a lot from him, too, by listening to his clear explanations and constructive feedback. I would like to acknowledge his invaluable contribution to this work. These last years have been very fruitful in terms of social life as well. I've met so many nice people, that I just feel lucky for this.

También agradecer a mi familia, y en particular a mis padres por su imponderable e incondicional apoyo, tantas veces necesario. Quiero darle las gracias a Lucía (nombre en clave " sonrisa asimétrica") por el sostén, las cenas y soportar algún que otro insomnio mío. Con ella, cada momento sólo ha sido mejor.

Quiero reconocer el papel de la universidad pública de Buenos Aires, que me ha formado desde el comienzo, y agradecer al CONICET por la ayuda financiera recibida.

Appendix A

Extrinsic spin-flip hopping matrix element

In this appendix we derive the spin-flip hopping element of the extrinsic SOC between two hydrogenic-like states, centered at different sites m and m'. We assume that the spin at site m is σ, while the spin at site m' is $-\sigma = \overline{\sigma}$. We start from eq. (4.9):

$$\langle m'\overline{\sigma}|H_{\text{ext}}|m\sigma\rangle = \lambda^* \left(\langle m'|\frac{\partial V}{\partial y}k_z - \frac{\partial V}{\partial z}k_y|m\rangle - i\sigma\langle m'|\frac{\partial V}{\partial x}k_z - \frac{\partial V}{\partial z}k_x|m\rangle \right). \quad (A.1)$$

Recalling that in the EFA formalism the wave vector $\vec{k}$ is an operator such that $k_i = -\frac{\partial}{\partial x_i}$, we proceed as follows

$$
\begin{aligned}
\langle m'\overline{\sigma}|H_{\text{ext}}|m\sigma\rangle &= \lambda^* \left[\int d\mathbf{r}\, \phi_{m'}^*(\mathbf{r}) \left(\frac{\partial V}{\partial y}k_z - \frac{\partial V}{\partial z}k_y \right) \phi_m(\mathbf{r}) \right. \\
&\quad \left. -i\sigma \int d\mathbf{r}\, \phi_{m'}^*(\mathbf{r}) \left(\frac{\partial V}{\partial x}k_z - \frac{\partial V}{\partial z}k_x \right) \phi_m(\mathbf{r}) \right] \\
&= \lambda^* \left[-i \int d\mathbf{r}\, \phi_{m'}^*(\mathbf{r}) \left(\frac{\partial V}{\partial y}\frac{\partial}{\partial z} - \frac{\partial V}{\partial z}\frac{\partial}{\partial y} \right) \phi_m(\mathbf{r}) \right. \\
&\quad \left. -\sigma \int d\mathbf{r}\, \phi_{m'}^*(\mathbf{r}) \left(\frac{\partial V}{\partial x}\frac{\partial}{\partial z} - \frac{\partial V}{\partial z}\frac{\partial}{\partial x} \right) \phi_m(\mathbf{r}) \right]. \quad (A.2)
\end{aligned}
$$

Integration by parts on the variable corresponding to the partial derivative of $V(\mathbf{r})$ yields

$$
\begin{aligned}
\langle m'\overline{\sigma}|H_{\text{ext}}|m\sigma\rangle = \lambda^* \left\{ -i \left[-\int d\mathbf{r}\, V(\mathbf{r})\frac{\partial}{\partial y}\left(\phi_{m'}^*\frac{\partial \phi_m}{\partial z} \right) + \int d\mathbf{r}\, V(\mathbf{r})\frac{\partial}{\partial z}\left(\phi_{m'}^*\frac{\partial \phi_m}{\partial y} \right) \right] \right. \\
\left. -\sigma \left[-\int d\mathbf{r}\, V(\mathbf{r})\frac{\partial}{\partial x}\left(\phi_{m'}^*\frac{\partial \phi_m}{\partial z} \right) + \int d\mathbf{r}\, V(\mathbf{r})\frac{\partial}{\partial z}\left(\phi_{m'}^*\frac{\partial \phi_m}{\partial x} \right) \right] \right\}. \quad (A.3)
\end{aligned}
$$

Appendix A Extrinsic spin-flip hopping matrix element

The terms with second order derivatives cancel out and the remaining terms read

$$
\begin{aligned}
\langle m'\overline{\sigma}|H_{\text{ext}}|m\sigma\rangle &= \lambda^* \left[i \int d\mathbf{r}\, V(\mathbf{r}) \left(\frac{\partial \phi_{m'}^*}{\partial y}\frac{\partial \phi_m}{\partial z} - \frac{\partial \phi_{m'}^*}{\partial z}\frac{\partial \phi_m}{\partial y} \right) \right. \\
&\quad + \left. \sigma \int d\mathbf{r}\, V(\mathbf{r}) \left(\frac{\partial \phi_{m'}^*}{\partial x}\frac{\partial \phi_m}{\partial z} - \frac{\partial \phi_{m'}^*}{\partial z}\frac{\partial \phi_m}{\partial x} \right) \right] \\
&= \lambda^* \int d\mathbf{r}\, V(\mathbf{r}) \left[\left(\sigma\frac{\partial \phi_{m'}^*}{\partial x} + i\frac{\partial \phi_{m'}^*}{\partial y} \right)\frac{\partial \phi_m}{\partial z} - \left(\sigma\frac{\partial \phi_m^*}{\partial x} + i\frac{\partial \phi_m^*}{\partial y} \right)\frac{\partial \phi_{m'}}{\partial z} \right] \\
&= \sigma\lambda^* \int d\mathbf{r}\, V(\mathbf{r}) \left[\frac{\partial \phi_m}{\partial z}\left(\frac{\partial}{\partial x} + i\sigma\frac{\partial}{\partial y} \right)\phi_{m'}^* - \frac{\partial \phi_{m'}}{\partial z}\left(\frac{\partial}{\partial x} + i\sigma\frac{\partial}{\partial y} \right)\phi_m^* \right].
\end{aligned}
\tag{A.4}
$$

The hydrogenic character of $\phi_m(\mathbf{r})$ leads to the following relation

$$
\frac{\partial \phi_m}{\partial x} = -\frac{\phi_m}{a}\frac{(x - X_m)}{|\mathbf{r} - \mathbf{R}_m|}
\tag{A.5}
$$

and analogously for the partial derivatives with respect to y and z. The letter a denotes the effective Bohr radius. The next step is to replace the equality in eq. (A.5) in order to obtain

$$
\begin{aligned}
\langle m'\overline{\sigma}|H_{\text{ext}}|m\sigma\rangle &= \frac{\sigma\lambda^*}{a^2} \int d\mathbf{r}\, V(\mathbf{r})\frac{\phi_{m'}(\mathbf{r})\phi_m(\mathbf{r})}{|\mathbf{r} - \mathbf{R}_{m'}||\mathbf{r} - \mathbf{R}_m|}\{(z - z_m)[(x - X_{m'}) + i\sigma(y - Y_{m'})] \\
&\quad -(z - z_{m'})[(x - X_m) + i\sigma(y - Y_m)]\} \\
&= \frac{\sigma\lambda^*}{a^2} \int d\mathbf{r}\, V(\mathbf{r})\frac{\phi_{m'}(\mathbf{r})\phi_m(\mathbf{r})}{|\mathbf{r} - \mathbf{R}_{m'}||\mathbf{r} - \mathbf{R}_m|} \\
&\quad [(z - z_m)(r_\sigma - R_{m'\sigma}) - (z - z_{m'})(r_\sigma - R_{m\sigma})],
\end{aligned}
\tag{A.6}
$$

The eq. (A.6) is exactly the expression of eq. (4.10), if the relations $r_\sigma = x + i\sigma y$ and $R_{m\sigma} = X_m + i\sigma Y_m$ are used.

Appendix B

The Impurity Spin Admixture wave function

In this appendix the derivation of the impurity spin admixture wave function is worked out. Owing to the SOC in the conduction band states (cbs), the spin polarized unperturbed function $\phi(\vec{r})[u_{\vec{k}=0,\sigma}](\vec{r})$ acquires a supplementary contribution that accounts for the spin mixing. Since the SOC modifies the cbs, we expect the impurity state of shallow donors, which are built out of cbs, to change accordingly. Starting from these modified cbs, we will now derive the impurity spin admixture wave function, firstly proposed in Ref. [79].

Using spinor language, a general impurity state located at the origin can be expressed as

$$
\begin{aligned}
[\Psi_\sigma](\vec{r}) &= \sum_{\vec{k}} \phi(\vec{k}) e^{i\vec{k}\cdot\vec{r}}[\mathbf{u}_{\vec{k}\sigma}](\vec{r}) \\
&= \frac{1}{N} \sum_{j,\vec{k}} \phi(\vec{R}_j) e^{-i\vec{k}\cdot\vec{R}_j} e^{i\vec{k}\cdot\vec{r}}[\mathbf{u}_{\vec{k}\sigma}](\vec{r})
\end{aligned} \tag{B.1}
$$

where the index j runs over all the units cells of the crystal, $\phi(\vec{r}) = (\frac{1}{\pi a^3})^{1/2} e^{-r/a}$, and $\vec{k}$ belongs to the first Brillouin zone. The SOC does not affect the envelope wave function considerably [79], and we assume that only the spinor $[\mathbf{u}_{\vec{k}\sigma}](\vec{r})$ is modified. It is thus no longer an eigenstate of S_z because the SOC leads to spin-mixed cbs at finite wave

vectors. Within the $k \cdot p$ approximation, the spinor $[\mathbf{u}_{\vec{k}\sigma}](\vec{r})$ can be written in bra-ket notation as [79, 91]

$$|\tilde{u}_{\mathbf{k}\sigma}\rangle = |u_{\vec{k}=0}^{\sigma}\rangle + \mathbf{k} \cdot |\mathbf{u}_{(1)}^{\sigma}\rangle \tag{B.2}$$

which in spite of not being an eigenstate of the spin, it can still be identified with a σ label if the spin mixing is weak. Whereas the state $|u_{\vec{k}=0}^{\sigma}\rangle$ is s-like since it represents the periodic wave function at the Γ point, the expression for $|\mathbf{u}_{(1)}^{\sigma}\rangle$ is

$$|\mathbf{u}_{(1)}^{\sigma}\rangle = \alpha_1 \left(|\mathbf{R}\sigma\rangle + \alpha_2 \mathbf{S} \times |\mathbf{R}\sigma\rangle \right) \tag{B.3}$$

and involves the p-like valence-band states $\mathbf{R} = (X, Y, Z)$. The angular momentum operator is denoted by $\mathbf{S}$. The constants $\alpha_1 = i\hbar \left[(3E_g + 2\Delta)/6m^* E_g (E_g + \Delta) \right]^1 /2$ and $\alpha_2 = 2\Delta/i\hbar(2\Delta + E_g)$ determine the degree of spin mixing. The energy E_g is the band gap, Δ is the spin-orbit splitting of the valence band, and m^* is the conduction-band effective mass. By replacing (B.3) in (B.1), we obtain

$$[\Psi_\sigma](\vec{r}) = \frac{1}{N} \sum_{j,\vec{k}} \phi(\vec{R}_j) e^{-i(\vec{R}_j - \vec{r}) \cdot \vec{k}} \left(|u_{\vec{k}=0}^{\sigma}\rangle + \mathbf{k} \cdot |\mathbf{u}_{(1)}^{\sigma}\rangle \right) \tag{B.4}$$

We see that while the first term gives $\phi(\vec{r})[u_{\vec{k}=0,\sigma}](\vec{r})$, the second term needs to be treated in more detail. The calculation follows as

$$\sum_j \frac{1}{N} \phi(\vec{R}_j) \mathbf{k} \cdot |\mathbf{u}_{\sigma(1)}\rangle(\vec{r}) \, e^{-i(\vec{R}_j - \vec{r}) \cdot \vec{k}} = \frac{1}{N} |\mathbf{u}_{(1)}^{\sigma}\rangle(\vec{r}) \sum_j \phi(\vec{R}_j)(-\frac{1}{i}) \nabla_{\vec{R}_j} \sum_{\vec{k}} e^{-i\vec{k} \cdot (\vec{R}_j - \vec{r})} \tag{B.5}$$

We next convert the sum into an integral over the different site positions, and use the fact that $\sum_{\vec{k}} e^{-i\vec{k} \cdot (\vec{R}_j - \vec{r})} = \delta(\vec{R}_j - \vec{r})$

$$\sum_j \frac{1}{N} \phi(\vec{R}_j) \mathbf{k} \cdot |\mathbf{u}_{\sigma(1)}\rangle(\vec{r}) \, e^{-i(\vec{R}_j - \vec{r}) \cdot \vec{k}} \cong |\mathbf{u}_{(1)}^{\sigma}\rangle(\vec{r})(-\frac{1}{i}) \int d\vec{R} \, \phi(\vec{R}) \, \nabla_{\vec{R}} \, \delta(\vec{R} - \vec{r})$$

(B.6)

Integration by parts yields

$$\sum_j \frac{1}{N} \phi(\vec{R}_j) \mathbf{k} \cdot |\mathbf{u}_{\sigma(1)}\rangle(\vec{r}) \, e^{-i(\vec{R}_j - \vec{r}) \cdot \vec{k}} \cong |\mathbf{u}_{(1)}^{\sigma}\rangle(\vec{r}) \left(\frac{1}{i} \right) \int d\vec{R} \, \delta(\vec{R} - \vec{r}) \, \nabla_{\vec{R}} \phi(\vec{R})$$

$$\cong \frac{1}{i} |\mathbf{u}_{(1)}^{\sigma}\rangle(\vec{r}) \nabla_{\vec{R}} \phi(\vec{R})\big|_{R=\vec{r}}$$

$$\cong \frac{1}{ia} |\mathbf{u}_{(1)}^{\sigma}\rangle(\vec{r}) \cdot \left(-\frac{\mathbf{r}}{|\mathbf{r}|} \right) \phi(\vec{r})$$

(B.7)

where in the last step the hydrogenic character of the wave function $\phi(\vec{r})$ has been used. The full expression for the impurity state located at the origin is

$$|\Psi_\sigma\rangle(\vec{r}) = \phi(\vec{r}) \left(|u_{\vec{k}=0}^{\sigma}\rangle(\vec{r}) + \frac{i}{a} \frac{\mathbf{r}}{|\mathbf{r}|} \cdot |\mathbf{u}_{(1)}^{\sigma}\rangle(\vec{r}) \right)$$

(B.8)

can be generalized for an impurity placed at position $\vec{r}_m$ to

$$|\Psi_\sigma\rangle(\vec{r} - \vec{r}_m) = \phi(\vec{r} - \vec{r}_m) \left(|u_{\vec{k}=0}^{\sigma}\rangle(\vec{r}) + \frac{i}{a} \frac{\mathbf{r} - \mathbf{r}_m}{|\mathbf{r} - \mathbf{r}_m|} \cdot |\mathbf{u}_{(1)}^{\sigma}\rangle(\vec{r}) \right)$$

(B.9)

which is the expression for the impurity spin admixture state presented in eq. (8) of Ref. [79]. We recall that the spin mixing enters through $|\mathbf{u}_{(1)}^{\sigma}\rangle(\vec{r})$. Since this is a linear combination of spin up and spin down states, it is not an eigenstate of S_z.

Appendix C

Impurity Spin admixture matrix element

We derive here the matrix elements between two ISA states, which have been obtained in the previous appendix.

The full Hamiltonian contains the kinetic energy and the sum of the (screened) Coulomb potential of the impurities. It reads

$$H = \frac{\vec{p}^2}{2m} + \sum_p V_p \tag{C.1}$$

where the electrostatic energy is given by

$$V_p = -\frac{e^2}{\epsilon |\vec{r} - \vec{r}_p|} \tag{C.2}$$

with $\vec{r}_p$ the position of a the impurity p that gives rise to the electrostatic field; ϵ is the dielectric constant, and e the electron charge.

The matrix elements $\langle n|H|m \rangle$ can be split into

$$\langle n|H|m \rangle = \langle n| \frac{\vec{p}^2}{2m} + V_m + \sum_{p \neq m} V_p |m \rangle = \epsilon_m \langle n|m \rangle + \sum_{p \neq m} \langle n|V_p|m \rangle \tag{C.3}$$

where we have assumed that $(\frac{\vec{p}^2}{2m} + V_m)|m \rangle = \epsilon_m |m \rangle$.

Appendix C Impurity Spin admixture matrix element

In the Matsubara-Toyozawa (MT) model the first term in eq. (C.3) is ignored by taking the ground state of an isolated impurity as the zero of energy. On the other hand, in the sum in eq. (C.3), only the integrals involving two centers are kept. This means that $\sum_{p \neq m} \langle n|V_p|m \rangle \cong \langle n|V_n|m \rangle$. In the MT model, the impurity sites are pure hydrogenic-like wave function centered at the impurity. If we take the impurity n to be at the origin, its wave function reads $\phi(\vec{r}) = (\frac{1}{\pi a^3})^{1/2} e^{-r/a}$, leading to

$$\langle n|V_n|m \rangle = -\frac{e^2}{\epsilon a}\left(1 + \frac{R_{nm}}{a}\right) e^{-R_{nm}/a} \tag{C.4}$$

where R_{mn} is the distance between the impurity n and m.

Nevertheless, the Impurity Spin Admixture theory goes beyond the MT model and the impurity states are modified according to

$$\phi(\vec{r} - \vec{r}_m)|u^\sigma_{\vec{k}=0}\rangle(\vec{r}) \rightarrow \phi(\vec{r} - \vec{r}_m)\left(|u^\sigma_{\vec{k}=0}\rangle(\vec{r}) + \frac{i}{a}\frac{\mathbf{r} - \mathbf{r}_m}{|\mathbf{r} - \mathbf{r}_m|}\cdot|\mathbf{u}^\sigma_{(1)}\rangle(\vec{r})\right) \tag{C.5}$$

where the perdiodic contribution of the Bloch functions of the conduction-band states at $\vec{k} = 0$ on the left side has been included. The previous result of eq. (C.4) for the matrix element within the MT model is recovered by separating the integral between an integral over the unit cell where the integration of the rapidly oscillating wave function $|u^\sigma_{\vec{k}=0}\rangle(\vec{r})$ is performed, and then an integral over the smooth varying functions $\phi(\vec{r})$.

We now consider the matrix elements between the ISA states (eq. (C.5)) and perform the integrals in two steps as before.

The terms involving the periodic wave function $|u^\sigma_{\vec{k}=0}\rangle(\vec{r})$ at $\vec{k} = 0$ yield the Matsubara-Toyozawa term:

$$-\frac{e^2}{\epsilon a}\left(1 + \frac{R_{nm}}{a}\right) e^{-R_{nm}/a}\delta_{\sigma\sigma'} \tag{C.6}$$

The $\delta_{\sigma\sigma'}$ accounts for the fact that no spin-flip occurs.

The **crossed term** involving the product $\langle u^\sigma_{\vec{k}=0}|\frac{\mathbf{r}-\mathbf{r}_m}{|\mathbf{r}-\mathbf{r}_m|}\cdot|\mathbf{u}^\sigma_{(1)}\rangle$ can be safely discarded if one invokes the orthogonality of $|S\rangle$ with $|X\rangle, |Y\rangle$, and $|Z\rangle$, and under the assumption that $\frac{\vec{r}}{|\vec{r}|}$ can be taken constant when integrating over the unit cell.

186

We thus concentrate in the **spin-flip** matrix elements due to the electrostatic potential at site

$$V_{nm}^{\sigma\sigma'} = -\frac{e^2}{\epsilon a^2} \int d^3r \frac{1}{|\vec{r} - \vec{R}_p|} \phi(\vec{r}) \frac{\vec{r}}{|\vec{r}|} \cdot [\mathbf{u}_{(1)}^{\sigma}]^{\dagger}(\vec{r}) \phi(\vec{r} - \vec{R}_m) \frac{\vec{r} - \vec{R}_m}{|\vec{r} - \vec{R}_m|} \cdot [\mathbf{u}_{(1)}^{\sigma}](\vec{r}) \quad \text{(C.7)}$$

We resort to our previous argument and consider that the functions ϕ, $\frac{1}{|\vec{r}-\vec{R}_p|}$, and $\frac{\vec{r}}{|\vec{r}|}$ do not change considerably throughout the unit cell. We also assume that the impurities are always at the same position in a unit cell. The integral is performed in two steps: we first integrate over the unit cell and then over the smooth varying functions across the crystal volume. The integral on the small scale with the origin of coordinates at position $\vec{R}_j$ reads

$$\int d^3r \frac{1}{|\vec{R}_j - \vec{R}_p|} \left(\frac{\vec{R}_j}{|\vec{R}_j|} \right) \cdot [\mathbf{u}_{(1)}^{\sigma}](\vec{r})^{\dagger} \left(\frac{\vec{R}_j - \vec{R}_m}{|\vec{R}_j - \vec{R}_m|} \right) \cdot [\mathbf{u}_{(1)}^{\sigma'}](\vec{r})$$

$$= \frac{1}{|\vec{R}_j - \vec{R}_p|} \sum_{\alpha,\beta=1}^{3} \left(\frac{\vec{R}_j}{|\vec{R}_j|} \right)_{\alpha} \left(\frac{\vec{R}_j - \vec{R}_m}{|\vec{R}_j - \vec{R}_m|} \right)_{\beta} \int d^3r [\mathbf{u}_{(1)}^{\sigma}]_{\alpha}(\vec{r})^{\dagger} [\mathbf{u}_{(1)}^{\sigma'}]_{\beta}(\vec{r}) \quad \text{(C.8)}$$

We need to examine the integral of the different components of the function $[\mathbf{u}_{(1)}^{\sigma'}]$. For this, we switch to bra-ket notation, so that the spin-mixing term $[\mathbf{u}_{(1)}^{\sigma}]_{\alpha}(\vec{r})$ is

$$
\begin{aligned}
|\mathbf{u}_{(1)}^{\sigma}\rangle = \ & \alpha_1 \widehat{x} \ \left[|X\sigma\rangle + \frac{\alpha_2 \hbar}{2} s(\sigma) \left(i|Z\overline{\sigma}\rangle - |Y\sigma\rangle \right) \right] + \\
& \alpha_1 \widehat{y} \ \left[|Y\sigma\rangle - \frac{\alpha_2 \hbar}{2} \left(|Z\overline{\sigma}\rangle - s(\sigma)|X\sigma\rangle \right) \right] + \\
& \alpha_1 \widehat{z} \ \left[|Z\sigma\rangle + \frac{\alpha_2 \hbar}{2} \left(|Y\overline{\sigma}\rangle - is(\sigma)|X\overline{\sigma}\rangle \right) \right] \quad \text{(C.9)}
\end{aligned}
$$

where α_1 and α_2 have been introduced in the previous appendix. The function $s(\sigma)$ indicates the eigenvalue of the spin operator

$$s(\sigma) = \sigma|\sigma\rangle$$

Appendix C Impurity Spin admixture matrix element

such that

$$s(\uparrow) = 1 \text{ and } s(\downarrow) = -1$$

We do not carry out the detailed calculation of the integrals here. The result for them can be summarized as

$$
\begin{aligned}
\langle \mathbf{u}^{(x)}_{\sigma(1)} | \mathbf{u}^{(x)}_{\sigma'(1)} \rangle &= \langle \mathbf{u}^{(y)}_{\sigma(1)} | \mathbf{u}^{(y)}_{\sigma'(1)} \rangle = \langle \mathbf{u}^{(z)}_{\sigma(1)} | \mathbf{u}^{(z)}_{\sigma'(1)} \rangle = |\alpha_1|^2 \left[1 + \frac{|\alpha_2|^2 \hbar^2}{2} \right] \delta_{\sigma\sigma'} \\
\langle \mathbf{u}^{(x)}_{\sigma(1)} | \mathbf{u}^{(y)}_{\sigma'(1)} \rangle &= -\langle \mathbf{u}^{(y)}_{\sigma(1)} | \mathbf{u}^{(x)}_{\sigma'(1)} \rangle = -i|\alpha_1|^2 \alpha_3 s(\sigma) \delta_{\sigma\sigma'} \\
\langle \mathbf{u}^{(x)}_{\sigma(1)} | \mathbf{u}^{(z)}_{\sigma'(1)} \rangle &= -\langle \mathbf{u}^{(z)}_{\sigma(1)} | \mathbf{u}^{(x)}_{\sigma'(1)} \rangle = |\alpha_1|^2 \alpha_3 s(\sigma) \delta_{\sigma\bar{\sigma}'} \\
\langle \mathbf{u}^{(y)}_{\sigma(1)} | \mathbf{u}^{(z)}_{\sigma'(1)} \rangle &= -\langle \mathbf{u}^{(z)}_{\sigma(1)} | \mathbf{u}^{(y)}_{\sigma'(1)} \rangle = -i|\alpha_1|^2 \alpha_3 s(\sigma) \delta_{\sigma\bar{\sigma}'} \quad \text{(C.10)}
\end{aligned}
$$

After inserting these last expressions in eq. (C.8), we are left with the remaining part of the integral of eq. (C.7), i.e. over the smooth variables. This means that we have to do the integral over the sites R_j introduced in eq. (C.8). For the specific case of $\sigma = \uparrow$ and $\sigma' = \downarrow$, it finally reads

$$
\begin{aligned}
\langle n \uparrow | V_p | m \downarrow \rangle = \; &C \int d^3 r \frac{e^{-(|\vec{r} - \vec{R}_n| + |\vec{r} - \vec{R}_m|)/a}}{|\vec{r} - \vec{R}_n||\vec{r} - \vec{R}_m||\vec{r} - \vec{R}_p|} \\
&\left[(z - Z_n)(\vec{r} - \vec{R}_m)_- - (z - Z_m)(\vec{r} - \vec{R}_n)_- \right] \quad \text{(C.11)}
\end{aligned}
$$

where the subscript next to the brackets must be understood as $R_\pm = X \pm iY$ and $C = V_0 |\alpha_1|^2 \alpha_3 / \pi a^4$. The newly defined constant α_3 regroups the spin split-off energy and the band-gap:

$$\alpha_3 = \frac{3\Delta(\Delta + 2E_g)}{(2\Delta + 3E_g)^2}$$

By comparing the integrals in eq. (A.6) and eq. (C.11), we note the equivalence of both

calculations. As mentioned before (or in Ref. [79]), it can be shown that the integral in eq. (C.11) vanishes when the impurity $n = p$. The lowest contribution then involves three-center integrals which must be numerically evaluated as no analytical formula is available.

Bibliography

[1]   J. H. Davies, *The Physics of Low-Dimensional Semiconductors - An introduction* (Cambridge University Press, Cambridge, 1998), 1st ed.

[2]   M. N. Baibich, J. M. Broto, A. Fert, F. N. V. Dau, F. Petroff, P. Etienne, G. Creuzet, A. Friederich, and J. Chazelas, Phys. Rev. Lett. **61**, 2472 (1988).

[3]   G. Binasch, P. Grünberg, F. Saurenbach, and W. Zinn, Phys. Rev. B **39**, 4828 (1989).

[4]   C. Chappert, A. Fert, and F. N. V. Dau, Nature Materials **6**, 813 (2007).

[5]   E. Gerstner, Nature Physics **3**, 754 (2007).

[6]   J. DeBrosse, D. Gogl, A. Bette, H. Hoenigschmid, R. Robertazzi, C. Arndt, D. Braun, D. Casarotto, R. Havreluk, S. Lammers, et al., *A high-speed 128-kb mram core for future universal memory applications*, Solid-State Circuits, IEEE Journal of **39**, 678 (2004).

[7]   C. Gould, C. Rüster, T. Jungwirth, E. Girgis, G. M. Schott, R. Giraud, K. Brunner, G. Schmidt, and L. W. Molenkamp, Phys. Rev. Lett. **93**, 117203 (2004).

[8]   S. Datta and B. Das, Appl. Phys. Lett. **56**, 665 (1990).

[9]   I. Žutić, J. Fabian, and S. D. Sarma, *Spintronics: Fundamentals and applications*, Rev. Mod. Phys. **76**, 323 (2004).

[10]   J. Schliemann, J. C. Egues, and D. Loss, Phys. Rev. Lett. **90**, 146801 (2003).

Bibliography

[11] G. Feher and E. A. Gere, Phys. Rev. **114**, 1245 (1959).

[12] P. W. Anderson, Phys. Rev. **109**, 1492 (1958).

[13] P. W. Anderson, *50 Years of Anderson Localization* (World Scientific, Singapore, 2010), 1st ed.

[14] D. Loss and D. P. DiVicenzo, Phys. Rev. A **57**, 120 (1998).

[15] B. E. Kane, Nature **393**, 133 (1998).

[16] J. M. Elzerman, R. Hanson, L. H. W. van Beveren, B. Witkamp, L. M. K. Vandersypen, and L. P. Kouwenhoven, Nature **430**, 431 (2004).

[17] S. Nadj-Perge, S. M. Frolov, E. P. A. M. Bakkers, and L. P. Kouwenhoven, Nature **468**, 1084 (2010).

[18] F. Duan and J. Guojun, *Introduction to Condensed Matter Physics*, vol. 1 (World Scientific, Singapore, 2005), 1st ed.

[19] A. Rodriguez, L. J. Vasquez, and R. A. Römer, Phys. Rev. B **78**, 195107 (2008).

[20] S. V. Kravchenko and M. P. Sarachik, Rep. Prog. Phys. **67**, 1 (2004).

[21] G. A. Intronati, P. I. Tamborenea, D. Weinmann, and R. A. Jalabert, Physica B **407**, 3252 (2012).

[22] M. W. Wu, J. H. Jiang, and M. Q. Weng, Physics Reports **493**, 61 (2010).

[23] J. S. Colton, M. E. Heeb, P. Schroeder, A. Stokes, L. R. Wienkes, and A. S. Bracker, Phys. Rev. B **75**, 205201 (2007).

[24] J. Fabian, A. Matos-Abiague, C. Ertler, P. Stano, and I. Zutic, Acta Physica Slovaca **57**, 565 (2007).

[25] J. M. Kikkawa and D. D. Awschalom, Phys. Rev. Lett. **80**, 4313 (1998).

[26] R. I. Dzhioev, K. V. Kavokin, V. L. Korenev, M. V. Lazarev, B. Y. Meltser, M. N. Stepanova, B. P. Zakharchenya, D. Gammon, and D. S. Katzer, Phys. Rev. B **66**, 245204 (2002).

[27] D. D. Awschalom, Physica E **10**, 1 (2001).

[28] J. S. Colton, T. A. Kennedy, A. S. Bracker, and D. Gammon, Phys. Rev. B **69**, 121307 (2004).

[29] M. Oestreich, M. Römer, R. J. Haug, and D. Hägele, Phys. Rev. Lett. **95**, 216603 (2005).

[30] M. Römer, H. Bernien, G. Müller, D. Schuh, J. Hübner, and M. Oestreich, Phys. Rev. B **81**, 075216 (2010).

[31] A. W. Overhauser, *Paramagnetic relaxation in metals*, Phys. Rev. **89**, 689 (1953).

[32] M. I. Dyakonov, *Spin Physics in Semiconductors* (Springer, 2008), 1st ed.

[33] K. V. Kavokin, Phys. Rev. B **64**, 075305 (2001).

[34] K. V. Kavokin, Semicond. Sci. Technol. **23**, 114009 (2008).

[35] J. Fabian and S. D. Sarma, J. Vac. Sci. Technol. B **17**, 1708 (1999).

[36] G. A. Intronati, P. I. Tamborenea, D. Weinmann, and R. A. Jalabert, Phys. Rev. Lett. **108**, 016601 (2012).

[37] H. W. Jiang and E. Yablonovitch, Phys. Rev. B **64**, 041307 (2001).

[38] W. Jantsch, Z. Wilamowski, N. Sandersfeld, M. Mühlberger, and F. Schäffler, Physica E **13**, 504 (2002).

[39] Y. Kato, R. C. Myers, D. C. Driscoll, A. C. Gossard, J. Levy, and D. D. Awschalom, Science **299**, 1201 (2003).

[40] E. I. Rashba and A. L. Efros, Appl. Phys. Lett. **83**, 5295 (2003).

Bibliography

[41] E. I. Rashba and A. L. Efros, Phys. Rev. Lett. **91**, 126405 (2003).

[42] AIXTRON Ltd., *How **MOCVD** works.deposition technology for beginners* (2011), URL `http://www.aixtron.com/fileadmin/user_upload/Unternehmen/ Acrobat4_MOCVD-Brochuere_E_LoRes.pdf`.

[43] L. Samuelson, Materials Today **6**, 22 (2003).

[44] P. Streda and P. Seba, Phys. Rev. Lett. **90**, 256601 (2003).

[45] V. Mourik, K. Zuo, S. M. Frolov, S. R. Plissard, E. P. A. M. Bakkers, and L. P. Kouwenhoven, Science **336**, 1003 (2012).

[46] M. T. Björk, B. J. Ohlosson, T. Sass, A. I. Persson, C. Thelander, M. H. Magnusson, K. Deppert, L. R. Wallenberg, and L. Samuelson, Nano Lett. **2**, 87 (2002).

[47] M. T. Björk, A. Fuhrer, A. E. Hansen, M. W. Larsson, L. E. Fröberg, and L. Samuelson, Nano Letters **4**, 1621 (2004).

[48] M. T. Björk, A. Fuhrer, A. E. Hansen, M. W. Larsson, L. E. Fröberg, and L. Samuelson, Phys. Rev. B **72**, 201307(R) (2005).

[49] F. H. L. Koppens, C. Buizert, K. J. Tielrooij, I. T. Vink, K. C. Nowack, T. Meunier, L. P. Kouwenhoven, and L. M. K. Vandersypen, Nature **442**, 766 (2006).

[50] B. G. Levi, Physics Today **64**, 19 (2011).

[51] K. C. Nowack, F. H. L. Koppens, Y. V. Nazarov, and L. M. K. Vandersypen, Science **318**, 1430 (2007).

[52] V. N. Golovach, M. Borhani, and D. Loss, Phys. Rev. B **74**, 165319 (2006).

[53] M. Koguchi, H. Kakibayashi, M. Yazawa, K. Hiruma, and T. Katsuyama, Jpn. J. Appl. Phys. **31**, 2061 (1992).

[54] J. Johansson, K. A. Dick, P. Caroff, M. E. Messing, J. Bolinsson, K. Deppert, and L. Samuelson, The Journal of Physical Chemistry C **114**, 3837 (2010).

194

[55] L. C. L. Y. Voon, M. Willatzen, M. Cardona, and N. E. Christensen, Phys. Rev. B **53**, 10703 (1996).

[56] J. Y. Fu and M. W. Wu, J. Appl. Phys. **104**, 093712 (2008).

[57] A. De and C. E. Pryor, Phys. Rev. B **81**, 155210 (2010).

[58] G. A. Intronati, P. I. Tamborenea, D. Weinmann, and R. A. Jalabert, arXiv:1303.1363 (2013).

[59] W. Greiner, *Quantum Mechanics - An Introduction* (Springer, Berlin, 2001), 4th ed.

[60] D. Griffiths, *Introduction to Elementary Particles* (John Wiley Sons, New York, 1987), 1st ed.

[61] J. Ziman, *Elements of advanced quantum theory* (Cambridge University Press, London, 1969), 1st ed.

[62] J. J. Sakurai, *Modern Quantum Mechanics - Revised Edition* (Addison-Wesley Publishing company, 1994), rev. ed.

[63] M. Tinkham, *Group Theory and Quantum Mechanics* (McGraw-Hill Book Company, 1964), 1st ed.

[64] R. F. Pierret, *Advanced Semiconductor Fundamentals, Vol. VI* (Prentice-Hall, New Jersey, 2002), 2nd ed.

[65] N. W. Ashcroft and N. D. Mermin, *Solid State Physics* (Harcourt College, Orlando, 1976), 1st ed.

[66] R. J. Elliot, Phys. Rev. **96**, 266 (1954).

[67] G. Dresselhaus, Phys. Rev. **100**, 580 (1955).

[68] H.-A. Engel, E. I. Rashba, and B. I. Halperin, *Theory of spin hall effects in semiconductors*, arXiv **3**, 60330 (2008).

Bibliography

[69] R. Winkler, *Spin-orbit Coupling Effects in Two-Dimensional Electron and Hole Systems* (Springer, Heidelberg, 2003), 1st ed.

[70] P. Y. Yu and M. Cardona, *Fundamentals of Semiconductors* (Springer, Heidelberg, 2010), 4th ed.

[71] H. Haug and S. W. Koch, *Quantum Theory of the Optical and Electronic Properties of Semiconductors* (World Scientific, Frankfurt, 2003), 4th ed.

[72] C. L. Y. Voon and M. Willatzen, *The $k \cdot p$ Method* (Springer, Heidelberg, 2009), 1st ed.

[73] W. T. Wang, C. L. Wu, S. F. Tsay, M. H. Gau, I. Lo, H. F. Kao, D. J. Jang, J. C. Chiang, M. E. Lee, Y. C. Chang, et al., Appl. Phys. Lett. **91**, 082110 (2007).

[74] J. Nitta, T. Akazaki, H. Takayanagi, and T. Enoki, Phys. Rev. Lett. **78**, 1335 (1997).

[75] J. P. Lu, J. B. Yau, S. P. Shukla, M. Shayegan, L. Wissinger, U. Rössler, and R. Winkler, Phys. Rev. Lett. **81**, 1282 (1998).

[76] P. Nozières and C. Lewiner, J. Phys. (Paris) **34**, 901 (1973).

[77] H.-A. Engel, E. I. Rashba, and B. I. Halperin, *Handbook of Magnetism and Advanced Magnetic Materials*, vol. Vol. 5 (John Wiley & Sons Ltd, Chichester, 2007).

[78] E. I. Rashba, Sov. Phys. Solid State **2**, 1109 (1960).

[79] P. I. Tamborenea, D. Weinmann, and R. A. Jalabert, Phys. Rev. B **76**, 085209 (2007).

[80] T. Matsubara and Y. Toyozawa, Prog. Theoret. Phys. **26**, 739 (1961).

[81] W. Y. Ching and D. L. Huber, Phys. Rev. B **26**, 5596 (1982).

[82] A. Puri and T. Odagaki, Phys. Rev. B **29**, 1707 (1984).

[83] M. K. Gibbons, D. E. Logan, and P. A. Madden, Phys. Rev. B **38**, 7292 (1988).

[84] B. I. Shklovskii and A. L. Efros, *Electronic properties of doped semiconductors* (Springer Verlag, 1984).

[85] E. N. Economou and A. C. Fertis, *Localization and Metal-Insulator Transitions* (Plenum Press, 1985).

[86] B. Kramer and A. MacKinnon, Rep. Prog. Phys. **56**, 1469 (1993).

[87] B. Kramer, A. MacKinnon, T. Ohtsuki, and K. Slevin, Int. J. Mod. Phys. **24**, 1841 (2010).

[88] V. Zarifis and T. G. Castner, Phys. Rev. B **36**, 6198 (1987).

[89] T. Ando, Phys. Rev. B **40**, 5325 (1989).

[90] Y. Asada, K. Slevin, and T. Ohtsuki, Phys. Rev. Lett. **89**, 256601 (2002).

[91] J. N. Chazalviel, Phys. Rev. B **11**, 1555 (1975).

[92] J. C. Slater, *Quantum Theory of Molecules and Solids* (McGraw-Hill, 1963).

[93] J. P. Gaspard and F. Cyrot-Lackmann, J. Phys. C **6**, 5325 (1989).

[94] G. A. Thomas, M. Capizzi, F. DeRosa, R. N. Bhatt, and T. M. Rice, Phys. Rev. B **23**, 5472 (1981).

[95] N. Majlis and E. Anda, J. Phys. C: Solid State Phys. **11**, 1607 (1978).

[96] F. Klopp, Journal of Mathematical Physics **43**, 2948 (2002).

[97] B. I. Shklovskii, Phys. Rev. B **73**, 193201 (2006).

[98] W. O. Putikka and R. Joynt, Phys. Rev. B **70**, 113201 (2004).

[99] I. S. Lyubinskiy, A. P. Dmitriev, and V. Y. Kachorovskii, JETP Lett. **85**, 55 (2007).

Bibliography

[100] T. Moriya, Phys. Rev. **120**, 91 (1960).

[101] I. Dzyaloshinski, J. Phys. Chem. Solids **4**, 241 (1958).

[102] P. H. Roberts and H. D. Ursell, Phil. Trans. R. Soc. Lond. A **252**, 317 (1960).

[103] G. A. Thomas, M. Capizzi, F. DeRosa, R. N. Bhatt, and T. M. Rice, Phys. Phys. B **23**, 5472 (1981).

[104] D. Sprinzl, P. Horodyská, N. Tesařová, E. Rozkotová, E. Belas, R. Grill, P. Malý, and P. Němec, Phys. Phys. B **82**, 153201 (2010).

[105] B. Jusserand, D. Richards, G. Allan, C. Priester, and B. Etienne, Phys. Rev. B **51**, 4707 (1995).

[106] E. N. Bulgakov and A. F. Sadreev, JETP Lett. **73**, 505 (2001).

[107] E. Tsitsishvili, G. S. Lozano, and A. O. Gogolin, Phys. Rev. B **70**, 115316 (2004).

[108] N. J. Harmon, W. O. Putikka, and R. Joynt, Appl. Phys. Lett. **98**, 073108 (2011).

[109] W.-T. Wang, C. L. Wu, J. C. Chiang, I. Lo, H. F. Kao, Y. C. Hsu, W. Y. Pang, D. J. Jang, M.-E. Lee, Y.-C. Chang, et al., J. Appl. Phys. **108**, 083718 (2010).

[110] A. De and C. E. Pryor, Phys. Rev. B **76**, 155321 (2007).

[111] Y. Yin, Semicond. Sci. Technol. **25**, 125004 (2010).

[112] Y. Yin and M. W. Wu, Journal of Applied Physic **108**, 063711 (2010).

[113] J. D. Zook, Physics Today **136**, 869 (1964).

[114] A. Bykhovski, B. Gelmont, M. Shur, and A. Khan, Journal of Applied Physics **77**, 1616 (1995).

[115] C. Weber, A. Fuhrer, C. Fasth, G. Lindwall, L. Samuelson, and A. Wacker, Phys. Rev. B **104**, 036801 (2010).

[116] T. Takagahara, Phys. Rev. Lett. **71**, 3577 (1993).

[117] C. L. Romano, P. I. Tamborenea, and S. E. Ulloa, Phys. Rev. B **74**, 155433 (2006).

[118] C. F. Destefani and S. E. Ulloa, Phys. Rev. B **72**, 115326 (2005).

[119] C. L. Romano, G. E. Marques, L. Sanz, and A. M. Alcalde, Phys. Rev. B **77**, 033301 (2008).

[120] S. N. Mott, *Conduction in non-crystalline materials* (Oxford Science Publications, Clarendon Press, Oxford, 1987).

[121] N. F. Mott, *Metal-Insulator Transitions* (Taylor and Francis Ltd, Oxford, 1990), 2nd ed.

[122] M. H. Cohen, Physica B **296**, 7 (2001).

[123] C. E. Pryor and M. E. Flatté, Phys. Rev. Lett. **96**, 026804 (2006).